공학석사학위논문

CEA 데이터베이스를 활용한 평형 유동 CFD 코드 개발 및 SiC 코팅 노즐의 삭마량 예측

Development of Equilibrium Flow CFD Code Using CEA Database and Prediction on Ablation of SiC Coating Nozzle

2017년 8월

서울대학교 대학원

기계항공공학부

배 지 환

CEA 데이터베이스를 활용한 평형 유동 CFD 코드 개발 및 SiC 코팅 노즐의 삭마량 예측

Development of Equilibrium Flow CFD Code Using CEA Database and Prediction on Ablation of SiC Coating Nozzle

지도교수 김 규 홍

이 논문을 공학석사 학위논문으로 제출함

2017년 6월

서울대학교 대학원
기계항공공학부
배 지 환

배지환의 공학석사 학위논문을 인준함

2017년 6월

위 원 장 _____

부위원장 _____

위 원 _____

Abstract

Development of Equilibrium Flow CFD Code Using CEA Database and Prediction on Ablation of SiC Coating Nozzle

Jihwan Bae
School of Mechanical and Aerospace Engineering
Seoul National University

This study was conducted with the aim such as development of ablation model of SiC due to combustion gas inside nozzle, prediction on ablation of SiC coating nozzle, development of ablation analysis code. For this purpose, equilibrium flow analysis code using CEA database and a structural temperature distribution analysis code had been developed and the reliability of the code had been secured by carrying out the validation process. These codes were coupled by transferring the wall heat flux and wall temperature as boundary conditions to each other, and the flow/structure integrated analysis code was developed. In order to develop the ablation model, the active and passive oxidation characteristics of SiC materials was investigated. The shear erosion model was developed to simulate mechanical ablation and the melting model was developed to simulate thermochemical ablation. The amount of ablation over time was predicted and compared with the measured amount of erosion depth of nozzle test delivered from the Agency for Defense Development.

Key Words: CFD, equilibrium flow, CEA, ablation, SiC, SiO_2
Student Number: 2015-20772

Contents

1. INTRODUCTION ····· 1

2. EQUILIBRIUM FLOW CODE DEVELOPMENT ····· 3
2.1. Flow type of a chemically reacting gas ····· 3
2.2. Governing equations for equilibrium flow ····· 4
2.3. Non-dimensionalization of governing equations ····· 6
2.4. Numerical method ····· 8
2.4.1. AUSMPW+ ····· 8
2.4.2. Time integration method : LU-SGS ····· 10
2.4.3. Time integration method : Dual time stepping ····· 12
2.5. Equilibrium flow analysis using CEA database ····· 13
2.5.1. CEA (Chemical Equilibrium with Applications) ····· 14
2.5.2. Free energy minimization method ····· 16
2.5.3. Thermodynamic properties and transfer coefficient of CEA ····· 18
2.5.3.1. Thermodynamic properties of CEA ····· 18
2.5.3.2. Transport coefficients of CEA ····· 18
2.5.4. Equivalent gamma using CEA database ····· 21
2.5.5. Utilization of CEA database ····· 23
2.5.6. CEA output verification ····· 27
2.5.6.1. Monotonic function ····· 27
2.5.6.2. Comparison of CEA GUI program output values and literature values ····· 28
2.5.6.3. Comparison of CEA GUI program output values and output values of bilinear interpolation function using table ····· 29
2.5.7. Precise verification of output values of bilinear interpolation function using table and table significant digits improvement 30
2.5.8. Generalization of Equilibrium Flow Codes ····· 35

3. FLOW/STRUCTURE INTEGRATED ANALYSIS CODE DEVELOPMENT ·· 36
3.1. Flow/structure integrated analysis code outline ····· 36
3.2. Algorithm of flow and structure analysis code coupling ····· 37
3.3. Structural analysis governing equation ····· 38
3.4. Boundary condition of Structure analysis code ····· 42
3.4.1. External boundary surface in contact with air ····· 42
3.4.2. Inner boundary surface ····· 42

4. VALIDATION OF FLOW/STRUCTURE INTEGRATED ANALYSIS CODE ····· 43
4.1. Validation of flow analysis code ····· 43
4.1.1. NASA CDV Nozzle study ····· 44
4.1.2. Validation of hypersonic flow on flat plate ····· 48
4.2. Validation of structure analysis code ····· 51

5. ABLATION MODEL ····· 55
5.1. SiC oxidation ····· 55
5.1.1. Passive oxidation ····· 55
5.1.2. Active oxidation ····· 56
5.1.3. Active to Passive Transition ····· 57
5.2. Mechanical ablation model ····· 61
5.3. Thermochemical ablation model ····· 61
5.3.1. Equilibrium gas kinetics ablation model ····· 61
5.3.2. Melting erosion model ····· 67

6. ANALYSIS OF ADD's NOZZLE ABLATION TEST RESULTS ····· 69

7. PREDICTION OF ABLATION USING INTEGRATED ANALYSIS CODE 71
7.1. Grid generation for flow and structure analysis ····· 71
7.1.1. Flow analysis grid ····· 71
7.1.2. Structure analysis grid and input material properties by position 72
7.2. Structure material properties correction ····· 75
7.3. Nozzle wall heat flux correction ····· 77

7.4. Physical time step setup ····· 83
7.5. Results of flow/structure integrated analysis code and discussion ····· 86
7.5.1. Results of equilibrium flow field analysis ····· 86
7.5.2. Results of structure temperature distribution analysis ····· 89
7.5.3. Wall heat flux, shear stress, and wall temperature distribution near the nozzle throat ····· 90
7.5.4. Prediction of the amount of SiC coating ablation ····· 92
7.5.4.1. Shear erosion prediction ····· 92
7.5.4.2. Melting erosion prediction ····· 93
7.5.4.3. Total erosion and comparison with measured values ·· 98

8. CONCLUSION ····· 102

9. REFERENCES ····· 104

국문 초록 ····· 108

List of Figures

Figure 1.1 SiC coating nozzle schematic and tested thruster of ADD ····· 2
Figure 2.1 CEA GUI program [Problem] tap ····· 15
Figure 2.2 CEA GUI program output plot window ····· 15
Figure 2.3 (T,p) Table example ····· 25
Figure 2.4 Schematic of bilinear interpolation ····· 26
Figure 2.5 Pressure distribution with (ρ,e) Table ····· 27
Figure 2.6 Density distribution with (T,p) Table ····· 27
Figure 2.7 Composition of equilibrium air versus temperature at 1 atm. (5 species) ····· 28
Figure 2.8 Composition of equilibrium nozzle combustion gas versus temperature at 1000 psi. (16 species) ····· 29
Figure 2.9 Composition of equilibrium nozzle combustion gas versus temperature at 2000 psi. (16 species) ····· 29
Figure 2.10 Stepwise result of molecular weight vs. pressure ····· 30
Figure 2.11 Stepwise result of enthalpy vs. pressure ····· 30
Figure 2.12 Stepwise result of internal energy vs. pressure ····· 30
Figure 2.13 Improved CEA table function energy output ····· 31
Figure 2.14 Improved CEA table function gamma output ····· 32
Figure 2.15 Improved CEA table function gamma output(zoomed in) ····· 32
Figure 2.16 Existing(left) and improved(right) (ρ,e) table example ····· 34
Figure 2.17 Input files required to create table ····· 35
Figure 3.1 Integrated code outline ····· 36
Figure 3.2 Flow/structural analysis code connection diagram ····· 37
Figure 3.3 Coordinate transformation using metric, ····· 39
Figure 3.4 External surface(left), Nozzle inner boundary surface (right) ····· 42
Figure 4.1 Converging-Diverging Verification(CDV) Nozzle (red is centerline) 44
Figure 4.2 NASA CDV Nozzle 51x31 grid ····· 45

Figure 4.3 CD Nozzle Axial Mach Number. Pexit = 0.75 psi (Shock in Diffuser) Developed CFD Code ····· 46
Figure 4.4 CD Nozzle Axial Static Pressure. Pexit = 0.75 psi (Shock in Diffuser) Developed CFD Code ····· 46
Figure 4.5 Mach number contours for CDV Nozzle of NASA ····· 47
Figure 4.6 Mach number contours for CDV Nozzle of Developed CFD Code ····· 47
Figure 4.7 Schematic of flat plate problem ····· 48
Figure 4.8 Flat plate problem 80x160 grid ····· 49
Figure 4.9 Flat plat wall pressure vs. x ····· 49
Figure 4.10 Gas composition of equilibrium air versus temperature at 1 bar. (5 species) using CEA database ····· 50
Figure 4.11 C_f vs. Re_x, Comparison with Van Driest's Analytic solution · 50
Figure 4.12 Cross-sectional schematic of flow filed of duct flow ····· 51
Figure 4.13 Duct flow axial velocity distribution contour ····· 53
Figure 4.14 Comparison between analytic solution and code result ····· 54
Figure 5.1 Pressure profiles of O2 and SiO for Wagner model ····· 58
Figure 5.2 Volatility diagram of SiC-O2-Ar system at 1873 K [14] ····· 58
Figure 5.3 Volatility diagram for the Si-C-O system between 1500 and 2300 K [22] ····· 59
Figure 5.6 Transition pressures for various oxidants (normalized per oxygen atom basis and stoichiometry factors) as compared to that calculated for O2 from reaction (12) [15] ····· 60
Figure 5.7 The main oxidation reaction formular of SiC ····· 62
Figure 5.8 Schematic of equilibrium gas kinetics ablation model ····· 63
Figure 5.9 Calculation of number density and molecular speed at 1400 K, 80 bar for equilibrium gas kinetics ablation model ····· 66
Figure 6.1 Erosion depth distribution graph by test ····· 70
Figure 7.1 Schematic of nozzle and nozzle flow region ····· 71
Figure 7.2 Nozzle flow grid, 190x120 cell ····· 72
Figure 7.3 Schematic of nozzle and nozzle structure region ····· 72

Figure 7.4 Nozzle structure grid, 190x240 cell ····· 73
Figure 7.5 Material distribution by position of nozzle structure ····· 74
Figure 7.6 Thermal transport coefficient distribution, original(left) and modified (right) ····· 75
Figure 7.7 Thermal conductivity distribution, original(left) and modified (right) ····· 76
Figure 7.8 Thermal transport coefficient vs. y at x=0.265 ····· 76
Figure 7.9 Thermal conductivity vs. y at x=0.265 ····· 77
Figure 7.10 Diverged wall temperature and heat flux at nozzle throat ····· 78
Figure 7.11 Verification of reason of heat flux oscillation ····· 78
Figure 7.12 Corrected heat flux example ····· 80
Figure 7.13 Wall temperature over time with correction, before(left) and after(right) ····· 81
Figure 7.14 Wall temperature and heat flux of verification case with correction, before(left) and after(right) ····· 81
Figure 7.15 Wall heat flux at nozzle throat over time, comparison by flow type, 3rd test ····· 82
Figure 7.16 Wall temperature at nozzle throat over time, 3rd test ····· 83
Figure 7.17 Wall heat flux at nozzle throat over time (Calorically perfect gas), comparison by physical time step variation. right graph is zoomed in ····· 85
Figure 7.18 Wall temperature at nozzle throat over time (Calorically perfect gas), comparison by physical time step variation. right graph is zoomed in ····· 85
Figure 7.19 Material distribution of nozzle structure around nozzle throat (zoomed in) ····· 86
Figure 7.20 Mach number contour, t=0.000 s, 3rd test (bottom contour is zoomed in around nozzle throat) ····· 87
Figure 7.21 Temperature contour, t=0.000 s, 3rd test (bottom contour is zoomed in around nozzle throat) ····· 87
Figure 7.22 Pressure contour, t=0.000 s, 3rd test (bottom is zoomed in around nozzle throat) ····· 88

Figure 7.23 Nozzle wall pressure distribution ····· 88
Figure 7.24 Temperature distribution of nozzle structure, t=14.000 s, 3rd test, right contour is zoomed in ····· 89
Figure 7.25 Temperature distribution of nozzle structure, t=19.000 s, 4th/5th test, right contour is zoomed in ····· 89
Figure 7.26 Wall heat flux distribution around nozzle throat over time, 3rd test(left) and 4th/5th test(right) ····· 90
Figure 7.27 Wall shear stress distribution around nozzle throat over time, 3rd test(left) and 4th/5th test(right) ····· 91
Figure 7.28 Wall temperature distribution around nozzle throat over time, 3rd test(left) and 4th/5th test(right) ····· 92
Figure 7.29 Shear erosion distribution around nozzle throat over time, 3rd test(left) and 4th/5th test(right) ····· 92
Figure 7.30 Thermal conductivity of various SiO_2 samples with porosity property[32] ····· 94
Figure 7.31 Tested nozzle surface. Porous SiO_2 layer is zoomed in (right) · 96
Figure 7.32 Melting erosion distribution around nozzle throat over time, 3rd test(left) and 4th/5th test(right) ····· 98
Figure 7.33 Total erosion distribution around nozzle throat over time, 3rd test(left) and 4th/5th test(right) ····· 99
Figure 7.34 Erosion depth comparison of 3rd test ····· 100
Figure 7.35 Erosion depth comparison of 4th and 5th test ····· 101
Figure 7.36 Erosion depth comparison of 4th and 5th test, modified shear/melting erosion model ····· 101

List of Tables

Table 2.1 Nozzle combustion gas mole fraction at 2750 K, 2500 psi ····· 24
Table 2.2 Verification of interpolation function improvement using (T,p) table ····· 33
Table 2.3 Verification of interpolation function improvement using (ρ,e) table ····· 33
Table 4.1 CDV Nozzle problem flow condition ····· 44
Table 4.2 Flat plate problem free stream condition ····· 48
Table 4.3 Duct flow problem condition ····· 53
Table 5.1 Passive oxidation reaction equations ····· 56
Table 5.2 Active oxidation reaction equations ····· 57
Table 5.3 Partial pressure of combustion gas at 80 bar, 1400 K ····· 67
Table 6.1 Summary of 3rd～5th test environment for combustion ····· 69
Table 7.1 Material properties (density, specific heat capacity, thermal conductivity) ····· 74
Table 7.2 Number of physical time step, target time and time step summary 84
Table 7.3 Thermal conductivity of SiO_2 with porosity by DEM theory ····· 95

1

INTRODUCTION

In the process of developing a high-performance rocket propulsion system, a material having excellent ablation resistance is required to withstand the high temperature/high pressure combustion gas. When the rocket is operated, high temperature/high pressure combustion gas is discharged from the combustion chamber and ablation phenomenon occurs due to the collision of the combustion gas on the nozzle surface. The nozzle throat is the area where the thermal load is most concentrated, and also the area where the shear force is very high due to the expansion of the flow and the change of the flow direction. Therefore, the ablation occurs intensively around the nozzle throat and the nozzle throat area increases due to erosion. It is very important to predict the amount of ablation of nozzle throat during rocket operating times because the increased throat area will cause changes in the rocket plume characteristics and will directly affect the rocket performance.

In this study, analysis is conducted about the ablation phenomenon of SiC coated nozzle which is known to be excellent in ablation resistance. Therefor, two main objectives are as follows:

1) to achieve a technique to predict the amount of nozzle erosion due to combustion gases by analyzing the ablation characteristics of SiC
2) to develop ablation analysis codes.

To accomplish the objectives, first development of equilibrium code is preceded to analyze the nozzle combustion gas. And structure analysis code is also needed to be developed to obtain the temperature distribution of nozzle structure and to calculate the ablation depth. Since SiC has active and passive oxidation characteristics, it should be reflected in the development of the ablation model. After developing integrated code by coupling the flow analysis code and the structure analysis code, the developed code predicts the amount of nozzle erosion and then the value is compared with the nozzle test result data from ADD(Agency for Defense Development).

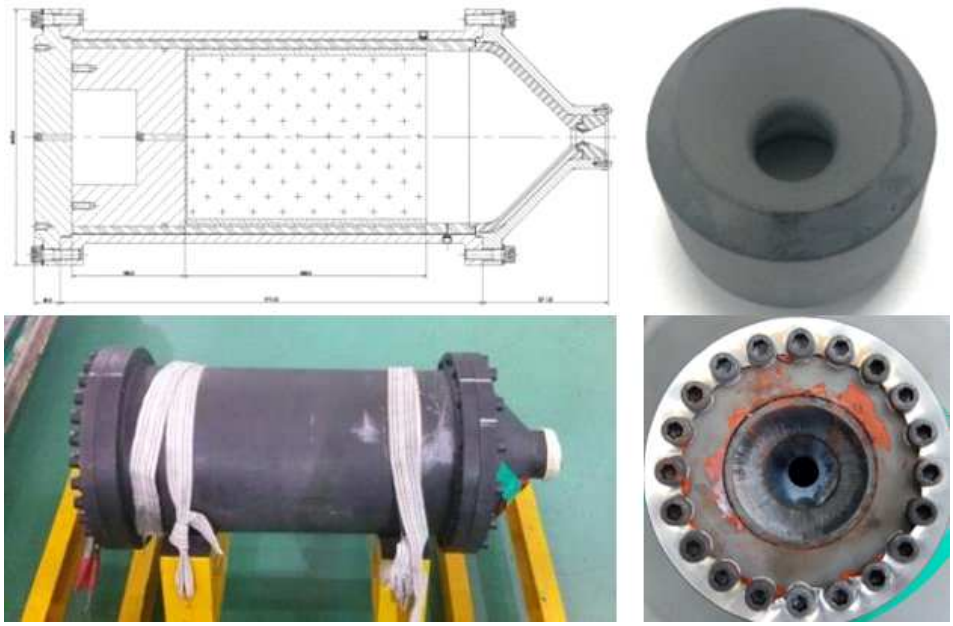

Figure 1.1 SiC coating nozzle schematic and tested thruster of ADD

2

EQUILIBRIUM FLOW CODE DEVELOPMENT

2.1. Flow type of a chemically reacting gas

Let's say that the time it takes for the reacting gas to flow over a certain distance is $\triangle t_f$, and the time taken to reach at the thermochemical equilibrium state through chemical reaction is called $\triangle t_c$. The flow type then could be set by comparing $\triangle t_f$ and $\triangle t_c$. The faster the flow velocity, the less the time($\triangle t_f$) it takes to travel a certain distance. Since the chemical reaction rate increases in proportion to the collision frequency of gas particles, as the temperature increases and the kinetic velocity of the gas particles increases, the reacting gas reaches the equilibrium state sooner due to the increased reaction rate and $\triangle t_c$ becomes smaller. The flow type is classified as follows by comparing two characteristic times.

$\triangle t_f \gg \triangle t_c$: Equilibrium Flow

$\triangle t_f \approx \triangle t_c$: Nonequilibrium Flow

$\triangle t_f \ll \triangle t_c$: Frozen Flow

If the reaction takes place quickly and the time $\triangle t_c$ to reach equilibrium is much less than the time $\triangle t_f$ the flow travels at a certain distance, it can be said that whenever the flow moves instantaneously, the chemical reaction

occurs sufficiently to reach an equilibrium state. This flow is called the equilibrium flow. If the reaction does not occur or occurs very slowly, the time $\triangle t_c$ is much greater than $\triangle t_f$, so it can be assumed that the chemical reaction does not occur when the flow moves, and this flow is called the frozen flow. If $\triangle t_f$ and $\triangle t_c$ are at similar levels, the flow properties must be calculated taking into account the amount of each individual chemical species produced or lost by finite chemical reaction rate. This flow is called non-equilibrium flow. Of course, a chemically reacting real gas flow has a finite reaction rate and neither equilibrium flow or frozen flow having infinite or zero reaction rate actually occurs, but it can be assumed with above descriptions.[1]

2.2. Governing equations for equilibrium flow

In order to analyze the high-temperature equilibrium flows with chemical reaction, the derivations of the conventional governing equations were examined. Continuity equation is just a expression of mass conservation and momentum equation is based on Newton's 2nd law and each one is independent of the presence or absence of a chemical reaction. Finally, we can derive the energy equation from the 1st and 2nd laws of thermodynamics, which hold for any type of gas. Accordingly, two-dimensional, axisymmetric governing equation for equilibrium flows is written as follows. The governing equations consist of continuity, momentum equations and energy equation, and energy transport by the diffusion and radiation effects is not considered. The ideal gas equation is required to solve the governing equations.

Continuity equation

$$\frac{\partial \rho}{\partial t}+\frac{\partial \rho u}{\partial x}+\frac{\partial \rho v}{\partial y}+\frac{\rho y}{y}=0 \tag{2.1}$$

Momentum equation(x-direction, axial direction)

$$\frac{\partial \rho u}{\partial t}+\frac{\partial(\rho u^2+p)}{\partial x}+\frac{\partial \rho uv}{\partial y}+\frac{\rho uv}{y}=\frac{\partial \tau_{xx}}{\partial x}+\frac{\partial \tau_{xy}}{\partial y}+\frac{1}{y}\left[\tau_{xy}-\frac{2}{3}y\frac{\partial}{\partial x}\left(\mu\frac{v}{y}\right)\right] \quad (2.2)$$

$$\tau_{xx}=\frac{4}{3}\mu\frac{\partial u}{\partial x}-\frac{2}{3}\mu\frac{\partial v}{\partial y},\ \tau_{xy}=\mu\left(\frac{\partial u}{\partial y}+\frac{\partial v}{\partial x}\right) \quad (2.3)$$

Momentum equation(y-direction, radial direction)

$$\begin{aligned}&\frac{\partial \rho v}{\partial t}+\frac{\partial \rho uv}{\partial x}+\frac{\partial(\rho v^2+p)}{\partial y}+\frac{\rho v^2}{y}\\&=\frac{\partial \tau_{xy}}{\partial x}+\frac{\partial \tau_{yy}}{\partial y}+\frac{1}{y}\left[\tau_{yy}-\tau_{\theta\theta}-\frac{2}{3}\left(\mu\frac{v}{y}\right)-\frac{2}{3}y\frac{\partial}{\partial y}\left(\mu\frac{v}{y}\right)\right]\end{aligned} \quad (2.4)$$

$$\tau_{yy}=\frac{4}{3}\mu\frac{\partial v}{\partial y}-\frac{2}{3}\mu\frac{\partial u}{\partial x},\ \tau_{\theta\theta}=\mu\left(\frac{4}{3}\frac{v}{y}-\frac{2}{3}\left(\frac{\partial u}{\partial x}+\frac{\partial v}{\partial u}\right)\right) \quad (2.5)$$

Energy equation

$$\begin{aligned}&\frac{\partial \rho e_t}{\partial t}+\frac{\partial(\rho e_t+p)u}{\partial x}+\frac{\partial(\rho e_t+p)v}{\partial y}+\frac{(\rho e_t+p)v}{y}\\&=-\frac{\partial q_x}{\partial x}-\frac{\partial q_y}{\partial y}+\frac{\partial \tau_{xx}u}{\partial x}+\frac{\partial \tau_{xy}u}{\partial y}+\frac{\partial \tau_{yx}v}{\partial x}+\frac{\partial \tau_{yy}v}{\partial y}\\&+\frac{1}{y}\left[u\tau_{xy}+v\tau_{yy}-q_y-\frac{2}{3}\left(\mu\frac{v^2}{y}\right)-\frac{2}{3}y\frac{\partial}{\partial y}\left(\mu\frac{v^2}{y}\right)-\frac{2}{3}y\frac{\partial}{\partial x}\left(\mu\frac{uv}{y}\right)\right]\end{aligned} \quad (2.6)$$

$$q_x=-k\frac{\partial T}{\partial x},\ q_y=-k\frac{\partial T}{\partial y} \quad (2.7)$$

Equation of state

$$p=\left(\sum_s \rho_s R_s\right)T=\left(\sum_s \rho_s\frac{\overline{R}}{M_s}\right)T=\rho\left(\frac{\overline{R}}{\sum_s X_s M_s}\right)T \quad (2.8)$$

ρ : density

μ : viscosity

u : x-direction velocity

τ_{ij} : viscous stress tensor

v : y-direction velocity

t : time

p : pressure

e : internal energy

T : temperature

h : enthalpy

Re : Reynolds number

M : Mach number

X_s : mole fraction of species s

k : thermal conductivity

q_i : conductive heat flux

e_t : total energy $= e + 0.5(u^2 + v^2)$

M_s : molecular weight of species s

ρ_s : density of species s

R_s : gas constant of species s

$\overline{R}$: ideal gas constant

Pr : Prandtl number

2.3. Non-dimensionalization of governing equations

In order to avoid the numerical errors such as the non-associativity of arithmetics due to the difference of order of magnitude between the variables, each variable was non-dimensionalized as follows. The subscript ∞ refers to free flow, which is the reference value for non-dimensionalization, and the superscript * refers to the dimensionless variables. And L and c respectively denote characteristic length and speed of sound.

$$\rho = \rho_\infty \rho^*,\ u = c_\infty u^*,\ v = c_\infty v^*,\ x = L_\infty x^*,\ y = L_\infty y^*,\ p = \rho_\infty c_\infty p^*$$

$$\tau = \mu_\infty \frac{c_\infty}{L_\infty}\tau^*,\ e_t = c_\infty^2 e_t^*,\ h = c_\infty^2 h^*,\ q = k_\infty \frac{T_\infty}{L_\infty} q^*$$

$$\mu = \mu_\infty \mu^*,\ k = k_\infty k^*,\ \frac{1}{Re_\infty} = \frac{\mu_\infty}{\rho_\infty u_\infty L_\infty},\ M_\infty = \frac{u_\infty}{c_\infty} \tag{2.9}$$

The non-dimensional governing equations are expressed in vector form as follows. If a is 0 then it is a planar flow and if a is 1 it is an axisymmetric flow. For the sake of convenience, * is omitted.

$$\frac{\partial Q}{\partial t}+\frac{\partial E}{\partial x}+\frac{\partial F}{\partial y}+aH=\frac{\partial E_v}{\partial x}+\frac{\partial F_v}{\partial y}+aH_v \tag{2.10}$$

$$Q=\begin{pmatrix}\rho\\ \rho u\\ \rho v\\ \rho e_t\end{pmatrix},\ E=\begin{pmatrix}\rho u\\ \rho u^2+p\\ \rho uv\\ (\rho e_t+p)u\end{pmatrix},\ F=\begin{pmatrix}\rho v\\ \rho uv\\ \rho v^2+p\\ (\rho e_t+p)v\end{pmatrix},\ H=\frac{1}{y}\begin{pmatrix}\rho v\\ \rho uv\\ \rho v^2\\ \rho v(e_t+p/\rho)\end{pmatrix}$$

$$E_v=\begin{pmatrix}0\\ \dfrac{M_\infty}{Re_\infty}\tau_{xx}\\ \dfrac{M_\infty}{Re_\infty}\tau_{xy}\\ -\dfrac{M_\infty}{Re_\infty}\dfrac{1}{\mathrm{Pr}_\infty(\gamma_\infty-1)}q_x+\dfrac{M_\infty}{Re_\infty}(\tau_{xx}u+\tau_{xy}v)\end{pmatrix}$$

$$F_v=\begin{pmatrix}0\\ \dfrac{M_\infty}{Re_\infty}\tau_{xy}\\ \dfrac{M_\infty}{Re_\infty}\tau_{yy}\\ -\dfrac{M_\infty}{Re_\infty}\dfrac{1}{\mathrm{Pr}_\infty(\gamma_\infty-1)}q_y+\dfrac{M_\infty}{Re_\infty}(\tau_{xy}u+\tau_{yy}v)\end{pmatrix}$$

$$H_v=\frac{1}{y}\begin{pmatrix}0\\ \dfrac{M_\infty}{Re_\infty}\left[\tau_{xy}-\dfrac{2}{3}y\dfrac{\partial}{\partial x}\left(\mu\dfrac{v}{y}\right)\right]\\ \dfrac{M_\infty}{Re_\infty}\left[\tau_{xy}-\dfrac{2}{3}y\dfrac{\partial}{\partial x}\left(\mu\dfrac{v}{y}\right)-\dfrac{2}{3}y\dfrac{\partial}{\partial y}\left(\mu\dfrac{v}{y}\right)\right]\\ \dfrac{M_\infty}{Re_\infty}\left[u\tau_{xy}+v\tau_{yy}-q_y-\dfrac{2}{3}\left(\mu\dfrac{v^2}{y}\right)-\dfrac{2}{3}y\dfrac{\partial}{\partial y}\left(\mu\dfrac{v^2}{y}\right)-\dfrac{2}{3}y\dfrac{\partial}{\partial x}\left(\mu\dfrac{uv}{y}\right)\right]\end{pmatrix}$$

2.4. Numerical method

In order to numerically calculate equilibrium flow governing equations, the code was developed using the following numerical techniques.

- Inviscid flux : AUSMPW+
- Limiter : Minmod Limiter
- Viscous flux : 2nd order CD
- Time integration : LU-SGS, Dual time stepping method

2.4.1. AUSMPW+

AUSMPW+ is a numerical flux technique designed to eliminate the numerical vibration phenomenon, maintaining the efficiency and accuracy of the AUSM-type by appropriately adjusting the advection characteristic using the pressure-weighted function in the region of the numerical vibration as in the vicinity of the shock wave or the wall.[2]

The numerical flux of AUSMPW+ has the following form.

$$\boldsymbol{F_{1/2}} = \overline{M}_L^+ c_{1/2} \boldsymbol{\Phi_L} + \overline{M}_R^- c_{1/2} \boldsymbol{\Phi_R} + (P_L^+ \boldsymbol{P_L} + P_R^- \boldsymbol{P_R}) \tag{2.11}$$

$\boldsymbol{\Phi} = (\rho, \rho u, \rho H)^T$, $\boldsymbol{P} = (0, p, 0)^T$, and subscripts $1/2$ and (L, R) represents the cell interface and left and right sides of the cell interface respectively. The Mach number at the cell interface is defined as:

$$m_{1/2} = M_L^+ + M_R^+ \tag{2.12}$$

$\overline{M}_{L,R}^{\pm}$ is the Mach number interpolation function, which depends on the Mach number at the interface.

(1) $m_{\frac{1}{2}} = M_L^+ + M_R^- \geq 0$,

$$\begin{aligned} \overline{M}_L^+ &= M_L^+ + M_R^- \cdot [(1-w)\cdot(1+f_R) - f_L], \\ \overline{M}_R^- &= M_R^- \cdot w \cdot (1+f_R) \end{aligned} \tag{2.13}$$

(2) $m_{\frac{1}{2}} < 0$,

$$\begin{aligned} \overline{M}_L^+ &= M_L^+ \cdot w \cdot (1+f_L) \\ \overline{M}_R^- &= M_R^- + M_L^+ \cdot [(1-w)\cdot(1+f_L) - f_R] \end{aligned} \tag{2.14}$$

The function f and w are pressure-weighted functions and are given by

$$w(p_L, p_R) = 1 - \min\left(\frac{p_L}{p_R}, \frac{p_R}{p_L}\right)^3 \tag{2.15}$$

$$f_{L,R} = \left(\frac{p_{L,R}}{p_s} - 1\right) \times \min\left(1, \frac{\min(p_{1,L}, p_{1,R}, p_{2,L}, p_{2,R})}{\min(p_L, p_R)}\right)^2, p_s \neq 0 \tag{2.16}$$

where $p_s = P_L^+ p_L + P_R^- p_R$.

The split Mach number and pressure of AUSMPW+ are given by

$$M^{\pm} = \begin{cases} \pm\frac{1}{4}(M \pm 1)^2, & |M| \leq 1 \\ \frac{1}{2}(M \pm |M|), & |M| > 1 \end{cases} \tag{2.17}$$

$$P^{\pm} = \begin{cases} \frac{1}{4}(M \pm 1)^2 (2 \mp M), & |M| \leq 1 \\ \frac{1}{2}(1 \pm sign(M)), & |M| > 1 \end{cases} \tag{2.18}$$

The Mach number and speed of sound at the cell interface are defined as

$$M_{L,R} = \frac{U_{L,R}}{c_{1/2}} \tag{2.19}$$

$$c_{1/2} = \min\left(c_s^2/\max(|U_L|, c_s), c_s^2/\max(|U_R|, c_s)\right) \tag{2.20}$$

Where c_s is given as follows. H means total enthalpy.

$$c_s = \sqrt{\frac{2(\gamma-1)}{(\gamma+1)H_{normal}}}, \quad H_{normal} = 0.5(H_L - 0.5\,V_L^2 + H_R - 0.5\,V_R^2) \tag{2.21}$$

2.4.2. Time integration method : LU-SGS

The time integration method applied to this study is the Lower-Upper Symetric Gauss-Seidel (LU-SGS) method developed by Yoon and Jameson. [3] The LU-SGS method does not require inverse operation of the matrix, so the required memory usage and computation time are reduced, and the converged solution can be obtained very efficiently.

The process for deriving the LU-SGS method is as follows. First, the governing equations after the conversion of the physical domain (x,y) into the computational domain (ξ,η) can be expressed as the following equation.

$$\frac{\partial(Q/J)}{\partial t} + \frac{\partial \overline{E}}{\partial \xi} + \frac{\partial \overline{F}}{\partial \eta} + a\overline{H} = \frac{\partial \overline{E}_v}{\partial \xi} + \frac{\partial \overline{F}_v}{\partial \eta} + a\overline{H_v} \tag{2.22}$$

$$J = \frac{\partial(\xi,\eta)}{\partial(x,y)}, \quad \overline{E} = Ey_\eta - Fx_\eta, \quad \overline{E_v} = E_v y_\eta - F_v x_\eta$$

$$\overline{F} = -Ey_\xi + Fx_\xi, \quad \overline{F_v} = -E_v y_\xi + F_v x_\xi, \quad \overline{H} = H/J, \quad \overline{H_v} = H_v/J$$

Because of the computational complexity to handle all the terms of the governing equations implicitly, the high stiffness terms were treated implicitly. The viscous flux and axisymmetric terms are processed explicitly as follows.

$$\frac{Q^{n+1}-Q^n}{J\Delta t}+\frac{\partial \overline{E}}{\partial \xi}^{n+1}+\frac{\partial \overline{F}}{\partial \eta}^{n+1}+a\overline{H}^n=\frac{\partial \overline{E}_v}{\partial \xi}^{n}+\frac{\partial \overline{F}_v}{\partial \eta}^{n}+a\overline{H_v}^n \quad (2.23)$$

Equation (2.23) can be rewritten as

$$\left(\frac{I}{J\Delta t}+\frac{\partial A^n}{\partial \xi}+\frac{\partial B^n}{\partial \eta}\right)_{i,j}\Delta Q_{i,j}^n=-R_{i,j}^n \quad (2.24)$$

Where,

$$\Delta Q^n=Q^{n+1}-Q^n \quad (2.25)$$

$$\overline{E}^{n+1}\cong\overline{E}^n+\left(\frac{\partial \overline{E}}{\partial Q}\right)^n\Delta Q,\ \ \overline{F}^{n+1}\cong\overline{F}^n+\left(\frac{\partial \overline{F}}{\partial Q}\right)^n\Delta Q \quad (2.26)$$

$$A^n=\left(\frac{\partial \overline{E}}{\partial Q}\right)^n,\ \ B^n=\left(\frac{\partial \overline{F}}{\partial Q}\right)^n \quad (2.27)$$

$$-R^n=-\frac{\partial \overline{E}^n}{\partial \xi}-\frac{\partial \overline{F}^n}{\partial \eta}+\frac{\partial \overline{E}_v^n}{\partial \xi}+\frac{\partial \overline{F}_v^n}{\partial \eta}+a\left(\overline{H_v}^n-\overline{H}^n\right) \quad (2.28)$$

The equation (2.24) can be converted into the following equation (2.29) through LU factorization. λ means the eigenvalue of the matrix.

$$LD^{-1}U\Delta Q_{i,j}^n=-R_{i,j}^n \quad (2.29)$$

Where,

$$L=\left(\frac{1}{J\Delta t}+\rho_A+\rho_B\right)_{i,j}I-A_{i-1,j}^+-B_{i-1,j}^+ \quad (2.30)$$

$$D=\left(\frac{1}{J\Delta t}+\rho_A+\rho_B\right)_{i,j}I \quad (2.31)$$

$$U=\left(\frac{1}{J\Delta t}+\rho_A+\rho_B\right)_{i,j}I+A_{i+1,j}^-+B_{i+1,j}^- \quad (2.32)$$

$$A^{\pm}=\frac{1}{2}(A\pm\rho_A I),\ \ B^{\pm}=\frac{1}{2}(B\pm\rho_B I) \tag{2.33}$$

$$\rho_A \geq \max(|\lambda_A|),\ \ \rho_B \geq \max(|\lambda_B|) \tag{2.34}$$

$$K_{i,j}=\left(\frac{1}{J\triangle t}+\rho_A+\rho_B\right)_{i,j} \tag{2.34}$$

If set $D^{-1}U\triangle Q_{i,j}^{n}=\triangle Q_{i,j}^{*}$ in Equation (2.29), the LU-SGS method can be expressed in a 2-step iterative form.

$$L\triangle Q_{i,j}^{*}=-R_{i,j}^{n} \tag{2.35}$$

$$U\triangle Q_{i,j}^{n}=D\triangle Q_{i,j}^{*} \tag{2.36}$$

Lower sweep

$$L\triangle Q_{i,j}^{*}=\left[K_{i,j}I-A_{i-1,j}^{+}-B_{i-1,j}^{+}\right]\triangle Q_{i,j}^{*}=-R_{i,j}^{n} \tag{2.37}$$

$$\triangle Q_{i,j}^{*}=K_{i,j}^{-1}\left(-R_{ij}^{n}+A_{i-1,j}^{+}\triangle Q_{i-1,j}^{*}+B_{i,j-1}^{+}\triangle Q_{i,j-1}^{*}\right) \tag{2.38}$$

Upper sweep

$$U\triangle Q_{i,j}^{n}=\left[K_{i,j}I+A_{i+1,j}^{-}+B_{i+1,j}^{-}\right]\triangle Q_{i,j}^{n}=D\triangle Q_{i,j}^{*} \tag{2.39}$$

$$\triangle Q_{i,j}^{n}=K_{i,j}^{-1}\left(D\triangle Q_{i,j}^{*}-A_{i+1,j}^{-}\triangle Q_{i+1,j}^{n}+B_{i,j+1}^{-}\triangle Q_{i,j+1}^{n}\right) \tag{2.40}$$

Finally, we can find the solution through the above process.

$$Q_{i,j}^{n+1}=Q_{i,j}^{n}+\triangle Q_{i,j}^{n} \tag{2.41}$$

2.4.3. Time integration method : Dual time stepping

The dual time stepping method is a technique of introducing a pseudo-time concept and advancing the physical time after pseudo-time convergence internally.

By applying pseudo-time τ and expressing the unsteady governing equation,

$$\frac{\partial Q}{\partial \tau} = -\left[\frac{\partial Q}{\partial t} + R(Q)\right] = -R^*(Q) \tag{2.42}$$

When the above equation converges with respect to the pseudo-time, the derivative value of Q with respect to τ becomes zero. Therefore, instead of solving the equation for each physical time interval, it is changed to the method calculating the steady state in pseudo-time. If we use the 2nd order backward differencing to express the differential term of the physical time, the above equation can be written as

$$\frac{\partial Q}{\partial \tau} = \frac{3Q^{m+1} - 4Q^m + Q^{m-1}}{2\triangle t} + R(Q^{m+1}) = R^*(Q) \tag{2.43}$$

Where the superscript m denotes the physical time step index.

2.5. Equilibrium flow analysis using CEA database

For the chemically reacting flow analysis, the thermodynamic properties of equilibrium flow should be given to calculate the governing equations. First, The mole fraction of the chemical species for the reacting flow should be calculated according to the given thermodynamic conditions. We should also obtain the properties such as temperature, pressure, enthalpy, transfer coefficient (viscous coefficient, thermal conductivity), specific heat ratio and speed of sound of the equilibrium state.

In the process of solving the governing equations, two methods are needed to obtain equilibrium chemical composition(mole fraction) and flow properties. The first is the calculation using density and internal energy, and the second is the calculation using temperature and pressure. Since the known values of

the thermodynamic variables in the flow governing equations are density(ρ) and internal energy(e), a method is necessary to calculate the equilibrium state properties such as temperature and pressure using these variables. Also, the thermodynamic variables known in isothermal wall boundary conditions of viscous flow are temperature(T) and pressure(p), so a method of calculating necessary properties to solve the governing equations by using temperature and pressure is needed. Conceptually, these method to obtain the properties could be written as

$$T = T(\rho, e), \quad p = p(\rho, e) \tag{2.44}$$

$$\mu = \mu(T, p), \quad \gamma = \gamma(T, p) \tag{2.45}$$

CEA was used to achieve both methods.

2.5.1. CEA (Chemical Equilibrium with Applications)

In this study, the CEA database is used to calculate mole fraction and thermodynamic flow properties in the equilibrium state. CEA is a program for calculating thermodynamic properties of chemical equilibrium mixtures developed by NASA's Glenn Research Center.[4][5] CEA provides a database of thermodynamic properties for over 2000 different chemical species and includes commonly used air and combustion gas species.

Using the CEA GUI program, we can select several problem types (t,p), (h,p), and (u,v) on the [Problem] tab(Figure 2.1). After selecting the problem type, the kind of chemical species, the initial mole fraction, and the input condition are entered and calculated. Then, various thermodynamic properties as well as the mole fraction of each species in the equilibrium state are calculated and can be output selectively. The output value is the 5 significant digits as shown in Figure 2.2

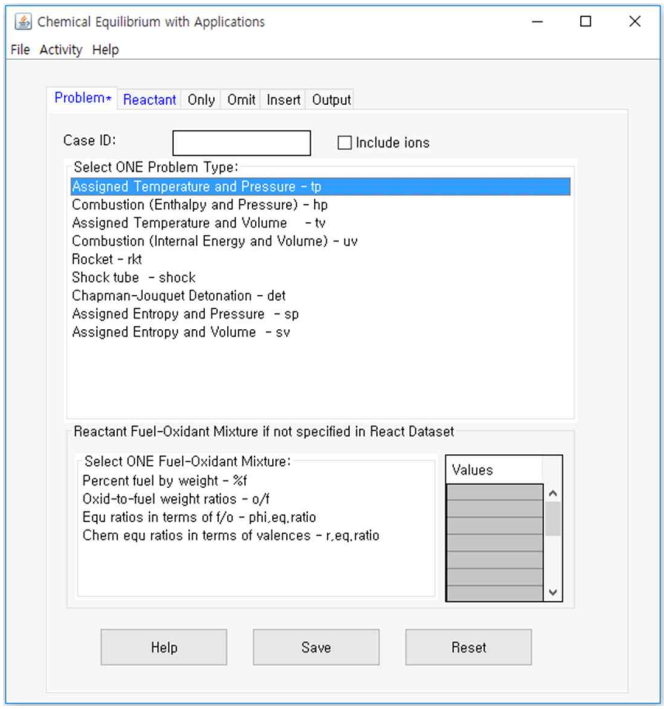

Figure 2.1 CEA GUI program [Problem] tap

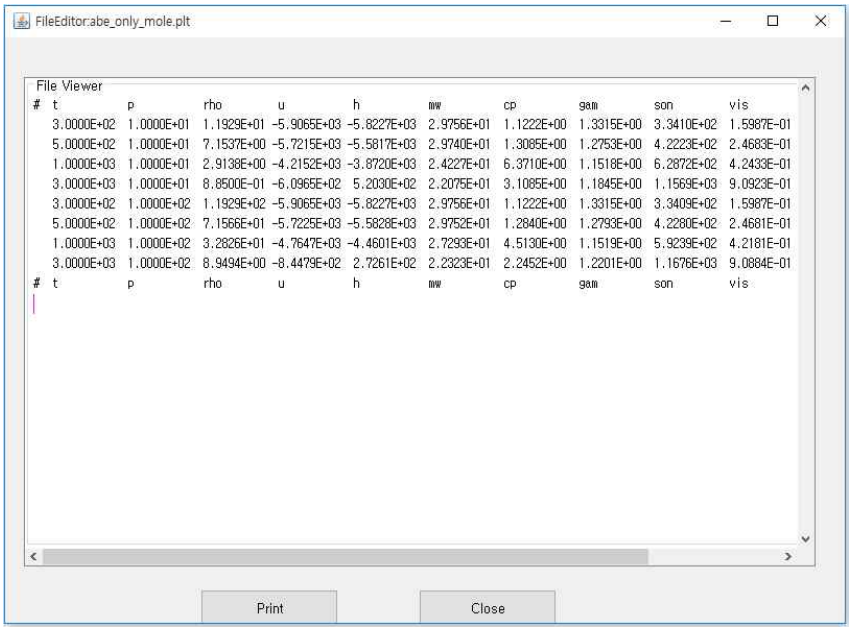

Figure 2.2 CEA GUI program output plot window

2.5.2. Free energy minimization method

CEA uses the free energy minimization method to calculate the equilibrium chemical composition. The free energy minimization method is a different way of expression of the 2nd law of thermodynamics.

$$\oint \frac{\delta Q}{T} \leq 0 \tag{2.46}$$

The above equation is the Clausius theorem. When the cycle is calculated, the equal sign is established only when the cycle is reversible, and the inequality is established when the cycle is irreversible. If the cycle goes from state A to state B in a irreversible process and returns from state B to state A in a reversible process, Clausius theorem can be expressed as following equations. s denotes the entropy, and subscripts Rev, e denote when heated reversibly, and subscripts Irr when irreversibly heated.

$$\oint \frac{\delta Q}{T} = \left(\int_A^B \frac{\delta Q_{Irr}}{T} - \int_A^B \frac{\delta Q_{Rev}}{T} \right) \leq 0 \tag{2.47}$$

$$\int_A^B \frac{\delta Q_{Irr}}{T} \leq \int_A^B \frac{\delta Q_{Rev}}{T} = s(B) - s(A) \tag{2.48}$$

$$\frac{\delta Q_{Irr}}{T} \leq ds \tag{2.49}$$

Since δQ is zero in the adiabatic system, ds is always equal to or greater than zero($ds \geq 0$). Let the entropy of this adiabatic condition be ds_i, and let the total entropy heated by the reversible process be ds, the second law of thermodynamics can be expressed as

$$ds = \frac{\delta Q_{Rev}}{T} + ds_i = ds_e + ds_i \quad (ds_i \geq 0) \tag{2.50}$$

Using the alternate expression of 2nd law of thermodynamics, the amount of change of the Helmholtz free energy and the Gibbs free energy can be expressed as follows. E means internal energy.

T, V : Constant

$$F \equiv E - Ts : Helmholtz\ free\ energy \tag{2.51}$$

$$\begin{aligned} dF &= dE - Tds \\ &= \delta Q - Tds \\ &= Tds_e - Tds = -Tds_i \le 0 \quad (\because ds_i \ge 0) \end{aligned} \tag{2.52}$$

T, p : Constant

$$G \equiv E - Ts + pV : Gibbs\ free\ energy \tag{2.53}$$

$$\begin{aligned} dG &= dE - Tds + pdV \\ &= \delta Q - pdV - Tds + pdV \\ &= Tds_e - Tds = -Tds_i \le 0 \quad (\because ds_i \ge 0) \end{aligned} \tag{2.54}$$

Entropy always increases during the chemical reaction in a constant temperature/volume or temperature/pressure system, starting from the initial non-equilibrium state. From the results of Equation (2.52) and (2.54), as entropy increases, the amount of free energy is always less than 0, so the free energy decreases. If the system becomes the equilibrium state and the entropy no longer increases, the amount of free energy change becomes zero, so that the free energy reaches the minimum value. Helmholtz free energy minimization is used for systems with assigned temperature/volume (or internal energy/density), and Gibbs free energy minimization is used for systems with assigned temperature/pressure. CEA uses the free energy minimization method to calculate the equilibrium chemical composition(mole fraction) at which the sum of the free energy of a mixture is minimized under a given condition. The thermodynamic properties in equilibrium state can be obtained by calculating the properties of each species and then taking the average using the

mole fraction. The method of obtaining the properties of each chemical species is introduced in section 2.5.3.

2.5.3. Thermodynamic properties and transfer coefficient of CEA

2.5.3.1. Thermodynamic properties of CEA

CEA calculates the specific heat, enthalpy, and entropy of each species using a function of temperature. The function is expressed as least-squares coefficients, and the coefficients can be found in the 'thermo.inp' file included when downloading the CEA GUI program from the NASA's GRC homepag e.[1] In the following functions, C_p°, H°, S°, R, T are specific heat, enthalpy, entropy, ideal gas constant, and temperature, respectively.

$$\frac{C_p^\circ}{R} = a_1 T^{-2} + a_2 T^{-1} + a_3 + a_4 T + a_5 T^2 + a_6 T^3 + a_7 T^4 \tag{2.55}$$

$$\frac{H^\circ}{RT} = -a_1 T^{-2} + a_2 T^{-1} \ln T + a_3 + a_4 \frac{T}{2} + a_5 \frac{T^2}{3} + a_6 \frac{T^3}{4} + a_7 \frac{T^4}{5} + \frac{a_8}{T} \tag{2.56}$$

$$\frac{S^\circ}{R} = -a_1 \frac{T^{-2}}{2} - a_2 T^{-1} + a_3 \ln T + a_4 T + a_5 \frac{T^2}{2} + a_6 \frac{T^3}{3} + a_7 \frac{T^4}{4} + a_9 \tag{2.57}$$

2.5.3.2. Transport coefficients of CEA

In order to calculate the equilibrium state viscosity and thermal conductivity of a mixture, CEA first uses a function to calculate the viscosity and thermal conductivity for each chemical species forming the mixture. The function is given by the following equation (2.58), where η denotes the viscous coefficient and λ denotes the thermal conductivity. The coefficients of each chemical species can be found in the 'trans.inp' file included when downloading the CEA GUI program.

---

1) http://www.grc.nasa.gov/WWW/CEAWeb/ceaguiDownload-win.htm

$$A\ln T+\frac{B}{T}+\frac{C}{T^2}+D=\begin{cases}\ln\eta\\ \ln\lambda\end{cases} \tag{2.58}$$

After calculating the viscosity and thermal conductivity of each species, CEA begins to calculate the viscosity and thermal conductivity of the equilibrium state. The equilibrium thermal conductivity λ_{eq} is expressed as the sum of two values "frozen" and "reaction" written as

$$\lambda_{eq}=\lambda_{fr}+\lambda_{re} \tag{2.59}$$

where λ_{eq}, λ_{fr} and λ_{re} are the equilibrium, frozen, and reaction thermal conductivities, respectively.

In CEA, the following equation is used to obtain the viscosity of equilibrium mixture η_{mix} and frozen thermal conductivity λ_{fr}.

$$\eta_{mix}=\sum_{i=1}^{NM}\frac{x_i\eta_i}{x_i+\sum_{\substack{j=1\\ j\neq i}}^{NM}x_j\phi_{ij}} \tag{2.60}$$

$$\lambda_{fr}=\sum_{i=1}^{NM}\frac{x_i\lambda_i}{x_i+\sum_{\substack{j=1\\ j\neq i}}^{NM}x_j\psi_{ij}} \tag{2.61}$$

NM denotes the number of gaseous species contained in a mixture for which equilibrium thermal conductivity and viscosity are to be determined, and x_i denotes the mole fraction of the species i. η_i and λ_i denote the viscosity and thermal conductivity of the species i, respectively, and are the values obtained by equation (2.58). ϕ_{ij} and ψ_{ij} are the viscosity interaction

coefficient and the interaction coefficient for the species i and j, and the equations for each is as follows.

$$\phi_{ij} = \frac{1}{4}\left[1+\left(\frac{\eta_i}{\eta_j}\right)^{1/2}\left(\frac{M_j}{M_i}\right)^{1/4}\right]^2\left(\frac{2M_j}{M_i+M_j}\right)^{1/2} \tag{2.62}$$

$$\psi_{ij} = \phi_{ij}\left[1+\frac{2.41\left(M_i-M_j\right)\left(M_i-0.142M_j\right)}{\left(M_i+M_j\right)^2}\right] \tag{2.63}$$

To obtain the reaction thermal conductivity λ_{re}, the following equation is used.

$$\lambda_{re} = R\sum_{i=1}^{NR}\frac{\triangle_r H_i^{\circ}}{RT}\lambda_{r,i} \tag{2.64}$$

NR denotes the total number of chemical reactions a mixture can react with. $\triangle_r H_i^{\circ}$ is the heat of reaction for reaction i expressed as equation (2.65). α_{ik} is the stoichiometric coefficients of the species A_k in the reaction i.

$$\triangle_r H_i^{\circ}(T) = \sum_{k=1}^{NM}\alpha_{ik}H_k^{\circ} \tag{2.65}$$

$$\sum_{k=1}^{NM}\alpha_{ik}A_k = 0 \tag{2.66}$$

Also, $\lambda_{r,i}$ used to calculate λ_{re} can be obtained by solving the following linear system equations. The variable A_{kl}^{*} is the collision cross-section ratio, and 1.1 is assigned for CEA.

$$\sum_{j=1}^{NR} g_{ij}\lambda_{r,j} = \frac{\triangle_r H_i^\circ(T)}{RT} \tag{2.67}$$

$$g_{ij} = \sum_{k=1}^{NM-1}\sum_{l=k+1}^{NM}\left(\frac{RT}{PD_{kl}}x_k x_l\right)\left(\frac{\alpha_{ik}}{x_k}-\frac{\alpha_{il}}{x_l}\right)\left(\frac{\alpha_{jk}}{x_k}-\frac{\alpha_{jl}}{x_l}\right) \tag{2.68}$$

$$\frac{RT}{PD_{kl}} = \frac{5M_kM_l}{3A_{kl}^*\eta_{kl}(M_k+M_l)} \tag{2.69}$$

2.5.4. Equivalent gamma using CEA database

To obtain the flux Jacobian matrix used in the LU-SGS method, we need to differentiate the pressure as conservative variables. The precise differentiation process is quite complicated for chemical reacting flow[6]. To use the CEA database for obtaining flux Jacobian matrix of equilibrium flow, the concept of "equivalent gamma" used by Shuen and Yoon[7] is applied.

$$\bar{\gamma} = h_{s_m}/e_{s_m} = \left(\sum_{i=1}^{N_s} Y_i\int_0^T C_{p,i}dT\right)\Big/\left(\sum_{i=1}^{N_s} Y_i\int_0^T C_{v,i}dT\right) \tag{2.70}$$

In the above equation, $\bar{\gamma}$ denotes equivalent γ. N_s is the number of species of reacting flow, and Y_i denotes mass fraction of species i. $C_{p,i}$ and $C_{v,i}$ is specific heat at constant pressure and at constant temperature of species i respectively. h_{s_m} and e_{s_m} denotes sensible enthalpy and sensible internal energy excluding the heat of formation for the mixture, respectively as

$$h_{s_m} = h - h_{f_m}^\circ,\ e_{s_m} = e - h_{f_m}^\circ \tag{2.71}$$

$$h_{f_m}^\circ = \sum_{i=1}^{N_s} Y_i h_{f_i}^\circ \tag{2.72}$$

where $h_{f_m}^\circ$ and $h_{f_i}^\circ$ denote the heat of formation of the mixture and species

i, respectively.

To obtain $\bar{\gamma}$ using the CEA database, we should not use the specific heat formular like the right term of equation (2.70), but directly use the formular of sensible enthalpy and energy like the middle term. First, as mentioned in section 2.5.3., we can obtain the equilibrium mole fraction, energy, and enthalpy using the CEA program. Since energy and enthalpy obtained by the CEA program are absolute energy and enthalpy, it is necessary to subtract the heats of formation from the obtained values to extract the sensible values.

Since "$\triangle H_f$(298.15 K)" and "H(298.15 K)-H(0 K)" values of each species for the mixture can be found in 'thermo.inp' file, The zero-point energy, which is the enthalpy when the temperature of each species is 0 K, can be obtained from $H(0\ \mathrm{K}) = \triangle H_f(298.15\ \mathrm{K}) - H(298.15\ \mathrm{K})\text{-}H(0\ \mathrm{K})$. Anderson[1] stated the theorem : "In a chemical reaction, the change in zero-point energy is equal to the difference between the heats of formation of the products at T=0 K and the heats of formations of the reactants at T=0 K." Therefore, H(0 K) values of each species can be used as the heats of formation and finally $\bar{\gamma}$ can be obtained.

The expression for pressure using $\bar{\gamma}$ can be written as equation (2.73), and flux jacobian matrix can be obtained as followings.

$$\begin{aligned} p &= (\bar{\gamma}-1)\rho e_{s_m} \\ &= (\bar{\gamma}-1)\left[\rho e_t - \rho h^{\circ}_{f_m} - 0.5\rho(u^2+v^2)\right] \end{aligned} \tag{2.73}$$

Flux Jacobian matrix

$$\frac{\partial \bar{E}}{\partial Q} = A y_\eta - B x_\eta, \quad \frac{\partial \bar{F}}{\partial Q} = -A y_\xi + B x_\xi \tag{2.74}$$

$$A = \left(= \frac{\partial E}{\partial Q}\right) = \begin{bmatrix} 0 & 1 & 0 & 0 \\ -u^2 + (\bar{\gamma}-1)\left[-h^{\circ}_{f_m} + 0.5(u^2+v^2)\right] & (3-\bar{\gamma})u & -(\bar{\gamma}-1)v & \bar{\gamma}-1 \\ -uv & v & u & 0 \\ -uH + u(\bar{\gamma}-1)\left[-h^{\circ}_{f_m} + 0.5(u^2+v^2)\right] & H-(\bar{\gamma}-1)u^2 & -(\bar{\gamma}-1)uv & \bar{\gamma}u \end{bmatrix}$$

$$B = \left(= \frac{\partial F}{\partial Q}\right) = \begin{bmatrix} 0 & 1 & 0 & 0 \\ -uv & v & u & 0 \\ -v^2 + (\bar{\gamma}-1)\left[-h^{\circ}_{f_m} + 0.5(u^2+v^2)\right] & -(\bar{\gamma}-1)u & (3-\bar{\gamma})v & \bar{\gamma}-1 \\ -vH + v(\bar{\gamma}-1)\left[-h^{\circ}_{f_m} + 0.5(u^2+v^2)\right] & -(\bar{\gamma}-1)uv & H-(\bar{\gamma}-1)v^2 & \bar{\gamma}v \end{bmatrix}$$

2.5.5. Utilization of CEA database

As shown in the previous section, it was confirmed that the equilibrium chemical composition and thermodynamic properties can be obtained by using CEA under the desired conditions. However, if CEA's free energy minimization method is implemented on the CFD code and it is executed all cells for every iteration to solve the flow governing equations, it takes long calculation time that it is impossible to analyze the flow. Therefore, in order to shorten the computation time, some tables are prepared in advance by using the CEA GUI program, and a method of interpolating the necessary values using the tables is adopted. In the process of solving the governing equations, since two methods are needed to obtain equilibrium chemical composition and thermodynamic properties, (T,p) and (ρ,e) tables according to each utilization method are prepared.

An example of the (T,p) table prepared for the equilibrium flow calculation at the beginning of the study is shown in Figure 2.3. Table 16 shows the chemical composition of the nozzle combustion gases in the combustion chamber condition delivered from the ADD.

▸ **(ρ,e) Table**

Density(ρ) and internal energy(e) calculated in the flow governing equation are used as inputs.

(ρ,e) → T, p, transport coefficients, mole fraction and other properties

▸ **(T,p) Table**

Temperature(T) and pressure(p) given in wall boundary conditions are used as inputs.

(T,p) → ρ, e, transport coefficients, mole fraction and other properties

Table 2.1 Nozzle combustion gas mole fraction at 2750 K, 2500 psi

No.	Species	Mole fraction	No.	Specie	Mole fraction
1	CH_4	0.00000	9	H_2	0.18317
2	CO	0.30780	10	H_2O	0.17568
3	CO_2	0.04793	11	NH_3	0.00002
4	Cl	0.00015	12	NO	0.00002
5	H	0.00166	13	N_2	0.25983
6	HCN	0.00000	14	O	0.00000
7	HCO	0.00000	15	OH	0.00033
8	HCl	0.02341	16	O_2	0.00000

T[K]	P[bar]	rho[kg/m^3]	E[kJ/kg]	H[kJ/kg]	MW[kg/(kg-mol)]	Cp[kJ/(kg*K)]	gamma	sonic_vel[m/s]	viscosity[millipoise]	conductivity[mW/(cm*K)]	Pr
238											
200.00	109.0000000000	195.040000000	-5987.40	-5931.60	29.75600	1.05770	1.35900	275.59000	0.11119	0.16781	0.70084
220.00	109.0000000000	177.310000000	-5971.80	-5910.30	29.75600	1.06930	1.35370	288.48000	0.12113	0.18011	0.71916
240.00	109.0000000000	162.540000000	-5955.80	-5888.80	29.75600	1.08160	1.34830	300.70000	0.13099	0.19399	0.73036
260.00	109.0000000000	150.030000000	-5939.70	-5867.00	29.75600	1.09460	1.34280	312.33000	0.14075	0.20899	0.73720
280.00	109.0000000000	139.320000000	-5923.20	-5845.00	29.75600	1.10820	1.33720	323.45000	0.15038	0.22479	0.74131
300.00	109.0000000000	130.030000000	-5906.50	-5822.70	29.75600	1.12220	1.33150	334.09000	0.15987	0.24124	0.74368
320.00	109.0000000000	121.900000000	-5889.50	-5800.10	29.75600	1.13660	1.32600	344.33000	0.16921	0.25820	0.74490
340.00	109.0000000000	114.730000000	-5872.20	-5777.20	29.75600	1.15140	1.32040	354.18000	0.17841	0.27562	0.74533
360.00	109.0000000000	108.360000000	-5854.60	-5754.00	29.75600	1.16650	1.31500	363.70000	0.18745	0.29346	0.74516
380.00	109.0000000000	102.660000000	-5836.70	-5730.60	29.75600	1.18200	1.30960	372.90000	0.19635	0.31173	0.74447
400.00	109.0000000000	97.522000000	-5818.50	-5706.80	29.75600	1.19770	1.30440	381.82000	0.20510	0.33048	0.74327
420.00	109.0000000000	92.878000000	-5800.00	-5682.70	29.75600	1.21370	1.29920	390.48000	0.21371	0.34981	0.74150
440.00	109.0000000000	88.655000000	-5781.20	-5658.20	29.75500	1.23020	1.29420	398.89000	0.22218	0.36983	0.73906
460.00	109.0000000000	84.798000000	-5762.00	-5633.40	29.75500	1.24720	1.28920	407.08000	0.23051	0.39074	0.73581
480.00	109.0000000000	81.262000000	-5742.50	-5608.30	29.75400	1.26500	1.28430	415.04000	0.23872	0.41275	0.73162
500.00	109.0000000000	78.007000000	-5722.60	-5582.80	29.75200	1.28350	1.27940	422.81000	0.24681	0.43614	0.72634
520.00	109.0000000000	75.001000000	-5702.30	-5557.00	29.74900	1.30330	1.27450	430.38000	0.25477	0.46126	0.71985
540.00	109.0000000000	72.215000000	-5681.60	-5530.70	29.74600	1.32450	1.26960	437.77000	0.26262	0.48847	0.71209
560.00	109.0000000000	69.624000000	-5660.50	-5504.00	29.74100	1.34760	1.26470	444.97000	0.27036	0.51824	0.70302
580.00	109.0000000000	67.209000000	-5639.00	-5476.80	29.73500	1.37310	1.25970	452.00000	0.27799	0.55107	0.69268
600.00	109.0000000000	64.951000000	-5616.90	-5449.00	29.72700	1.40170	1.25460	458.85000	0.28553	0.58754	0.68120
620.00	109.0000000000	62.832000000	-5594.20	-5420.70	29.71500	1.43430	1.24920	465.52000	0.29296	0.62831	0.66877

CH4	CO	CO2	CL	H	HCN	HCO	HCL	H2	H2O	NH3	NO	N2	O	OH	O2
0.16317E+00	0.64104E-18	0.30915E+00	0.00000E+00	0.00000E+00	0.62664E-36	0.00000E+00	0.31282E-01	0.11351E-09	0.15138E+00	0.40338E-06	0.00000E+00	0.34502E+00	0.00000E+00	0.00000E+00	0.00000E+00
0.16317E+00	0.54780E-16	0.30915E+00	0.00000E+00	0.00000E+00	0.17393E-32	0.00000E+00	0.31282E-01	0.10190E-08	0.15138E+00	0.98129E-06	0.00000E+00	0.34501E+00	0.00000E+00	0.00000E+00	0.00000E+00
0.16317E+00	0.22559E-14	0.30915E+00	0.00000E+00	0.00000E+00	0.12989E-29	0.00000E+00	0.31282E-01	0.64097E-08	0.15138E+00	0.20477E-05	0.00000E+00	0.34501E+00	0.00000E+00	0.00000E+00	0.00000E+00
0.16317E+00	0.52901E-13	0.30915E+00	0.00000E+00	0.00000E+00	0.35320E-27	0.00000E+00	0.31282E-01	0.30655E-07	0.15138E+00	0.38005E-05	0.00000E+00	0.34501E+00	0.00000E+00	0.00000E+00	0.00000E+00
0.16317E+00	0.79610E-12	0.30915E+00	0.00000E+00	0.00000E+00	0.49407E-25	0.00000E+00	0.31282E-01	0.11817E-06	0.15138E+00	0.64577E-05	0.00000E+00	0.34501E+00	0.00000E+00	0.00000E+00	0.00000E+00
0.16317E+00	0.83935E-11	0.30915E+00	0.59117E-34	0.00000E+00	0.28251E-23	0.00000E+00	0.31282E-01	0.38319E-06	0.15138E+00	0.10141E-04	0.00000E+00	0.34501E+00	0.00000E+00	0.00000E+00	0.00000E+00
0.16316E+00	0.66226E-10	0.30916E+00	0.74516E-32	0.00000E+00	0.10966E-21	0.00000E+00	0.31282E-01	0.10794E-05	0.15137E+00	0.15066E-04	0.00000E+00	0.34501E+00	0.00000E+00	0.00000E+00	0.00000E+00
0.16316E+00	0.41131E-09	0.30916E+00	0.53196E-30	0.19443E-34	0.27804E-20	0.00000E+00	0.31282E-01	0.27064E-05	0.15137E+00	0.21334E-04	0.00000E+00	0.34501E+00	0.00000E+00	0.00000E+00	0.00000E+00
0.16316E+00	0.20916E-08	0.30916E+00	0.23847E-28	0.21411E-32	0.49418E-19	0.32905E-34	0.31282E-01	0.61575E-05	0.15136E+00	0.29036E-04	0.00000E+00	0.34501E+00	0.00000E+00	0.00000E+00	0.00000E+00
0.16315E+00	0.89840E-08	0.30917E+00	0.70538E-27	0.14437E-30	0.65106E-18	0.29795E-32	0.31282E-01	0.12904E-04	0.15135E+00	0.38226E-04	0.00000E+00	0.34500E+00	0.00000E+00	0.25317E-34	0.00000E+00
0.16315E+00	0.33420E-07	0.30917E+00	0.14991E-25	0.64138E-29	0.66486E-17	0.17217E-30	0.31281E-01	0.25212E-04	0.15133E+00	0.48931E-04	0.00000E+00	0.34499E+00	0.00000E+00	0.15231E-32	0.00000E+00
0.16313E+00	0.10987E-06	0.30918E+00	0.23826E-24	0.19924E-27	0.54565E-16	0.67685E-29	0.31281E-01	0.46377E-04	0.15131E+00	0.61150E-04	0.00000E+00	0.34498E+00	0.00000E+00	0.62090E-31	0.00000E+00
0.16312E+00	0.32456E-06	0.30919E+00	0.29463E-23	0.45430E-26	0.37070E-15	0.19074E-27	0.31281E-01	0.80960E-04	0.15128E+00	0.74861E-04	0.00000E+00	0.34497E+00	0.00000E+00	0.18086E-29	0.00000E+00
0.16310E+00	0.87347E-06	0.30920E+00	0.29293E-22	0.79152E-25	0.21365E-14	0.40240E-26	0.31280E-01	0.13502E-03	0.15124E+00	0.90024E-04	0.00000E+00	0.34496E+00	0.00000E+00	0.39324E-28	0.00000E+00
0.16306E+00	0.21663E-05	0.30922E+00	0.24063E-21	0.10896E-23	0.10661E-13	0.65887E-25	0.31279E-01	0.21631E-03	0.15118E+00	0.10658E-03	0.00000E+00	0.34493E+00	0.00000E+00	0.66196E-27	0.00000E+00
0.16302E+00	0.49993E-05	0.30923E+00	0.16711E-20	0.12189E-22	0.46856E-13	0.86305E-24	0.31277E-01	0.33444E-03	0.15110E+00	0.12446E-03	0.00000E+00	0.34491E+00	0.00000E+00	0.88983E-26	0.00000E+00
0.16295E+00	0.10824E-04	0.30925E+00	0.11348E-19	0.11348E-21	0.18404E-12	0.92791E-23	0.31275E-01	0.50101E-03	0.15100E+00	0.14359E-03	0.00000E+00	0.34487E+00	0.00000E+00	0.97926E-25	0.00000E+00
0.16287E+00	0.22141E-04	0.30927E+00	0.52466E-19	0.89730E-21	0.65403E-12	0.83688E-22	0.31271E-01	0.72962E-03	0.15086E+00	0.16387E-03	0.00000E+00	0.34482E+00	0.00000E+00	0.90287E-24	0.00000E+00
0.16275E+00	0.43046E-04	0.30929E+00	0.24660E-18	0.61312E-20	0.21255E-11	0.64535E-21	0.31266E-01	0.10359E-02	0.15067E+00	0.18520E-03	0.00000E+00	0.34478E+00	0.00000E+00	0.71058E-23	0.00000E+00
0.16260E+00	0.79960E-04	0.30931E+00	0.10259E-17	0.36750E-19	0.63747E-11	0.49229E-20	0.31260E-01	0.14375E-02	0.15044E+00	0.20748E-03	0.00000E+00	0.34467E+00	0.00000E+00	0.48506E-22	0.00000E+00
0.16240E+00	0.14255E-03	0.30931E+00	0.39128E-17	0.19576E-18	0.17784E-10	0.25511E-19	0.31251E-01	0.19537E-02	0.15015E+00	0.23058E-03	0.00000E+00	0.34456E+00	0.00000E+00	0.29137E-21	0.00000E+00
0.16214E+00	0.24484E-03	0.30929E+00	0.13694E-16	0.93727E-18	0.46472E-10	0.13426E-18	0.31239E-01	0.26057E-02	0.14981E+00	0.25440E-03	0.00000E+00	0.34442E+00	0.00000E+00	0.15591E-20	0.00000E+00

Figure 2.3 (T,p) **Table example**

Since the tables created using the CEA GUI program are the equilibrium thermodynamic properties of a particular input condition, it is needed to create a function to calculate the thermodynamic properties for any arbitrary inputs. A bilinear interpolation function is used to obtain the desired value.

$$f(x,y) \approx \frac{y_2-y}{y_2-y_1}\left(\frac{x_2-x}{x_2-x_1}f(Q_{11})+\frac{x-x_1}{x_2-x_1}f(Q_{21})\right) + \frac{y-y_1}{y_2-y_1}\left(\frac{x_2-x}{x_2-x_1}f(Q_{12})+\frac{x-x_1}{x_2-x_1}f(Q_{22})\right) \tag{2.75}$$

In Figure 2.4, the value of the position of the green dot is the desired value, and the four red dots indicate the position of the table data needed to interpolate it.

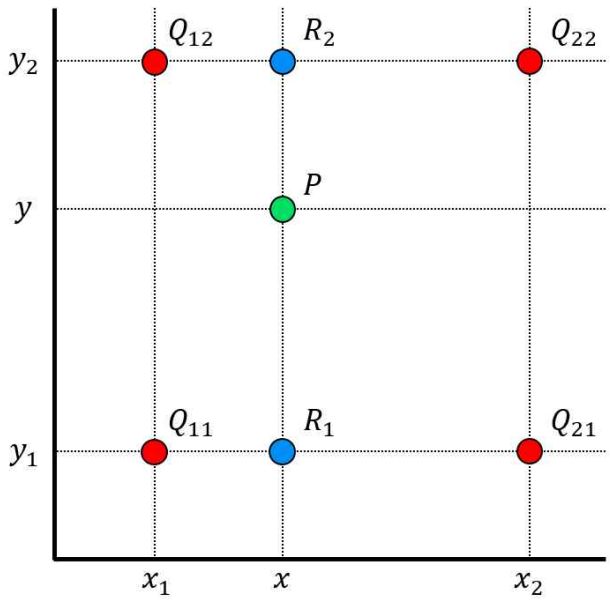

Figure 2.4 Schematic of bilinear interpolation

2.5.6. CEA output verification

2.5.6.1. Monotonic function

To use the bilinear interpolation function with the desired accuracy, it is necessary to check whether the maximum value or the minimum value exists in the inner area of the four table data $D=[x_1,x_2]\times[y_1,y_2]$ for the bilinear interpolation. If the maximum or minimum value does not exist at the boundaries of the domain D but exists in the inner region, the interpolated value may show a large difference from the actual value because the bilinear interpolation function uses the linear interpolation twice. To confirm this, the pressure distribution using the (ρ,e) table and the density distribution using the (T,p) table are shown in Figures 2.5 and 2.6. The pressure and temperature distributions were found to be monotonically increasing or monotonically decreasing for both the x and y axes. Therefore, the maximum and minimum values in the interpolating table data region always exist at the boundaries of the domain D, then it is confirmed that the bilinear interpolation method using the table can obtain the desired level of accuracy.

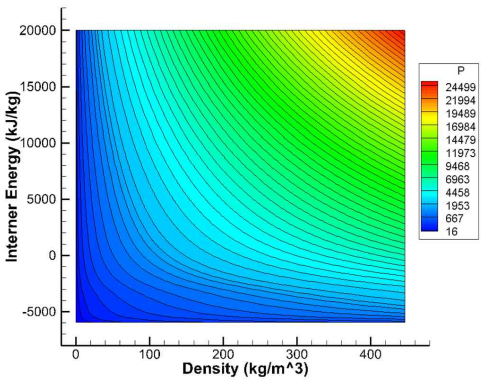

Figure 2.5 Pressure distribution with (ρ,e) Table

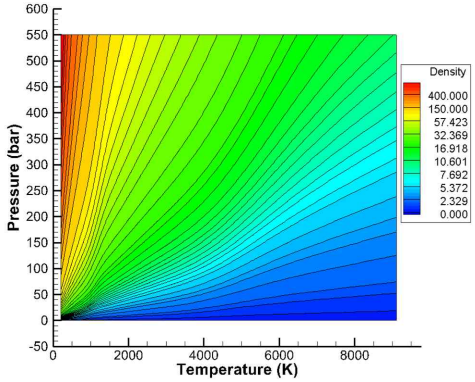

Figure 2.6 Density distribution with (T,p) Table

2.5.6.2. Comparison of CEA GUI program output values and literature values

Since CEA is a NASA-provided program that has a high level of reliability, a simple verification is performed to see if it matches other literature values. Figure 2.7 shows the mole fraction of the air 5 chemical species (N2, NO, N, O2, O) at 1 atmospheric pressure as a function of temperature and the literature values and the CEA program output values were compared. It was confirmed that the compared values were in good agreement.

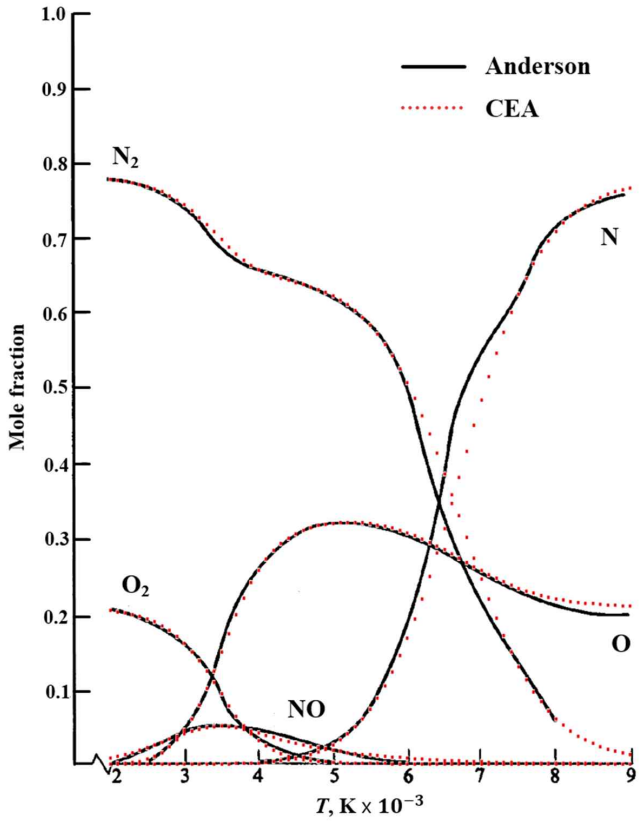

Figure 2.7 Composition of equilibrium air versus temperature at 1 atm. (5 species)

2.5.6.3. Comparison of CEA GUI program output values and output values of bilinear interpolation function using table

It has been confirmed earlier that the CEA output is reliable and have now verified that the bilinear interpolation function works correctly. The mole fractions of the sixteen species of nozzle combustion gases at 1000 psi and 2000 psi as a function of temperature are shown in Figure 2.8 and 2.9, respectively. The black solid line represents the CEA output values, and the red dot represents the output values of the bilinear interpolation function using the (T,p) table. The graph shows only five chemical species with large mole fractions, and the bilinear interpolation function using table shows reliable accuracy.

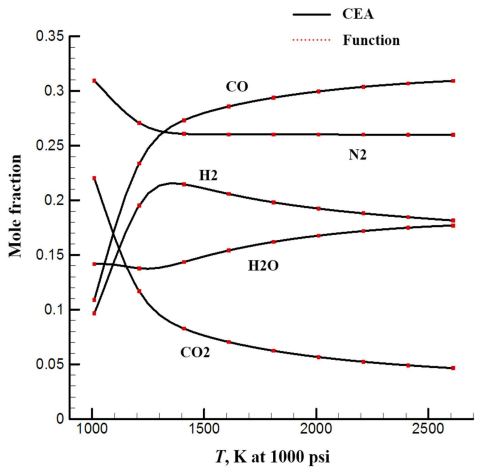

Figure 2.8 Composition of equilibrium nozzle combustion gas versus temperature at 1000 psi. (16 species)

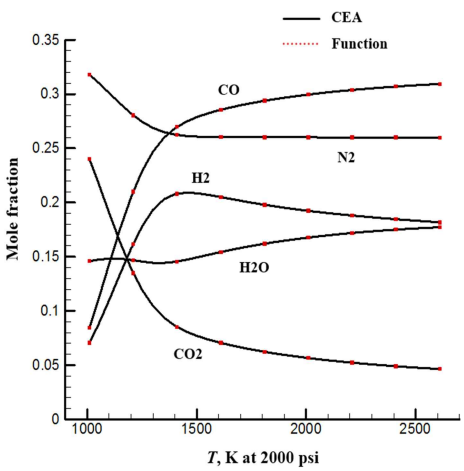

Figure 2.9 Composition of equilibrium nozzle combustion gas versus temperature at 2000 psi. (16 species)

2.5.7. Precise verification of output values of bilinear interpolation function using table and table significant digits improvement

In order to verify the accuracy of the flow analysis code during the re-study, a detailed check of the bilinear interpolation function using the table was performed. Using the bilinear interpolation function, more than 10 values were printed between one data interval of the table. stepwise graphs which were not shown when a single output was printed for each data interval are found.(Figure 2.10-12)

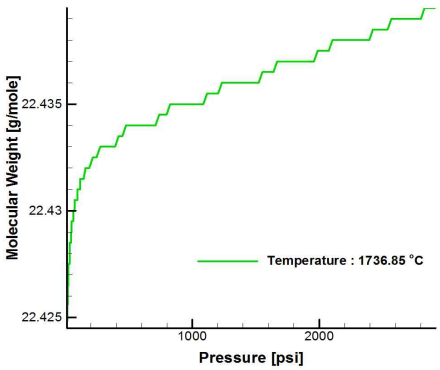

Figure 2.10 Stepwise result of molecular weight vs. pressure

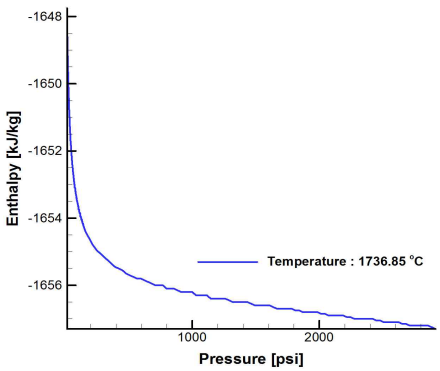

Figure 2.11 Stepwise result of enthalpy vs. pressure

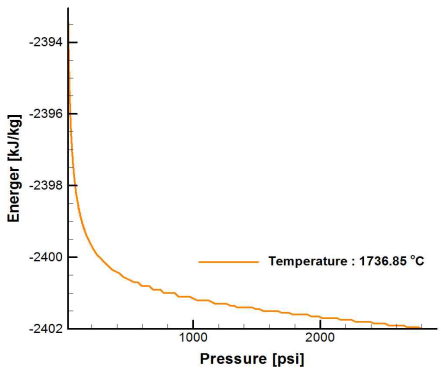

Figure 2.12 Stepwise result of internal energy vs. pressure

The significant digits of output printed from the CEA GUI program is five as shown in Figure 2.2. If you look at the graph output results, all the values of the stepped form occur within the 5th significant digit. Looking at the stepwise graph, all of the cascading output values occur within the 5^{th} significant digit. Therefore, it is expected that the calculation accuracy is insufficient for the 5 significant digits of the CEA GUI program output.

To obtain more accurate equilibrium flow calculation results, I adopted the way of directly handling the CEA source code to write a table to have more significant digits. I handled Fortran 77-based CEA source code provided when downloading CEA GUI program from NASA CEA homepage, and modified the source code to get the desired data. I increased the number of significant digits of the output to 14 levels and improved the (T,p) and (ρ,e) table. In order to confirm the improvement effect, the difference of the output values due to the difference of the significant digits of the table is shown as in Figure 2.13-25. Graphs show that the interpolation function output is smoothed and improved.

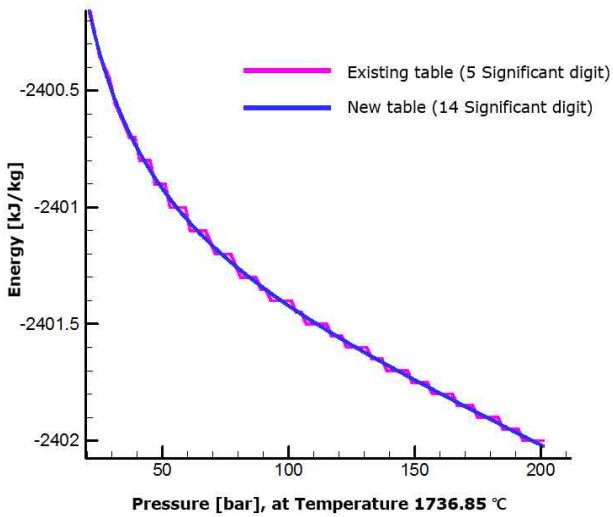

Figure 2.13 Improved CEA table function energy output

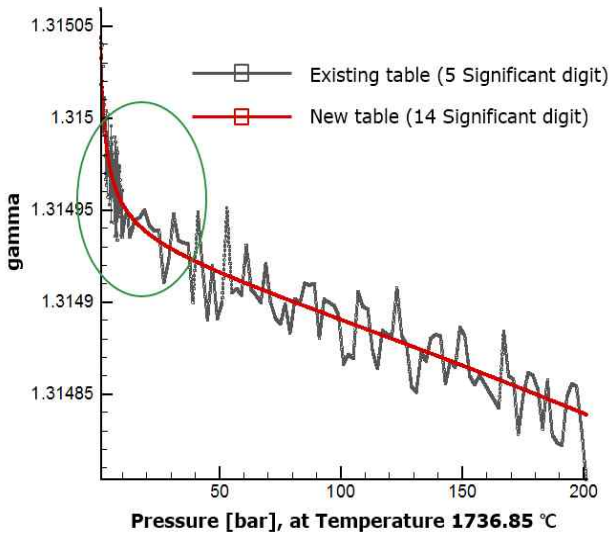

Figure 2.14 Improved CEA table function gamma output

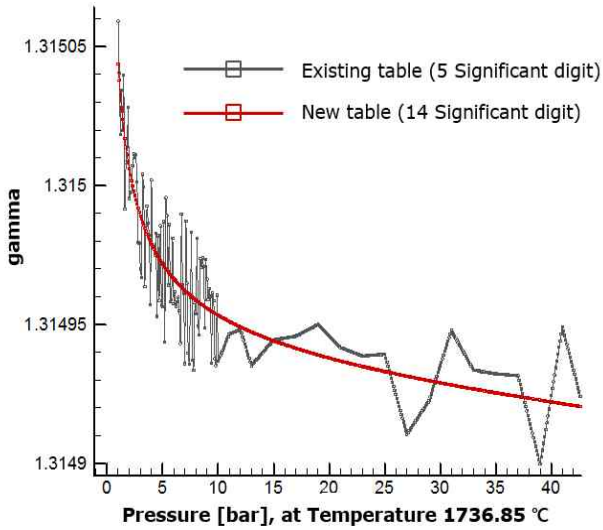

Figure 2.15 Improved CEA table function gamma output(zoomed in)

There was considerable improvement in the time it takes to create tables because it is calculated using the CEA source code directly. It takes about 50 hours to create a table of 160,000 data using the CEA GUI program, but it takes only 15 minutes to create an improved table of 2,120,000 data using the modified CEA source code. The modified CEA source code was included in the CFD code and automatically creates the table at the beginning of the code operation. The table data is arranged more tightly to improve the accuracy of the bilinear interpolation function using (T,p) and (ρ,e) tables. The improved results are shown in Tables 2.2 and 2.3, and the output accuracy of the interpolation function is greatly improved. An example of the before and after improvement of (ρ,e) table is shown in Figure 2.16.

Table 2.2 Verification of interpolation function improvement using (T,p) table

(T,p) table	input		output		Data point
	T [K]	p [bar]	ρ [kg/m^3]	e [kJ/kg]	[T1,T2]×[p1,p2]
Exact	1412.43	113.42	21.81202825	-3277.3929216	
Existing table	1412.43	113.42	21.81436293	-3277.6574756	[1400,1420] ×[113,115]
New table	1412.43	113.42	21.81204543	-3277.3948077	[1412,1414] ×[113,113.5]

Table 2.3 Verification of interpolation function improvement using (ρ,e) table

(ρ,e) table	input		output		Data point
	ρ [kg/m^3]	e [kJ/kg]	T [K]	p [bar]	[ρ1,ρ2]×[e1,e2]
Exact	8.213	-2113.38	2208.0478886	67.21848295	
Existing table	8.213	-2113.38	2208.04051974	67.21841602	[8.0909590,8.3176377] ×[-2120,-2100]
New table	8.213	-2113.38	2208.0478139	67.21848132	[8.1283052,8.2224265] ×[-2115,-2112]

Figure 2.16 Existing(left) and improved(right) (ρ,e) table example

2.5.8. Generalization of Equilibrium Flow Codes

The developed equilibrium code can calculate the equilibrium flow composed of the user-desired chemical species by simply modifying the five input files shown in Figure 2.17. In the 'thermoinput.dat' file, the chemical species and initial mole fraction of the reacting flow can be written as user wants. Then by modifying ‘T.dat’, ‘P.dat’, ‘rho.dat’, ‘E.dat’ files, user can set as many table intervals as he/she wants.

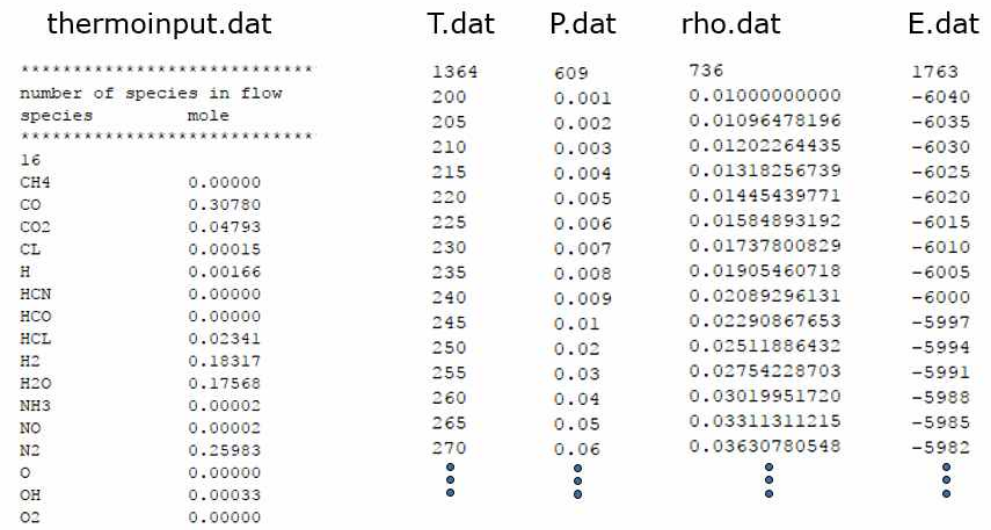

Figure 2.17 Input files required to create table

3

FLOW/STRUCTURE INTEGRATED ANALYSIS CODE DEVELOPMENT

3.1. Flow/structure integrated analysis code outline

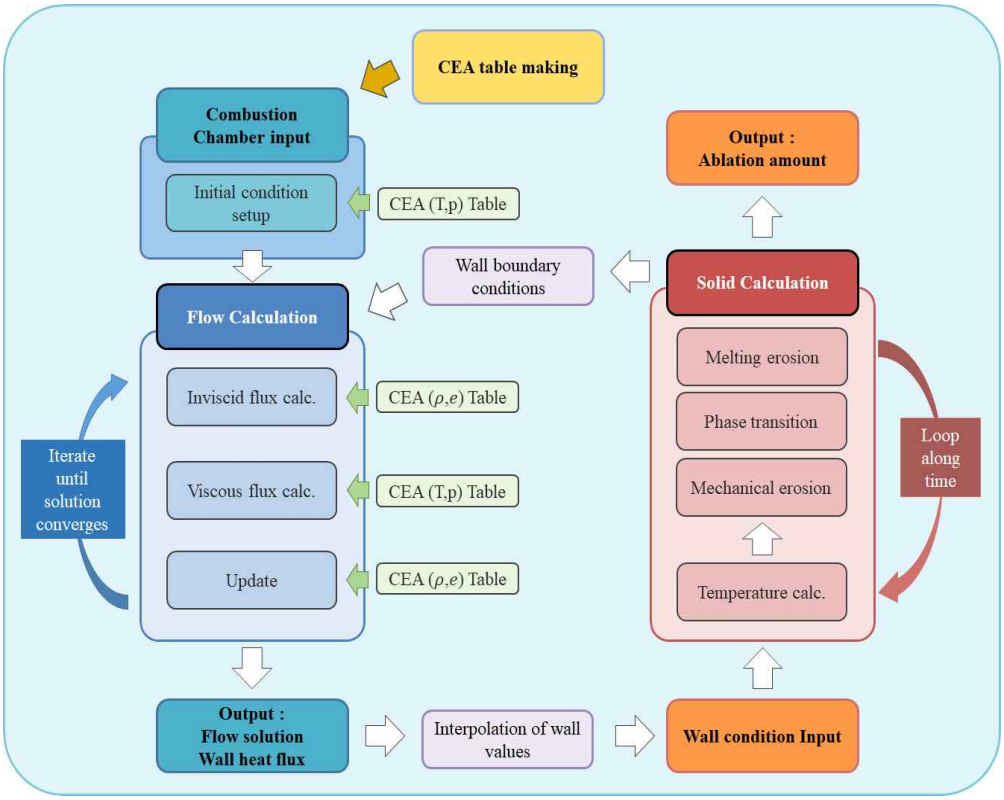

Figure 3.1 Integrated code outline

The equilibrium flow analysis code and the structural analysis code are integrated to analyze the amount of SiC coated nozzle erosion. The outline of integrated code is shown in Figure 3.1. The code was constructed by analyzing the flow and nozzle structure independently, and the code is coupled by exchanging the boundary conditions between the flow and the structure.

When the code starts, (T,p) and (ρ,e) tables are created by modified CEA source code. After then, the flow calculations begins and the equilibrium two-dimensional axisymmetric Navier-Stokes equations is solved until the flow values converge. After calculating the heat transfer and shear stress to the nozzle wall surface by using the converged flow solution, these values are transferred to the boundary condition of the structure analysis code. The structure analysis code calculates the temperature distribution of the nozzle wall surface and inside the structure, and calculates the amount of erosions. The wall temperature distribution is then transferred back to the flow code to calculate the flow field. Through this iterative process, nozzle wall temperature, heat transfer, shear force and erosion can be calculated over time.

3.2. Algorithm of flow and structure analysis code coupling

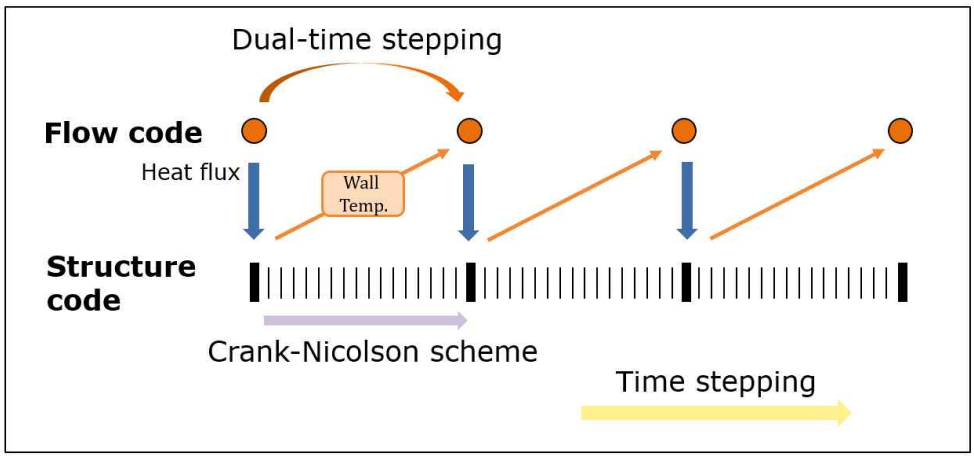

Figure 3.2 Flow/structural analysis code connection diagram

Since the flow analysis code takes a long time to converge compared to the structure analysis code, the dual time step is applied. When the flow analysis is performed, calculation is performed at a wide time interval, and The structure analysis, which is relatively fast in computation, performs in tight time intervals to increase accuracy. In order to analyze the temperature distribution of the structure, boundary conditions of nozzle wall temperature distribution over time are needed. The n-th and (n-1)th heat flux are linearly interpolated according to the time of structure code.

3.3. Structural analysis governing equation

For the analysis of temperature distribution of nozzle structure, two-dimensional axisymmetric heat transfer equations are used.

2D axisymmetric heat transfer equation

$$\frac{\partial \rho e}{\partial t}+\frac{\partial q_x}{\partial x}+\frac{\partial q_y}{\partial y}+\frac{q_y}{y}=0 \tag{3.1}$$

In the above equation, the energy and the directional heat conduction are rewritten as

$$\frac{\partial T}{\partial t}=\alpha\frac{\partial^2 T}{\partial x^2}+\alpha\frac{\partial^2 T}{\partial y^2}+\frac{\alpha}{y}\frac{\partial T}{\partial y} \tag{3.2}$$

q_i : i-dir. conduction$\left(=-k\frac{\partial T}{\partial x_i}\right)$ ρ : density

x : axial direction e : energy$(=C_pT)$

y : radial direction C_p : specific heat

k : thermal conductivity α : heat transfer coefficient$(=k/\rho C_p)$

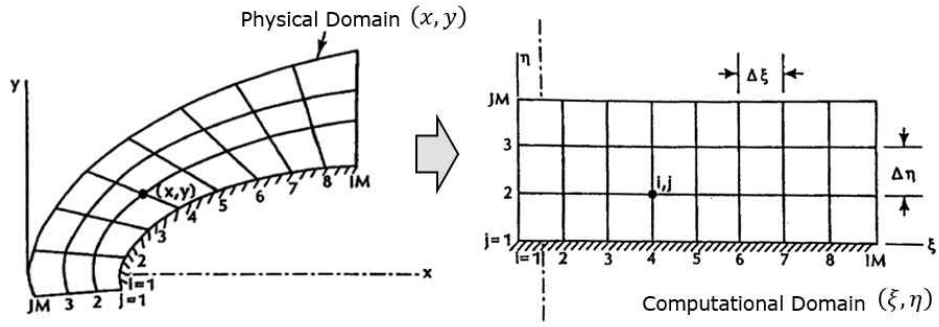

Figure 3.3 Coordinate transformation using metric, $(x,y)\rightarrow(\xi,\eta)$

The heat transfer equation expressed with computational domain is as follows.

$$\begin{aligned}\frac{\partial T}{\partial t}=&\alpha\left(\xi_x^2\frac{\partial^2 T}{\partial\xi^2}+2\xi_x\eta_x\frac{\partial^2 T}{\partial\xi\partial\eta}+\eta_x^2\frac{\partial^2 T}{\partial\eta^2}\right)\\&+\alpha\left(\xi_y^2\frac{\partial^2 T}{\partial\xi^2}+2\xi_y\eta_y\frac{\partial^2 T}{\partial\xi\partial\eta}+\eta_y^2\frac{\partial^2 T}{\partial\eta^2}\right)\\&+\alpha\left(\xi_y\frac{\partial T}{\partial\xi}+\eta_y\frac{\partial T}{\partial\eta}\right)\end{aligned}\tag{3.3}$$

$$\begin{aligned}\frac{\partial T}{\partial t}=&\alpha\left[\left(\xi_x^2+\xi_y^2\right)\frac{\partial^2 T}{\partial\xi^2}+2\left(\xi_x\eta_x+\xi_y\eta_y\right)\frac{\partial^2 T}{\partial\xi\partial\eta}+\left(\eta_x^2+\eta_y^2\right)\frac{\partial^2 T}{\partial\eta^2}\right]\\&+\alpha\left(\xi_y\frac{\partial T}{\partial\xi}+\eta_y\frac{\partial T}{\partial\eta}\right)\end{aligned}\tag{3.4}$$

For the numerical analysis, partial differential equations are presented in a discrete form, and FDM(Finite Difference Method) using Crank-Nicolson scheme is applied. Since the C-N scheme is an implicit method ensuring the computational robustness and second-order accuracy for space and time, it is frequently used. The second derivatives of ξ and η are implicitly treated, and cross derivative term and axisymmetric term are explicitly treated for computational efficiency.

$$\frac{T^{n+1}-T^n}{\triangle t}=\frac{\alpha}{2}\left(\xi_x^2+\xi_y^2\right)\left(A_\xi T^{n+1}+A_\xi T^n\right) \tag{3.5}$$
$$+\frac{\alpha}{2}\left(\eta_x^2+\eta_y^2\right)\left(A_\eta T^{n+1}+A_\eta T^n\right)$$
$$+2\alpha\left(\xi_x\eta_x+\xi_y\eta_y\right)B_\xi B_\eta T^n+\frac{\alpha}{y}\left(\xi_y B_\xi T^n+\eta_y B_\eta T^n\right)$$

$$A_\xi T^n=\frac{T^n_{i+1,j}-2T^n_{i,j}+T^n_{i-1,j}}{\triangle\xi^2},\quad A_\eta T^n=\frac{T^n_{i,j+1}-2T^n_{i,j}+T^n_{i,j-1}}{\triangle\eta^2} \tag{3.6}$$

$$B_\xi T^n=\frac{T^n_{i+1,j}-T^n_{i-1,j}}{2\triangle\xi},\quad B_\eta T^n=\frac{T^n_{i,j+1}-T^n_{i,j-1}}{2\triangle\eta} \tag{3.7}$$

Equation (3.5) is rearranged for temperature T^{n+1} and T^n as

$$\left[I-\frac{\alpha\triangle t}{2}\left(\xi_x^2+\xi_y^2\right)A_\xi-\frac{\alpha\triangle t}{2}\left(\eta_x^2+\eta_y^2\right)A_\eta\right]T^{n+1} \tag{3.8}$$
$$=T^n+\frac{\alpha\triangle t}{2}\left(\xi_x^2+\xi_y^2\right)A_\xi T^n+\frac{\alpha\triangle t}{2}\left(\eta_x^2+\eta_y^2\right)A_\eta T^n$$
$$+2\alpha\triangle t\left(\xi_x\eta_x+\xi_y\eta_y\right)B_\xi B_\eta T^n+\frac{\alpha\triangle t}{y}\left(\xi_y B_\xi T^n+\eta_y B_\eta T^n\right)$$

To calculate the 2-step, add and subtract the cross term to both sides of Eq. (3.8), and transfer the minus cross term to the right side.

$$\left[I-\frac{\alpha\triangle t}{2}\left(\xi_x^2+\xi_y^2\right)A_\xi\right]\left[I-\frac{\alpha\triangle t}{2}\left(\eta_x^2+\eta_y^2\right)A_\eta\right]T^{n+1} \tag{3.9}$$
$$=\left[I+\frac{\alpha\triangle t}{2}\left(\xi_x^2+\xi_y^2\right)A_\xi\right]\left[I+\frac{\alpha\triangle t}{2}\left(\eta_x^2+\eta_y^2\right)A_\eta\right]T^n$$
$$+2\alpha\triangle t\left(\xi_x\eta_x+\xi_y\eta_y\right)B_\xi B_\eta T^n+\frac{\alpha\triangle t}{y}\left(\xi_y B_\xi T^n+\eta_y B_\eta T^n\right)$$
$$+\frac{\alpha^2\triangle t^2}{4}\left(\xi_x^2+\xi_y^2\right)\left(\eta_x^2+\eta_y^2\right)A_\xi A_\eta\left(T^{n+1}-T^n\right)$$

$$cross\ term:\ \frac{\alpha^2\triangle t^2}{4}\left(\xi_x^2+\xi_y^2\right)\left(\eta_x^2+\eta_y^2\right)A_\xi A_\eta T^{n+1\text{ or }n} \tag{3.10}$$

In equation (3.9), the rightmost term of the right-hand side can be ignored without loss of accuracy because the error order is the same with the truncation error[8], so equation (3.9) can be organized in 2-step as follows.

$$T^{*}=\left(I-\frac{\alpha\triangle t}{2}\left(\eta_x^2+\eta_y^2\right)A_\eta\right)T^{n+1} \tag{3.11}$$

$$\begin{aligned}&\left[I-\frac{\alpha\triangle t}{2}\left(\xi_x^2+\xi_y^2\right)A_\xi\right]T^{*} \\ &=\left[I+\frac{\alpha\triangle t}{2}\left(\xi_x^2+\xi_y^2\right)A_\xi\right]\left[I+\frac{\alpha\triangle t}{2}\left(\eta_x^2+\eta_y^2\right)A_\eta\right]T^{n} \\ &\quad+2\alpha\triangle t\left(\xi_x\eta_x+\xi_y\eta_y\right)B_\xi B_\eta T^{n}+\frac{\alpha\triangle t}{y}\left(\xi_y B_\xi T^{n}+\eta_y B_\eta T^{n}\right)\end{aligned} \tag{3.12}$$

Equation (3.12) is first calculated by the tri-diagonal matrix method in the ξ direction. The boundary condition used is as follows. Subscript 1 and IM are the left and right boundary coordinate values in the ξ direction, respectively.

$$T_{1,j}^{*}=T_{1,j}^{n+1}-\frac{\alpha_{1,j}\triangle t}{2}\left(\eta_x^2+\eta_y^2\right)_{i,j}\frac{T_{1,j+1}^{n+1}-2T_{1,j}^{n+1}+T_{1,j-1}^{n+1}}{\triangle\eta^2} \tag{3.13}$$

$$T_{IM,j}^{*}=T_{IM,j}^{n+1}-\frac{\alpha_{IM,j}\triangle t}{2}\left(\eta_x^2+\eta_y^2\right)_{IM,j}\frac{T_{IM,j+1}^{n+1}-2T_{IM,j}^{n+1}+T_{IM,j-1}^{n+1}}{\triangle\eta^2} \tag{3.14}$$

After the calculation of Equation (3.12), the (n+1)th temperature distribution is obtained by calculating the equation (3.11) again using the tri-diagonal matrix method for the η direction.

3.4. Boundary condition of Structure analysis code

In order to analyze the temperature distribution of the structure, the wall temperature boundary condition should be obtained. The wall temperature is calculated using the energy balance equation where the sum of the heat at the interface is zero. Using this energy balance, the wall temperature can be obtained by the Newton-Raphson method with the wall temperature as a variable.

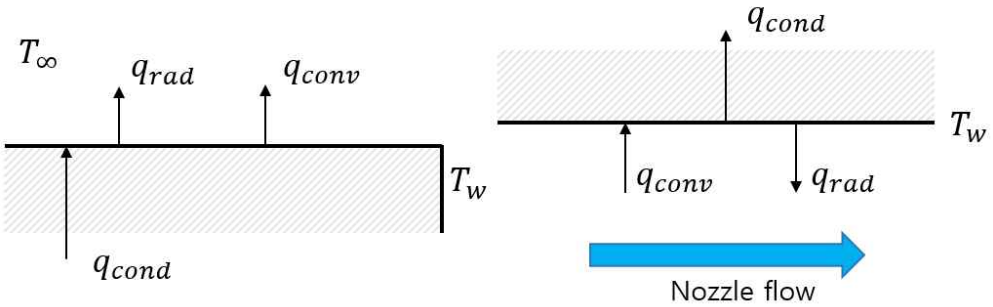

Figure 3.4 External surface(left), Nozzle inner boundary surface (right)

3.4.1. External boundary surface in contact with air

$$q_{conv} + q_{rad} - q_{cond} = 0 \tag{3.15}$$

$q_{conv} = h_\infty (T_w - T_\infty)$: Convection heat transfer with air

3.4.2. Inner boundary surface

$$q_{conv} - q_{rad} - q_{cond} = 0 \tag{3.16}$$

q_{conv} : convective heat transfer due to flow

q_{cond} : conductive heat transfer$\left(= -k\frac{\partial T}{\partial y}\right)_w$

q_{rad} : radiative heat transfer$\left(= \epsilon\sigma T_w^4\right)$

4

VALIDATION OF FLOW/STRUCTURE INTEGRATED ANALYSIS CODE

4.1. Validation of flow analysis code

To verify whether the flow analysis code developed in this study works correctly and whether the results of the flow analysis are reliable, two problems were solved and the verification work was performed. First, the validation is conducted which is axisymmetric two-dimensional inviscid flow Euler code with Converging-Diverging Verification Nozzle problem[2] provided by NASA CFD verification homepage[3]. To validate the inviscid Euler flow code, calorically perfect gas assumption of air without chemical reaction is applied. In addition, the supersonic flat plate flow problem is solved and the axisymmetric two-dimensional viscous equilibrium flow N-S code validation work is performed. It is compared the results of the flow analysis with the assumption of the calorically perfect gas and the results of the equilibrium flow analysis using the CEA database.

2) https://www.grc.nasa.gov/www/wind/valid/cdv/cdv.html
3) https://www.grc.nasa.gov/www/wind/valid/

4.1.1. NASA CDV Nozzle study

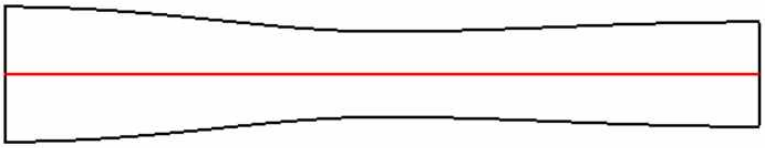

Figure 4.1 Converging-Diverging Verification (CDV) Nozzle (red is centerline)

The CDV nozzle is a problem of comparing the calculated value of the flow properties with the theoretical value with assumption that there is no viscous and conduction, which is a typical steady compressible flow problem. The stagnation pressure and stagnation temperature of the nozzle plenum are constant values are summarized in Table 4.1. Since the nozzle flow is determined by the nozzle outlet pressure condition, three values were selected for this problem and the change in the nozzle flow pattern is confirmed according to the outlet pressure value.

▸ **Flow pattern according to three outlet pressures**

$p_{exit}/p_t = 0.89$: subsonic, isentropic flow

$p_{exit}/p_t = 0.75$: supersonic flow with a normal shock in the diffusing section

$p_{exit}/p_t = 0.16$: supersonic, isentropic flow

Table 4.1 CDV Nozzle problem flow condition

Plenum Total Pressure [psi]	1.0
Plenum Total Temperature [R]	100.0
Inflow Mach Number	0.2
Exit Static Pressures [psi]	0.89 0.75 0.16

The nozzle grid is provided on the NASA CFD validation homepage and is shown in Figure 4.2.

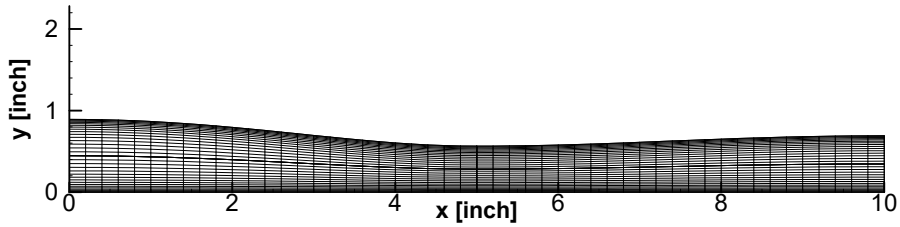

Figure 4.2 NASA CDV Nozzle 51x31 grid

Since the analytical solution along the center line is provided on the NASA validation homepage, the results of the flow analysis code that performed the flow analysis are compared and summarized. It is confirmed that the all of the code results are almost same with analytical solutions for three flow outlet pressures. In this paper, the graph of the result of the second case is presented(Figure 4.3-4), which can confirm both subsonic, supersonic and shock.

In addition, NASA's homepage provides contour graphs of the Mach number distribution by NASA's CFD code as shown in Figure 4.5, and the flow code results of this study are compared with the same contour level as NASA’s contour graphs. It is confirmed that the entire flow area is similar to that of NASA, and in the case (b), the developed code can be confirmed that no vibration occurs after the shock wave.

▸ **Supersonic flow with a normal shock,** $p_{exit}/p_t = 0.75$

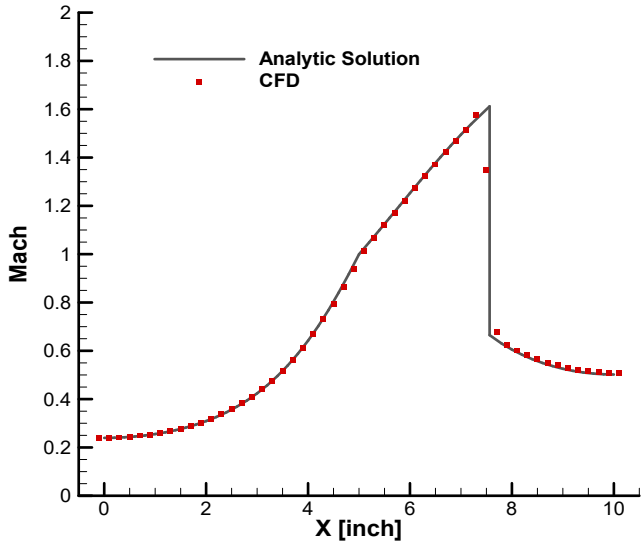

Figure 4.3 CD Nozzle Axial Mach Number. Pexit = 0.75 psi (Shock in Diffuser) Developed CFD Code

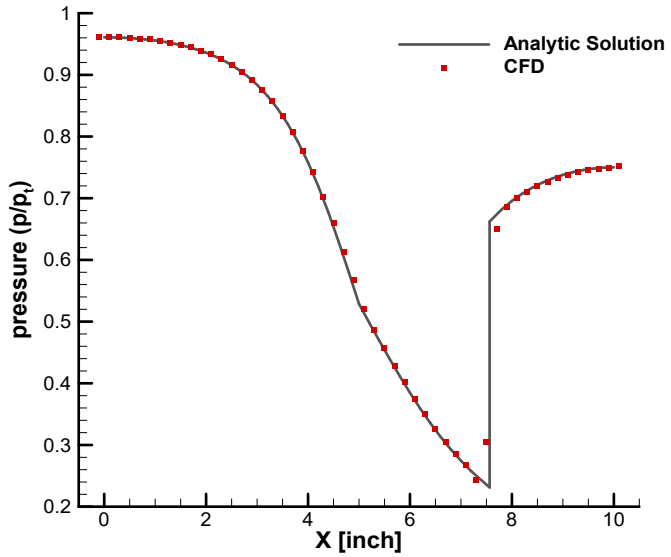

Figure 4.4 CD Nozzle Axial Static Pressure. Pexit = 0.75 psi (Shock in Diffuser) Developed CFD Code

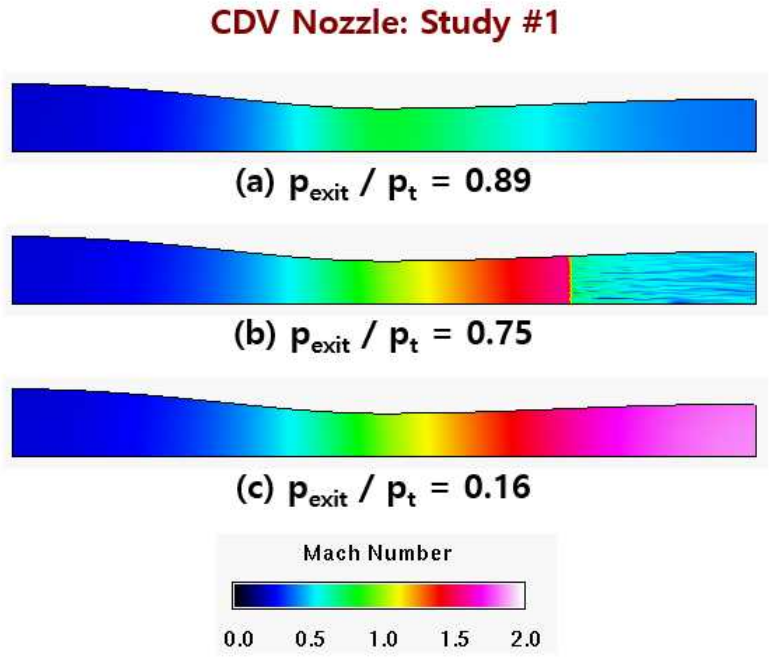

Figure 4.5 Mach number contours for CDV Nozzle of NASA

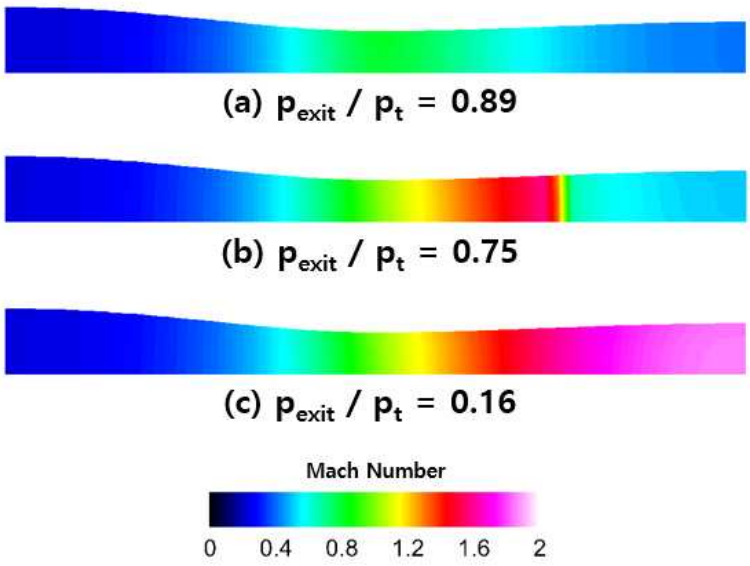

Figure 4.6 Mach number contours for CDV Nozzle of Developed CFD Code

4.1.2. Validation of hypersonic flow on flat plate

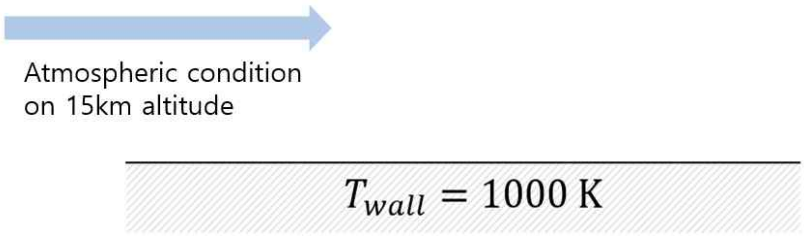

Figure 4.7 Schematic of flat plate problem

In the previous work, the validation of axisymmetric two-dimensional inviscid calorically perfect gas flow was performed. To validate the accuracy of the flow variable calculation using the viscous flux and CEA database, the hypersonic flat plate problem is treated at a wall temperature of 1,000 K at a free flow Mach number of 8, and then the test results are compared with the Van Driest correlation[9][10]. Free-flow conditions using atmospheric conditions on 15 km altitude are shown in Table 4.2 below. The grid used in the calculation is shown in Figure 4.8.

Table 4.2 Flat plate problem free stream condition

Mach Number M_∞	8.0
Pressure p_∞ [bar]	1.21114
Temperature T_∞ [K]	216.65
Wall Temperature T_{wall} [K]	1,000

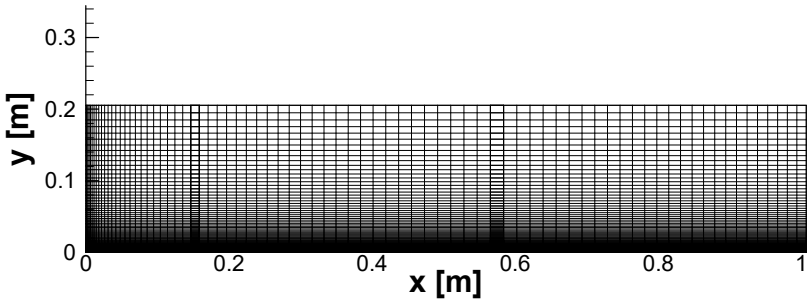

Figure 4.8 Flat plate problem 80x160 grid

To calculate the equilibrium flow using the CEA database, the (ρ,e), (T,p) tables of the five air species(N_2, NO, N, O_2, O) is prepared. The chemical composition assigned to the initial values are nitrogen(N_2) of 79% and oxygen(O_2) of 21%.

The wall pressure is compared to verify that the flow analysis using the CEA database was performed properly, as shown in Figure 4.9. The graph shows that the result of the equilibrium flow using the CEA database agrees well with that of calorically perfect gas.

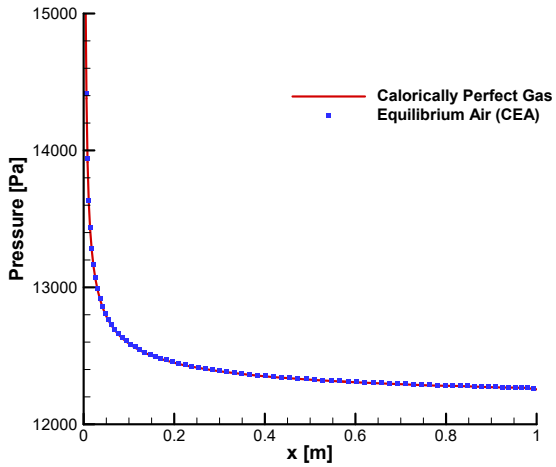

Figure 4.9 Flat plat wall pressure vs. x

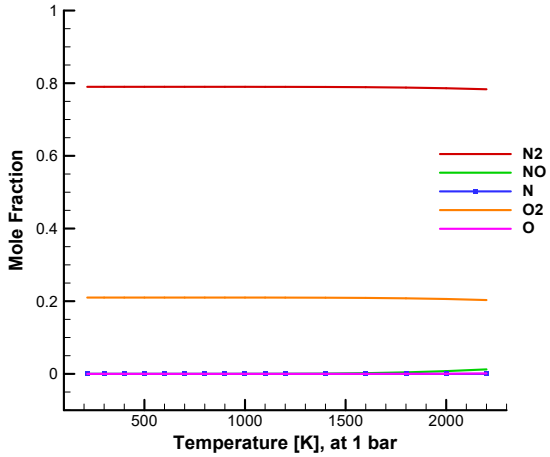

Figure 4.10 Gas composition of equilibrium air versus temperature at 1 bar. (5 species) using CEA database

For the viscous flux verification, the Van Driest's theoretical value of the wall friction coefficient C_f versus Reynolds number Re_x is compared with the flow analysis results(Figure 4.11).

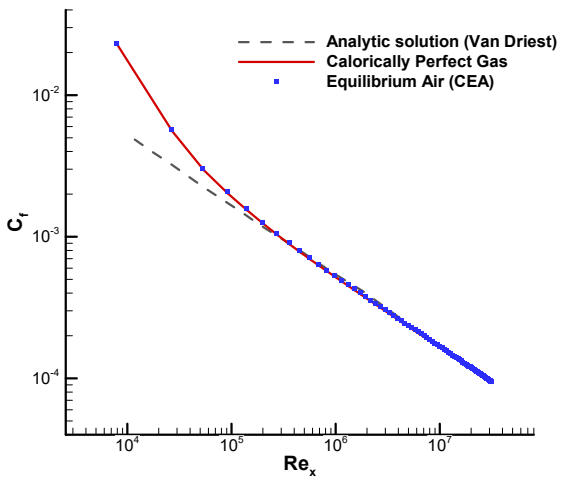

Figure 4.11 C_f vs. Re_x, Comparison with Van Driest's Analytic solution

As shown in the graph, the results of the equilibrium and calorically perfect gas flow analysis agree well with the theoretical values of Van Driest except for some initial points at which the plate starts.

4.2. Validation of structure analysis code

After the development of the structural analysis code, the two-dimensional duct flow equation was analyzed for validation. A two-dimensional duct flow is a flow through a tube whose cross-section is rectangular(Figure 4.12).

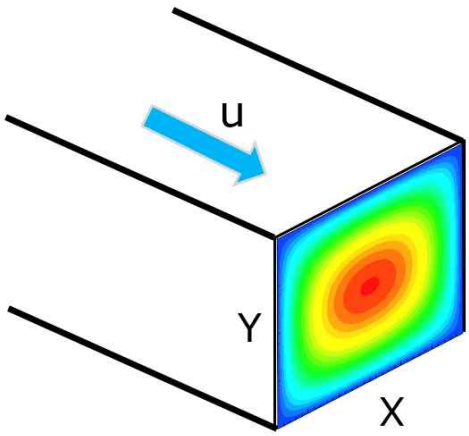

Figure 4.12 Cross-sectional schematic of flow filed of duct flow

The governing equation of duct flow is as shown in the following equation (4.1), and can be rewritten in the form of equation (4.2). By analyzing the governing equations, it can be confirmed how the longitudinal velocity of the flow is distributed in the duct section under steady state conditions.[9]

$$\mu\left(\frac{\partial^2 u}{\partial x^2}+\frac{\partial^2 u}{\partial y^2}\right)-\frac{\partial p}{\partial z}=0 \tag{4.1}$$

$$\alpha\frac{\partial^2 u}{\partial x^2}+\alpha\frac{\partial^2 u}{\partial y^2}+1=0 \tag{4.2}$$

If the virtual time is introduced to obtain the converged solution, the equation is rewritten as

$$\frac{\partial u}{\partial \tau}=\alpha\frac{\partial^2 u}{\partial x^2}+\alpha\frac{\partial^2 u}{\partial y^2}+1 \tag{4.3}$$

u : longitudinal velocity μ : viscosity

z : longitudinal direction $\frac{\partial p}{\partial z}$: longitudinal pressure gradient of duct

$\alpha=-\frac{\mu}{dp/dz}$ τ : pseudo time

The form of the governing equations of the two-dimensional duct flow with virtual time are the same as those of the two-dimensional axisymmetric heat transfer equation, so that the structure analysis code created to solve the heat transfer equations can be used as is. Therefore, the two-dimensional axial symmetric heat transfer equation analysis code can be validated by comparing the result of the two-dimensional duct flow with the analysis solution.

Two-Dimensional Axisymmetric Heat Transfer Equation :

$$\frac{\partial T}{\partial t}=\alpha\frac{\partial^2 T}{\partial x^2}+\alpha\frac{\partial^2 T}{\partial y^2}+\frac{\alpha}{y}\frac{\partial T}{\partial y}$$

Two-Dimensional duct flow governing equation :

$$\frac{\partial u}{\partial \tau}=\alpha\frac{\partial^2 u}{\partial x^2}+\alpha\frac{\partial^2 u}{\partial y^2}+1$$

The conditions of the two-dimensional duct flow problem are shown in

Table 4.3 below. Figure 4.13 shows the result of the code analysis.

Table 4.3 Duct flow problem condition

Width [m]	3.0
Height [m]	2.0
Viscosity [Pa • s]	0.4
Pressure gradient [Pa/m]	-10

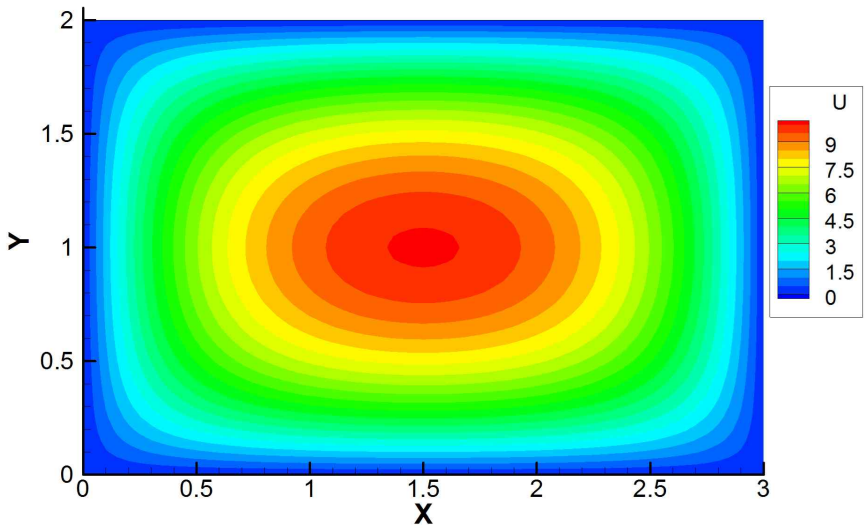

Figure 4.13 Duct flow axial velocity distribution contour

In order to validate the results of the code analysis, it is compared with the analytical solution of the two-dimensional duct flow governing equation[11]. (Figure 4.14) Analytic solution is as follow equation (4.4). Figure 4.14 shows that the analytic solution and code analysis result are in good agreement.

$$u_a(x,y) \tag{4.4}$$

$$= \frac{16L^2}{\mu\pi^3}\left(-\frac{dp}{dz}\right)\sum_{m=1,3,5,\ldots}^{\infty}(-1)^{(m-1)/2}\left[1-\frac{\cosh\left(\frac{m\pi y}{2L}\right)}{\cosh\left(\frac{m\pi h}{2L}\right)}\right]\frac{\cosh\left(\frac{m\pi x}{2L}\right)}{m^3}$$

$$(L=1.5, h=1.0)$$

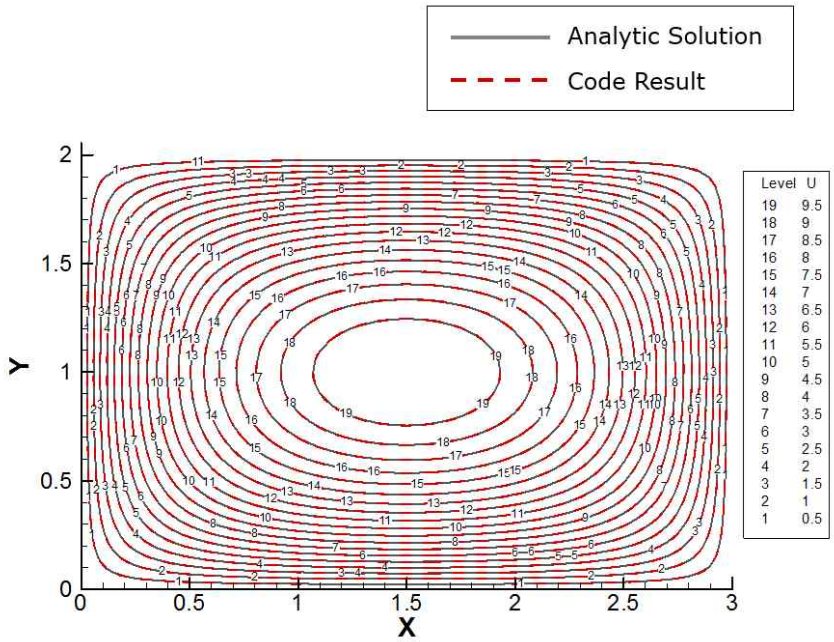

Figure 4.14 Comparison between analytic solution and code result

5

ABLATION MODEL

5.1. SiC oxidation

Silicon Carbide (SiC) is used as a material of thermal protection system in the aerospace industry because it has the advantages of reducing weight due to its low density and excellent resistance to flame and ablation.[12] The SiC exposed to the high temperature environment reacts with the oxidants to produce gaseous species such as SiO and CO and produce a thin layer of SiO_2 on the surface in specific temperature and pressure range.[13] Since the SiO_2 layer reduces the amount of thermochemical erosion by reducing the SiC surface area in contact with the high temperature flow, SiC is used for coating on the surface of other thermal protection materials such as Carbon/Carbon. The oxidation reaction of SiC is classified into 1)active oxidation, which occurs when the partial pressure of oxidants such as O_2, H_2O, CO_2 is low, 2)passive oxidation which occurs when the partial pressure of oxidants is high, and 3)active to passive transition which occurs in the range therebetween.[14][15]

5.1.1. Passive oxidation

In an environment where the surface temperature of the SiC is sufficiently low and the oxidant partial pressure is sufficiently high, a SiO_2 layer is formed on the surface of the SiC and the ablation of the SiC is delayed.

This SiO_2 formation reaction is called passive oxidation, and typical passive oxidation reaction formulas are shown in Table 5.1 below. The oxidation of SiC directly produces a SiO_2 layer by reaction <1-5>. Si_2N_2O and Si_3N_4 participate as an intermediate product to produce the SiO_2 layer by reaction <6-8> and reaction <9-10> respectively.

Table 5.1 Passive oxidation reaction equations

No.	Reaction formula			Ref.
<1>	$SiC_{(s)} + 2O_{2(g)}$	→	$SiO_{2(s)} + CO_{(g)} + \frac{1}{2}O_{2(g)}$	[13]
<2>	$SiC_{(s)} + 2O_{2(g)}$	→	$SiO_{2(s)} + CO_{2(g)}$	[16]
<3>	$2SiC_{(s)} + 3O_{2(g)}$	→	$2SiO_{2(s)} + 2CO_{(g)}$	[17]
<4>	$SiC_{(s)} + 3H_2O_{(g)}$	→	$SiO_{2(s)} + CO_{(g)} + 3H_{2(g)}$	[17]
<5>	$SiC_{(s)} + 3CO_{2(g)}$	→	$SiO_{2(s)} + 4CO_{(g)}$	[18]
<6>	$2SiC_{(s)} + CO_{(g)} + N_{2(g)}$	→	$Si_2N_2O_{(g)} + 3C_{(s)}$	[16]
<7>	$2SiC_{(s)} + CO_{(g)} + (5/2)N_{2(g)}$	→	$Si_2N_2O_{(g)} + 3CN_{(g)}$	[16]
<8>	$Si_2N_2O_{(g)} + (3/2)O_{2(g)}$	→	$2SiO_{2(s)} + N_{2(g)}$	[16]
<9>	$3SiC_{(s)} + 4N_{2(g)}$	→	$Si_3N_{4(s)} + 3C_{(s)}$	[16]
<10>	$Si_3N_{4(s)} + 3O_{2(g)}$	→	$3SiO_{2(s)} + 2N_{2(g)}$	[16]

5.1.2. Active oxidation

Active oxidation is the case where the SiO_2 layer is no longer blocking the oxidation of SiC or the SiO_2 layer is removed.[13] Typical active oxidation reaction formulas are shown in Table 5.2. SiC is directly oxidized by O_2, H_2O, CO_2 due to the reaction <11-16> and SiO_2 is removed by reaction <17-18>. The reaction <19-21> occurs at the interface between SiC and the SiO_2 layer formed on the surface. Due to this reaction it is thinned the SiC and the SiO_2 layer.

Table 5.2 Active oxidation reaction equations

No.	Reaction formula			Ref.
<11>	$SiC_{(s)} + O_{2(g)}$	→	$SiO_{(g)} + CO_{(g)}$	[13]
<12>	$2SiC_{(s)} + 3O_{2(g)}$	→	$2SiO_{(g)} + 2CO_{2(g)}$	[16]
<13>	$SiC_{(s)} + H_2O_{(g)} + H_{2(g)}$	→	$SiO_{(g)} + CH_{4(g)}$	[16]
<14>	$SiC_{(s)} + 2H_2O_{(g)}$	→	$SiO_{(g)} + CO_{(g)} + 2H_{2(g)}$	[16]
<15>	$SiC_{(s)} + CO_{(g)} + N_{2(g)} + H_{2(g)}$	→	$SiO_{(g)} + 2HCN_{(g)}$	[16]
<16>	$SiC_{(s)} + 2CO_{2(g)}$	→	$SiO_{(g)} + 3CO_{(g)}$	[15]
<17>	$SiO_{2(s)} + H_{2(g)}$	→	$SiO_{(g)} + H_2O_{(g)}$	[16]
<18>	$2SiO_{2(s)}$	→	$2SiO_{(g)} + O_{2(g)}$	[19]
<19>	$SiC_{(s)} + 2SiO_{2(s)}$	→	$3SiO_{(g)} + CO_{(g)}$	[20]
<20>	$SiC_{(s)} + SiO_{2(s)}$	→	$2SiO_{(g)} + C_{(s)}$	[20]
<21>	$2SiC_{(s)} + SiO_{2(s)}$	→	$3Si_{(l,s)} + 2CO_{(g)}$	[20]

5.1.3. Active to Passive Transition

On the SiC surface, the active oxidation sustains the ablation while the passive oxidation reduces the ablation with the same reactants species. It is therefore important to know the temperature and pressure conditions that distinguish the two oxidation reactions, which have completely different results. Active to passive transition is an intermediate reaction in which an active oxidation reaction is converted into a passive oxidation reaction, and the conditions under which the transition occurs are investigated to distinguish the conditions under which the two oxidation reactions occur.

▸ **Wagner model**

In 1958 Wagner[21] proposed an oxidation model that can determine the temperature and pressure conditions under which active to passive transition of SiC occurs. In Wagner's model, the SiO partial pressure is low at the beginning of the oxidation of SiC, so that active oxidation reaction occurs and the partial pressure of SiO on the SiC surface rises. The SiO density boundary layer is formed by the influence of the SiO generation rate and the diffusion rate of the SiO gas on the SiC surface(Figure 5.1).

Wagner expressed the oxygen partial pressure $P^{t}_{O_2}(W)$ as equation (5.1) at which the active to passive transition takes place, taking into account the boundary layer thickness δ and the mass flux of the gas molecules J. In this equation, D is the diffusion coefficient, and P^{eq}_{SiO} is the partial pressure of SiO_2 when the reaction<18> is in an equilibrium state. In the Wagner model, passive oxidation occurs when the oxygen partial pressure is greater than $P^{t}_{O_2}(W)$, and active oxidation occurs when less than $P^{t}_{O_2}(W)$.

$$P^{t}_{O_2}(W) = (D_{SiO}/D_{O_2})^{1/2} P^{eq}_{SiO} \tag{5.1}$$

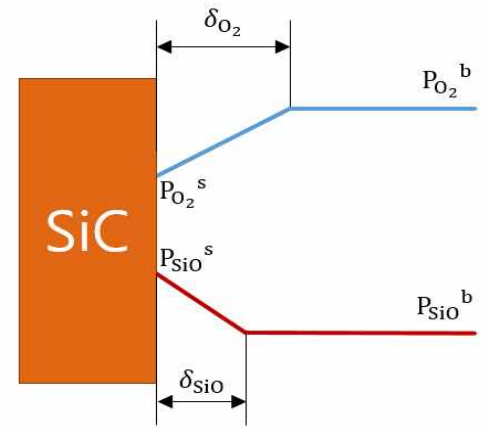

Figure 5.1 Pressure profiles of O_2 and SiO for Wagner model

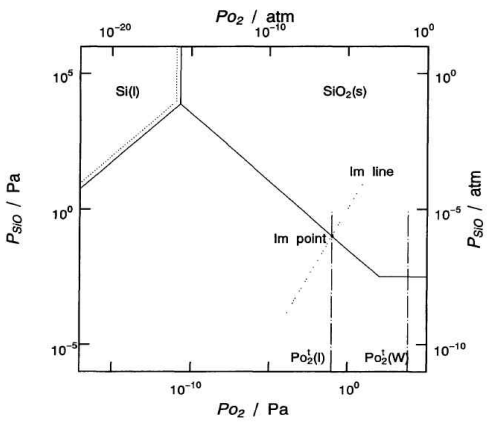

Figure 5.2 Volatility diagram of SiC-O_2-Ar system at 1873 K [14]

▸ **Heuer model**

Heuer[19][22] described the active to passive transition by presenting the volatility diagram as shown in Figure 5.2. In Figure 5.2, a solid line crossing the center diagonally represents the partial pressure at the equilibrium state of the reaction<18>. The oxygen partial pressure at the point where this solid line and the isomolar (Im) line meet is called $P^{t}_{O_2}(I)$. The Im line is a line

that takes into account the fact that when the chemical reaction takes place, the total number of moles of the species can vary, but the total number of mass before and after the reaction is preserved. $SiO_{2(s)}$ smoke generation begins when the oxygen partial pressure reaches $P^{t}_{O_2}(\mathrm{I})$, and then SiO_2 will condense and $SiO_{2(s)}$ protective layer will be formed on the SiC surface. Active to passive transition occurs.

Heuer[22] presents the volatility diagram for SiC materials based on the above oxidation model(Figure 5.3). If we know the temperature, pressure, and gas composition, we can use this diagram to predict how the oxidation will occur. The higher the temperature, the larger the oxygen partial pressure required for passive oxidation to occur, and thus the temperature and pressure ranges at which active oxidation occurs are increased.

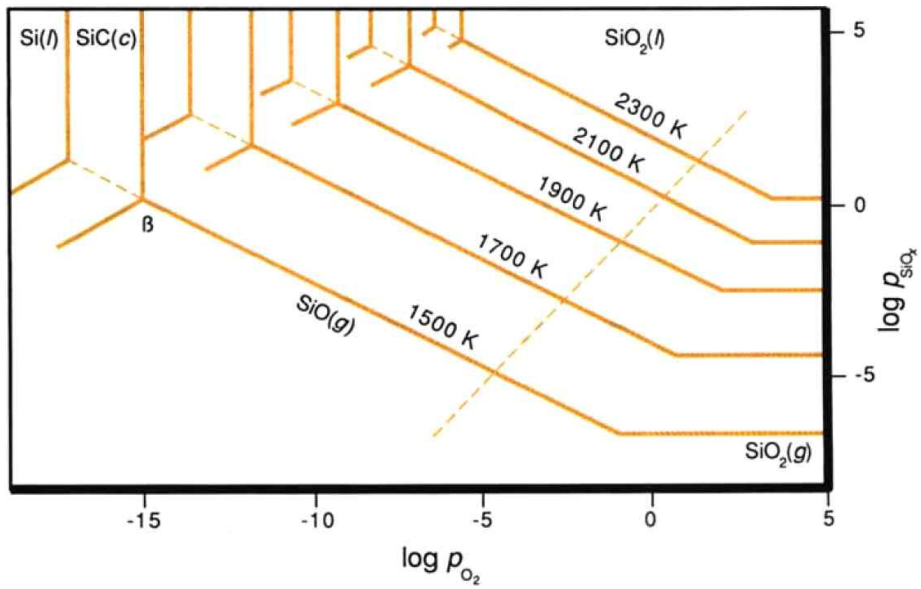

Figure 5.3 Volatility diagram for the Si-C-O system between 1500 and 2300 K [22]

▸ **Opila model**

In this study, there is almost no oxygen in the nozzle combustion gas, and H_2O(17.5%), CO_2(4.79%) exist as oxidants for SiC oxidation(Table 2.1). The values in parentheses are the mole fractions at the combustion chamber conditions. Therefore, it is necessary to investigate the active to passive transition region in which SiC reacts with the oxidants of H_2O and CO_2. In the previous reivew the oxidation model between SiC and O_2 is presented. Opila[15] proposed a model of oxidation reaction between SiC and CO_2, H_2O. Opila presented the active oxidation of SiC with H_2O/H_2 and CO_2/CO gases as follows.

$$SiC_{(s)} + 2H_2O_{(g)} \leftrightarrow SiO_{(g)} + 2H_{2(g)} + CO_{(g)} \quad (5.2)$$

$$SiC_{(s)} + 2CO_{2(g)} \leftrightarrow SiO_{(g)} + 3CO_{(g)} \quad (5.3)$$

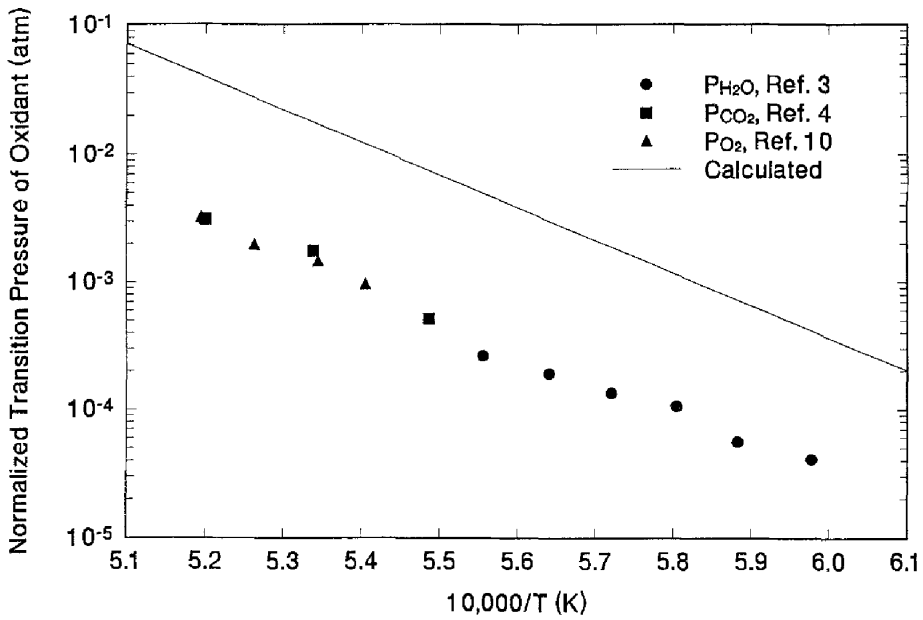

Figure 5.6 Transition pressures for various oxidants (normalized per oxygen atom basis and stoichiometry factors) as compared to that calculated for O_2 from reaction (11) [15]

Opila showed the experimental values of the oxidant partial pressure in which active to passive transition occurs in H_2O/H_2, CO_2/CO gas(Figure 5.6).

As in the case of O_2, the experimental data shows that even when the oxidant is H_2O or CO_2, the oxidant partial pressure required for the active to passive transition increases as the temperature increases. Therefore, the higher the temperature, the higher the partial pressure of the oxidants such as O_2, H_2O, and CO_2 required to cause the passive oxidation of the SiC, so that the oxidation resistance of the SiC decreases. In addition, passive oxidation is expected to occur when oxidant partial pressure is higher than 10^{-2}~10^{-4} atm under the conditions of 1,600~2,000 K.

5.2. Mechanical ablation model

Pressure of the combustion chamber used in this study is 2800 psi (193 bar), and the nozzle throat is exposed to high pressure flow. A major factor influencing the ablation of nozzle throat exposed to high-pressure flow is mechanical ablation as well as thermochemical ablation. Particularly, under high-temperature/high-pressure conditions, mechanical ablation is the main factor due to high shear stress, so consideration about mechanical ablation must be given to calculate the ablation depth precisely.

Shear erosion model is used to simulate the mechanical ablation. But, shear erosion model is classified and it will not be mentioned in this paper.

5.3. Thermochemical ablation model

5.3.1. Equilibrium gas kinetics ablation model

Since high-temperature combustion gas is emitted from the nozzle combustion chamber, it is essential to consider thermochemical ablation as a main factor of ablation of the nozzle throat where the heat load is concentrated. In

this study, because about 140 μm SiC layers were coated on the surface of the nozzle throat, the oxidation of the SiC coating layer was considered as thermochemical ablation phenomenon. The nozzle combustion gases are composed of 16 chemical species as shown in Table 2.1. Among the chemical species that can act as an oxidant for the SiC oxidation at a relatively large mole fraction are CO2(4.793%) and H2O(17.568%). The main oxidation reactions of SiC reacting with these species are as follows.

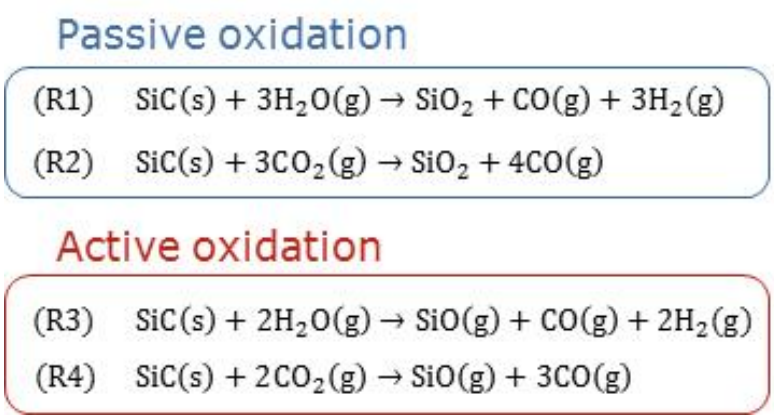

Figure 5.7 The main oxidation reaction formular of SiC

Since the above main oxidation reaction does not have a literature reference of the reaction rate coefficient, a new model of ablation using molecular kinetic theory is designed to calculate the amount of thermochemical ablation. The difference between the incoming mass flow rate to the nozzle wall and the exiting mass flow rate from the nozzle wall after reaction with SiC coating was calculated. The amount of thermochemical ablation that SiC exits to the gaseous state by reacting with the combustion gas is proportional to the amount of Si molecules exiting in the form of SiO molecules. Therefore, in order to calculate the ablation rate of SiC coating layer, the net mass flux of the SiO gas generated by the oxidation reaction of SiC was calculated, and

then the mass flux of Si is chased.

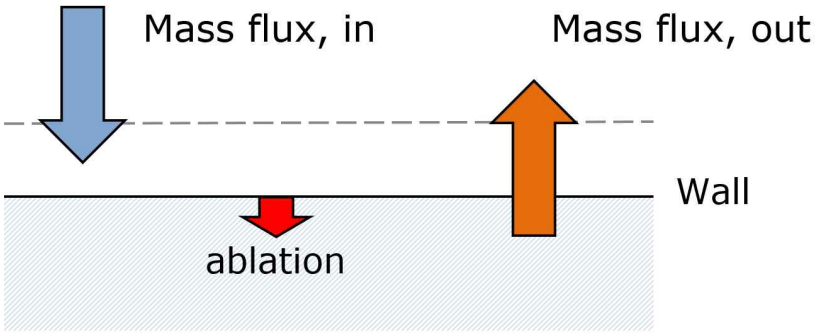

Figure 5.8 Schematic of equilibrium gas kinetics ablation model

$$
\begin{aligned}
J_{Si} &= \frac{1}{4} C_{w,SiO} \triangle(\rho_w \alpha_{SiO}) \frac{m_{Si}}{m_{SiO}} \\
&= \frac{1}{4} C_{w,SiO} \triangle(n_{SiO}) m_{SiO} \frac{m_{Si}}{m_{SiO}} \\
&= \frac{1}{4} C_{w,SiO} \triangle(n_{SiO}) m_{Si}
\end{aligned}
\tag{5.4}
$$

J_s : mass flux of species s

$C_{w,s} = \sqrt{\frac{8kT}{\pi m_s}}$: average molecular speed of species s at wall

α_s : mass fraction of species s

n_s : number density

ρ_w : gas density at wall

m_s : particle mass of species s

The net $\triangle$ value is calculated by taking the exiting mass flow rate as positive, and the incoming mass flow rate as negative. The chemical species composition of the combustion gas before and after the reaction is determined

by using the mole fraction of equilibrium state with CEA. It is assumed that there are an infinite number of SiC on the surface, and the calculation results are summarized in Figure 5.9. The calculation is conducted assuming that the combustion gas pressure in the vicinity of the nozzle throat is reduced to 80 bar, and the nozzle wall temperature is increased to 1,400 K during the nozzle operation time. Since solid state SiO_2 is produced after the reaction of combustion gas with SiC, mass fraction is calculated only by the gaseous species in order to consider the amount of SiO gas exiting.

$C_{w,SiO} = 819.985\ \mathrm{m/s}$, $\triangle(n_{SiO}) = 7.909 \times 10^{15}\ \mathrm{particle/m^3}$, $m_{Si} = 4.664 \times 10^{-26}\ \mathrm{kg}$ and the result of the equation (5.4) calculated with these values is $J_{Si} = 7.5612 \times 10^{-8}\ \mathrm{kg/m^2 s}$.

J_{Si} is the amount of Si atoms escaping from the SiC surface into the combustion gas after the oxidation of SiC, and thus the gaseous mass flow rate of SiC after ablation is as follows.

$$J_{SiC} = J_{Si}\frac{m_{SiC}}{m_{Si}} = 1.07947 \times 10^{-7}\ \mathrm{kg/m^2 s} \tag{5.5}$$

The thermochemical ablation rate and depth of SiC exiting in the gaseous state after oxidation can be calculated as follows.

$$J_{SiC} = \rho_{w,SiC} V_{ablation} \tag{5.6}$$

$$V_{ablation} = \frac{J_{SiC}}{\rho_{w,SiC}}\ \ [\mathrm{m/s}] \tag{5.7}$$

$$\triangle S_{ablation} = \int V_{ablation} dt \tag{5.8}$$

Density of SiC is 3.21 $\mathrm{g/cm^3}$, thus thermochemical ablation rate is $V_{ablation} = 3.3628 \times 10^{-11}\ \mathrm{m/s} = 3.3628 \times 10^{-5}\ \mu\mathrm{m/s}$. The operating time of the nozzle

used in this study is 20 seconds, and the total depth of ablation $\triangle S_{ablation}$ is only $6.7256\times10^{-4}\,\mu\mathrm{m}$ by considering $V_{ablation}=3.3628\times10^{-5}\,\mu\mathrm{m/s}$ as average ablation rate. Therefore, it can be concluded that the equilibrium gas kinetics ablation model can not express the ablation phenomenon of this study, and it can be judged that the amount of ablation by the gaseous state SiO after the oxidation of SiC is insignificant.

화학종	CH4	CO	CO2	CL	H	HCN	HCO	HCL	H2	H2O	NH3	NO	N2	O	OH	O2	SiO	SiC(b)	SiO2(a-gr)	SiO2(b-gr)	SiO2(b-crt)	SiO2(L)	Si
분자량 [kg/(kg-mole)]	16.04246	28.0101	44.0095	35.453	1.00794	27.02534	29.01804	36.46094	2.01588	18.01528	17.03052	30.0061	28.0134	15.9994	17.00734	31.9988	44.0849	40.0962	60.0843	60.0843	60.0843	60.0843	28.0855
분자질량 [kg]	2.664E-26	4.651E-26	7.309E-26	5.887E-26	1.674E-27	4.488E-26	4.81E-26	6.054E-26	3.347E-27	2.992E-26	2.828E-26	4.983E-26	4.653E-26	2.657E-26	2.824E-26	5.314E-26	7.323E-26	6.656E-26	9.977E-26	9.977E-26	9.977E-26	9.977E-26	4.664E-26
Cvv [m/s]	1393.301	1028.712	820.688	914.376	5422.927	1047.287	1010.888	901.648	3884.588	1282.716	1319.280	993.306	1028.651	1391.129	1320.179	982.463	819.985	858.604	702.378	702.378	702.378	702.378	

반응 전	CH4	CO	CO2	CL	H	HCN	HCO	HCL	H2	H2O	NH3	NO	N2	O	OH	O2	SiO	SUM
mole fraction	1.99E-03	2.71E-01	8.38E-02	2.20E-06	2.51E-07	1.67E-05	1.32E-08	2.39E-02	2.14E-01	1.43E-01	3.47E-04	3.07E-11	2.61E-01	3.57E-15	3.59E-09	1.14E-15	0	1.000
mass fraction (gases only)	1.37E-03	3.36E-01	1.66E-01	3.60E-06	1.12E-08	2.01E-05	1.70E-08	3.93E-02	1.91E-02	1.14E-01	2.62E-04	4.08E-11	3.24E-01	2.53E-15	3.01E-09	1.62E-15	0	1.000
number density [#/m3]	8.01E-23	1.12E-25	3.46E-25	9.46E-19	1.04E-20	6.94E-21	5.49E-18	9.90E-24	8.85E-25	5.93E-25	1.43E-23	1.27E-16	1.08E-25	1.47E-12	1.65E-18	4.72E-11	0	

반응 후	CH4	CO	CO2	CL	H	HCN	HCO	HCL	H2	H2O	NH3	NO	N2	O	OH	O2	SiO	SiC(b)	SiO2(a-gr)	SiO2(b-gr)	SiO2(b-crt)	SiO2(L)	SUM
mole fraction	1.79E-05	3.01E-05	2.91E-03	1.16E-12	4.00E-13	2.00E-06	6.40E-14	2.35E-06	6.83E-07	1.03E-10	4.54E-10	1.76E-20	2.49E-05	3.49E-25	7.46E-19	2.59E-29	1.46E-15	9.99E-01	0.00E+00	0.00E+00	1.30E-05	0.00E+00	1.000
mass fraction (gases only)	1.46E-01	4.30E-01	8.53E-05	2.09E-08	2.05E-10	2.76E-02	9.46E-10	4.37E-02	7.11E-04	9.44E-07	3.94E-06	2.70E-16	3.80E-01	2.94E-21	6.46E-15	4.22E-25	3.32E-11						1.000
number density [#/m3]	9.22E-25	1.61E-25	1.55E-22	6.20E-19	2.14E-18	1.07E-25	3.41E-17	1.26E-25	3.70E-24	5.50E-20	2.42E-21	9.43E-10	1.33E-25	1.86E-06	3.96E-12	1.39E-02	7.93E-15						

△number density [#/m3]	9.15E-25	4.65E-25	-3.46E-25	-3.27E-18	-1.02E-20	1.07E-25	-5.14E-18	2.77E-24	-8.49E-25	-5.93E-25	-1.41E-23	-1.27E-16	2.53E-25	-1.47E-12	-1.65E-18	-4.72E-11	7.93E-15

Figure 5.9 Calculation of number density and molecular speed at 1400 K, 80 bar for equilibrium gas kinetics ablation model

5.3.2. Melting erosion model

Since the ablation phenomenon of this study can not be expressed only by the gaseous amount of ablation, other ablation model is adopted. As a result of the flow analysis of this study, the wall pressure of the nozzle throat is calculated to be about 80 bar and the wall temperature is about 1,000 to 1,800 K. The partial pressure of the combustion gas at 80 bar and 1,400 K is calculated as shown in Table 5.3 using CEA. The partial pressure of H_2O is about 11.5 bar and the partial pressure of CO_2 is about 6.7 bar.

Table 5.3 Partial pressure of combustion gas at 80 bar, 1400 K

Species	Mole fraction	partial pressure [bar]	Species	Mole fraction	partial pressure [bar]
CH_4	$1.9363x10^{-3}$	0.1549	H_2	$2.1402x10^{-1}$	17.1216
CO	$2.7185x10^{-1}$	21.7480	H_2O	$1.4329x10^{-1}$	11.4632
CO_2	$8.3812x10^{-2}$	6.7050	NH_3	$3.4780x10^{-4}$	0.0278
Cl	$2.2914x10^{-8}$	$1.833x10^{-6}$	NO	$3.0733x10^{-11}$	$2.459x10^{-9}$
H	$2.5184x10^{-7}$	$2.015x10^{-5}$	N2	$2.6105x10^{-1}$	20.8840
HCN	$1.6790x10^{-5}$	0.0013	O	$3.5738x10^{-15}$	$2.859x10^{-13}$
HCO	$1.3250x10^{-8}$	$1.060x10^{-6}$	OH	$3.9966x10^{-9}$	$3.197x10^{-7}$
HCl	$2.3685x10^{-2}$	1.8948	O_2	$1.1406x10^{-15}$	$9.125x10^{-14}$

The partial pressure of H_2O and CO_2 in the expected nozzle wall temperature range is much higher than the partial pressure required for the active to passive transition measured by Opila in Figure 5.6, so the oxidation of the SiC coating layer with the nozzle combustion gas is considered to be passive oxidation.

Therefore, it could be supposed that the chemical reaction that the SiO_2 layer occurs by passive oxidation occurred on the surface of the SiC coating layer, and the generated SiO_2 layer is removed, thereby causing the thermo-

chemical ablation phenomenon. It could be assumed that the surface temperature of the SiO_2 layer continuously increased due to the heat load concentrated on the nozzle throat, and then the molten SiO_2 is removed by sweeping the flow after reaching the melting point. Thus melting erosion model is adopted to simulate thermochemical ablation. But, melting erosion model is classified and it will not be mentioned in this paper.

6

ANALYSIS OF ADD's NOZZLE ABLATION TEST RESULTS

During the development of the numerical analysis code, the combustion test of the nozzle was carried out by ADD. The combustion tests were carried out up to the 5th test. The propellant, the rocket motor design condition, and the amount of ablation measurement data of the 3rd, 4th, and 5th combustion test were received from ADD. In the data received, the information necessary for the development of the ablation model and the integrated code are summarized, and the test environment of the 3rd to 5th nozzle combustion test is summarized as shown in Table 6.1 below.

Table 6.1 Summary of 3rd∼5th test environment for combustion

	3rd	4th	5th
flame temperature [K]	2710	2715	2715
chamber pressure [psi]	2800	2800	2800
nozzle throat diameter [mm]	15.40(15.16)	14.5	14.5
target test time [s]		20	
actual test time [s]	14	19	19
SiC coating thickness [μm]		135∼165	

Since the flame temperature, combustion chamber pressure, nozzle throat test environment of the 4th and 5th tests are the same, the two test environments of the 3rd test and the 4th/5th test are given as conditions of integrated code analysis. The target test time for the nozzle combustion test was 20 seconds, and in the 3rd test, the flame leaks at 14 seconds, and the ablation was no longer carried out. Both the 4th and 5th tests were completed without more than 19 seconds. The nozzle throat surface is coated with SiC of 135 to 165 μm in order to delay the ablation.

Figure 6 shows the results of measuring the amount of ablation of the nozzle throat coated with SiC in the 3rd-5th nozzle combustion test. The 4th and 5th tests have the same test environment, but different amounts of ablation have been found. The amount of ablation of the nozzle divergent section was similar, but In the 4th test, more than twice as much ablation was measured as in the 5th test. In addition, more ablation was measured in the the 14-second 3rd test than the 19-second 5th test.

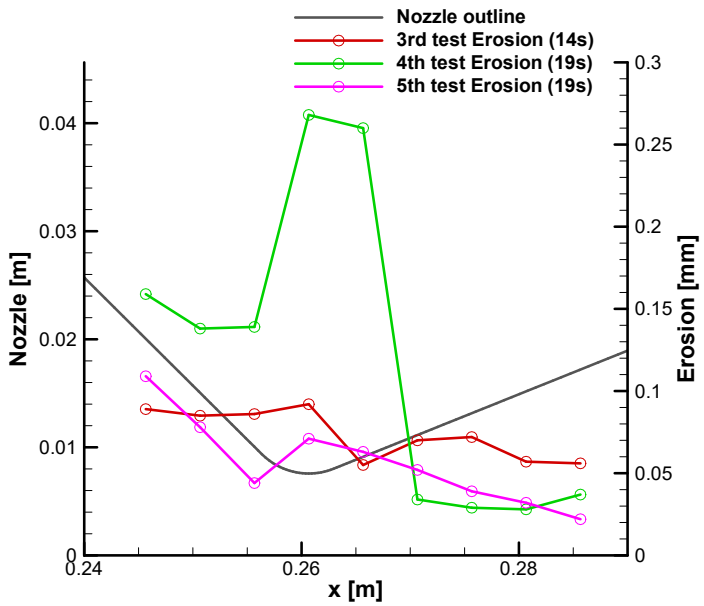

Figure 6.1 Erosion depth distribution graph by test

7

PREDICTION OF ABLATION USING INTEGRATED ANALYSIS CODE

7.1. Grid generation for flow and structure analysis

7.1.1. Flow analysis grid

In this study, we received the nozzle drawing from ADD, which is shown in Figure 7.1. Since the flow analysis area is the area inside the nozzle in the orange frame in Figure 7.1, a flow grid was created to match the shape of the inner region of the nozzle assembly.

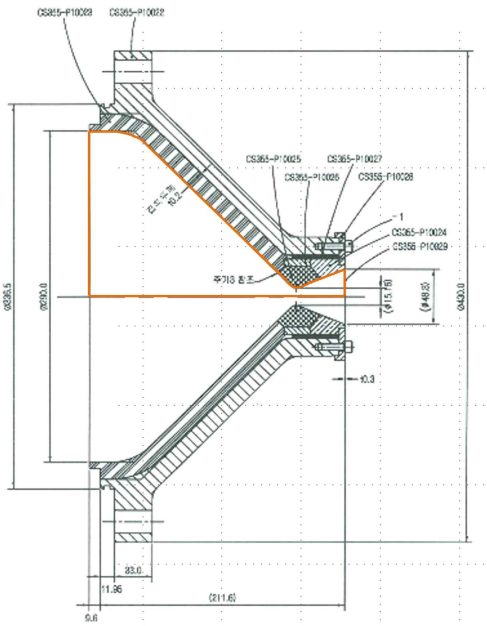

Figure 7.1 Schematic of nozzle and nozzle flow region

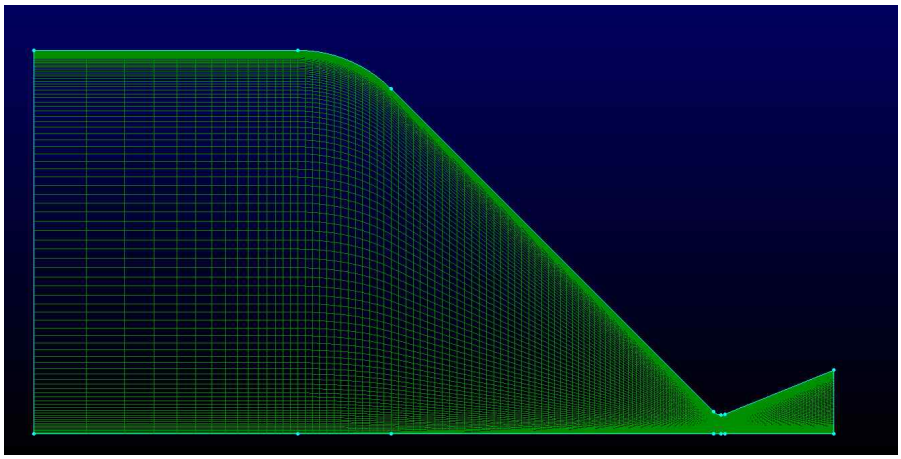

Figure 7.2 Nozzle flow grid, 190×120 cell

7.1.2. Structure analysis grid and input material properties by position

As in the case of creating the flow analysis grid, the structure analysis grid was created using the nozzle drawing. The structure analysis area is limited to the area within the orange border in Figure 7.3.

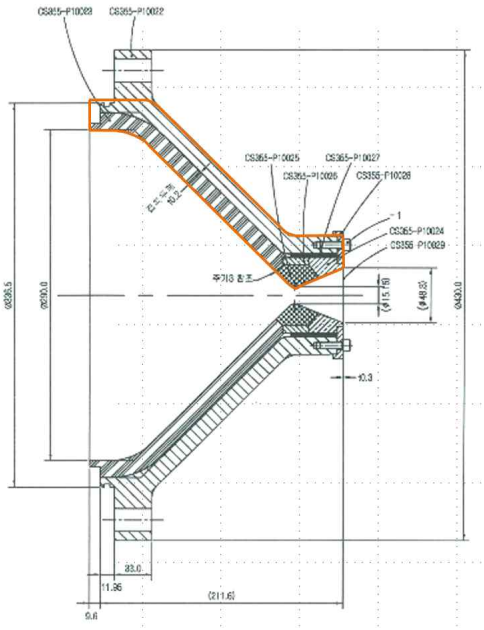

Figure 7.3 Schematic of nozzle and nozzle structure region

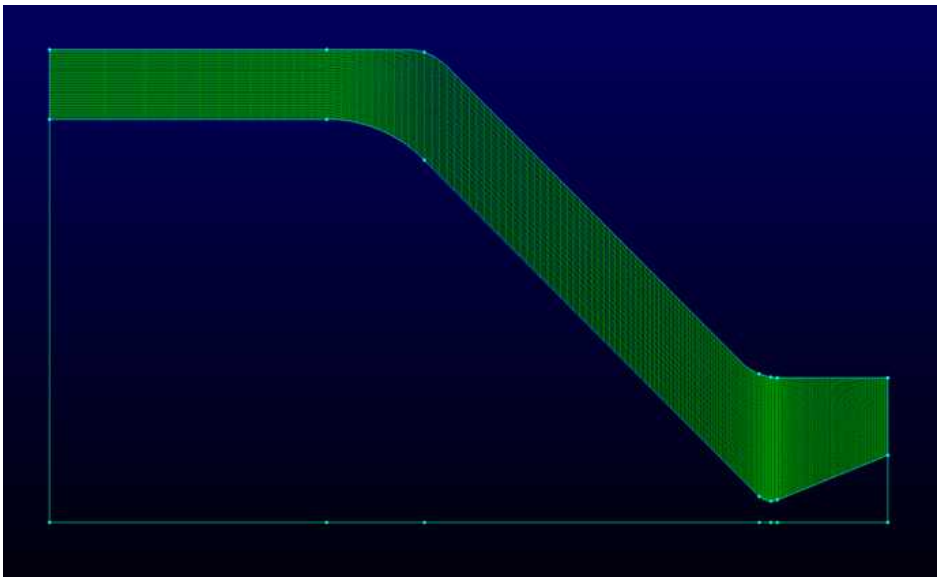

Figure 7.4 Nozzle structure grid, 190×240 cell

In order to solve the heat transfer equation in calculating the temperature distribution of the structure, density, specific heat and thermal conductivity of each material are required. The properties of materials used in this study are shown in Table 7.1. There are five materials used in structural analysis. When assigning the initial condition in the structural analysis code, the method of entering density, specific heat, and thermal conductivity by distinguishing each material with their location is chosen. The material that is input by location in the actual code is shown in Figure 7.5.

Table 7.1 Material properties (density, specific heat capacity, thermal conductivity)

part name	material	density (g/cm^3)	specific heat (J/gK)	thermal conductivity (W/mK)
nozzle throat	C/SiC	2.0	0.8	4.6
nozzle throat insulator	C/C	1.7	0.7	16.3
nozzle insulator	Glass/Phenolic	1.8	2.36	1.17
converging part heat resisting material	Carbon/Phenolic	1.3	2.3	2.55
nozzle body	AISI 4130	*7.85*	*0.523*	*42.7*

BLACK : from ADD, RED : Ref. [24]
BLUE : Existing data of this laboratory, *GREEN* : Ref. [7-2222][4)]

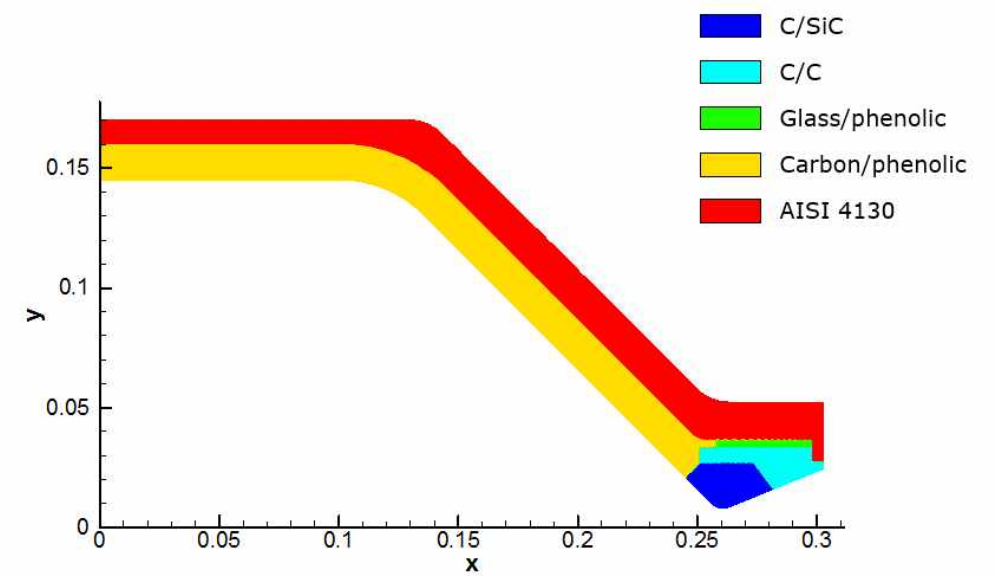

Figure 7.5 Material distribution by position of nozzle structure

4) http://asm.matweb.com/search/SpecificMaterial.asp?bassnum=m4130r

7.2. Structure material properties correction

The nozzle structure analyzed in this study consists of several kinds of materials, and the material properties of each material are different from each other, and the discontinuity of material property occurs at the interface of the structural parts. Because these properties are used to analyze the temperature distribution of the structure, numerical error occurs at the discontinuity point of the material interface and the calculation of the wall heat transfer amount may oscillate. Therefore, the discontinuous properties are corrected by a smoothing method. The heat transfer coefficient and the thermal conductivity distribution are shown in Figure 7.6 and 7.7, respectively, and these properties along the black dotted line are shown in Figure 7.8 and 7.9.

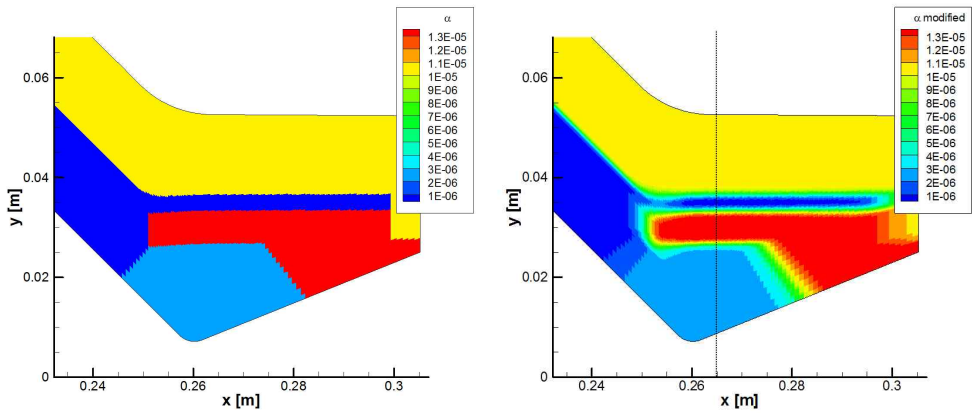

Figure 7.6 Thermal transport coefficient distribution, original(left) and modified (right)

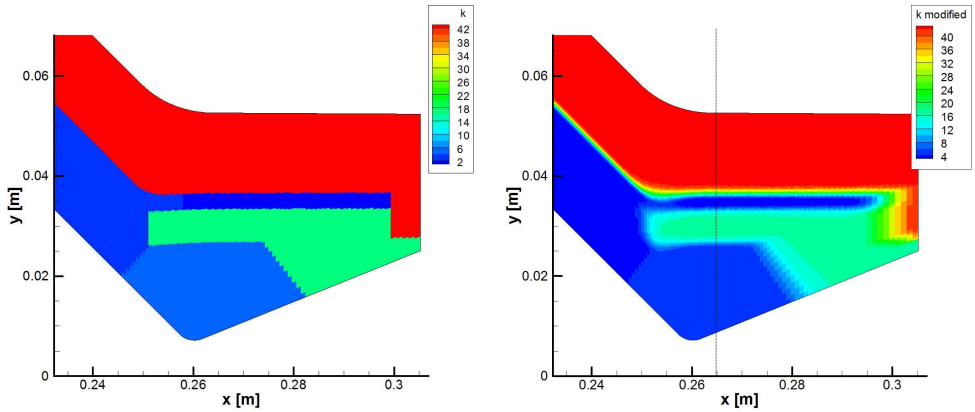

Figure 7.7 Thermal conductivity distribution, original(left) and modified (right)

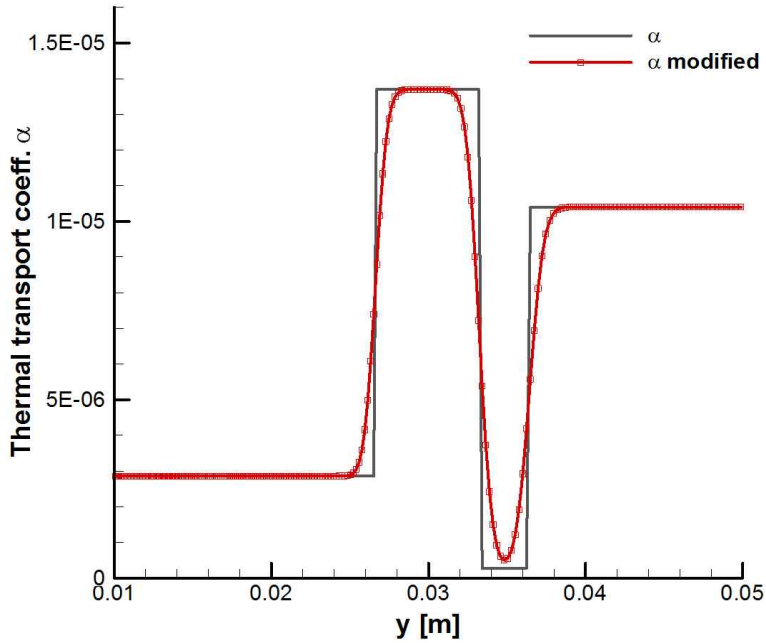

Figure 7.8 Thermal transport coefficient vs. y at x=0.265

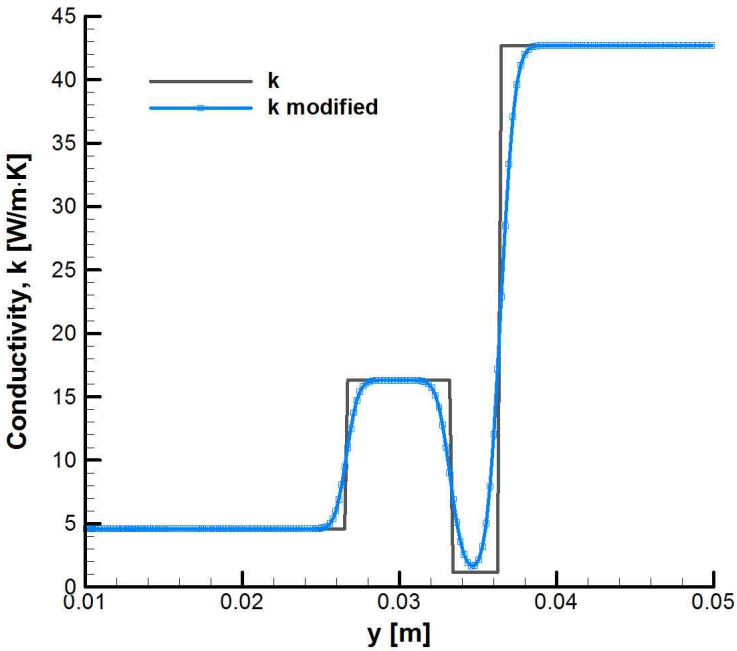

Figure 7.9 Thermal conductivity vs. y at x=0.265

7.3. Nozzle wall heat flux correction

The integrated code developed in this study performs flow and structure analysis with time advance. The flow and structure grids were used and the corrected material properties were input and then, the flow and structure analysis were performed over time. But, nozzle wall heat transfer and wall temperature oscillation occurred near the nozzle throat, and the oscillation was not suppressed, and the amplitude became large, which eventually diverged. Figure 7.10 shows the phenomenon that wall heat transfer and wall temperature oscillate and diverge from the nozzle throat position with the passage of time.

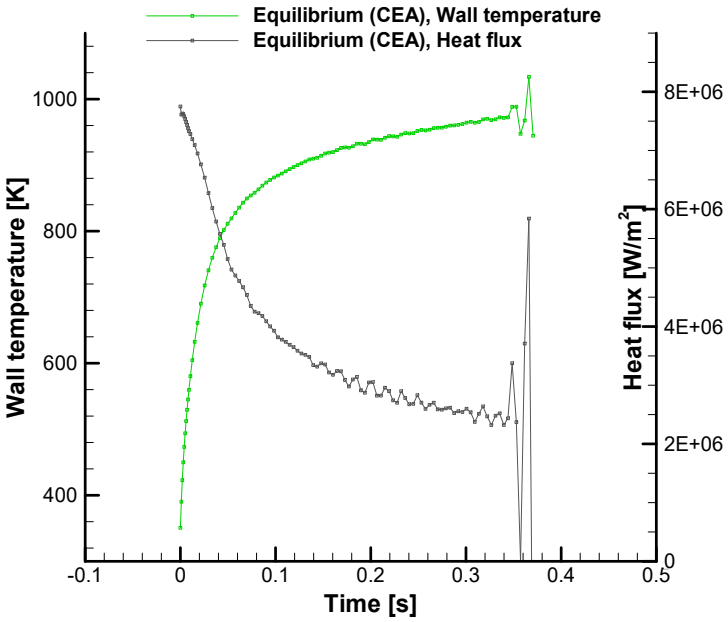

Figure 7.10 Diverged wall temperature and heat flux at nozzle throat

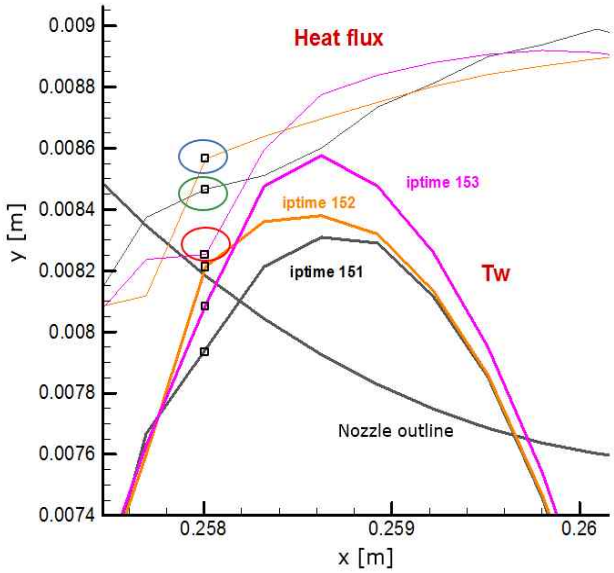

Figure 7.11 Verification of reason of heat flux oscillation

In order to eliminate the error caused by the use of CEA database, I analyzed calorically perfect gas flow which is more stable numerically to find the cause of oscillation. Figure 7.11 shows a graph of heat flux and wall temperature(Tw) at a specific moment when oscillation occurs. iptime is the physical time index.

In Figure 7.11, the heat flux value of iptime 151 indicated by the green circle was judged to be the cause of oscillation. As a result of the heat flux of iptime 151, the wall surface temperature is slightly lower at x = 0.258, which indicates that the overall convex temperature distribution is slightly distorted. Therefore, it is assumed that the heat flux amount of iptime 151 at x = 0.258, which is used to calculate the wall temperature, is calculated to be slightly smaller due to the accumulated error. It can be seen that the shape of the heat flux graph is already recessed at x = 0.258.

Then, the calculation was carried out with the wall temperature slightly reduced at the x = 0.258 position of iptime 151 as the boundary condition of the 152^{nd} flow analysis. As the temperature of the wall decreases, the temperature gradient increases. Therefore, the iptime 152 heat flux amount, which is represented by the blue circle due to the reduced wall temperature, is calculated to be larger than the expected value and becomes larger than the iptime 151 heat flux amount. Wall heat flux vibration occurred. The iptime 152 wall temperature at x = 0.258, calculated as the expected larger heat flux, would have been calculated to be greater than the value correctly calculated. This is again given as the boundary condition of iptime 153 flow analysis. Since the wall temperature is higher than expected due to the error and the temperature gradient is smaller, the heat flux amount of the iptime 153 indicated by the red circle becomes smaller than the heat flux amount of iptime 152. The wall heat flux oscillation does not disappear and its amplitude is larger than before. Also, the wall surface temperature calculated by this heat flux amount

is smaller than the iptime 152 wall surface temperature, and the wall surface temperature oscillation also occurs.

If the wall heat flux amount is calculated to be smaller than expected, the oscillation occurs, and the oscillation does not decrease, and the size of the magnitude becomes larger and larger. In order to suppress the oscillation of the wall heat flux amount, a method of correcting the heat flux amount smaller than expected is adopted. If it is determined that the heat flux amount at a specific position is smaller than the surrounding heat flux amount, smaller one is filled by smoothing with the surround heat flux amount. An example is shown in Figure 7.12. The jagged heat flux(blue) near the nozzle throat is smoothened into the orange graph, and the corrected heat flux is transferred to the boundary condition of the structure analysis code.

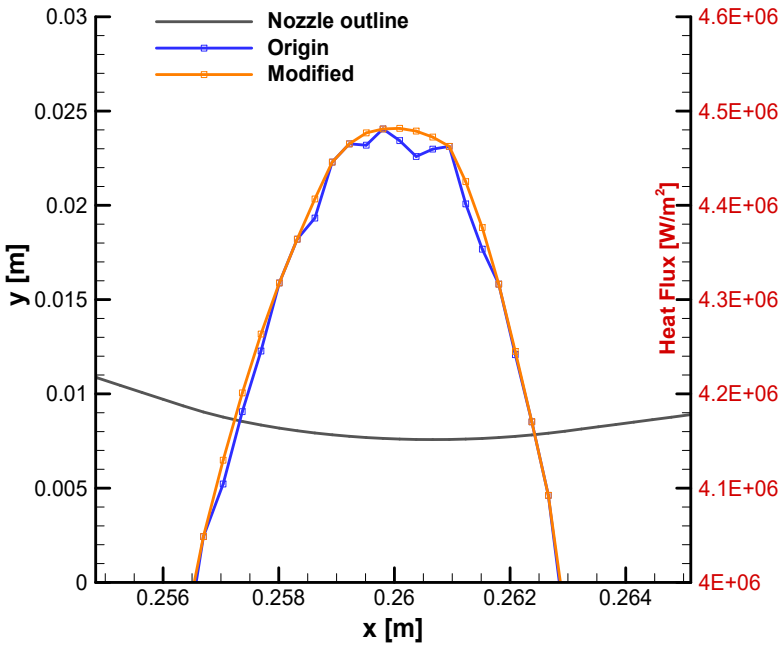

Figure 7.12 Corrected heat flux example

The calculation results using the method of correcting the heat flux amount of the nozzle wall surface are compared with those before the correction. Figure 7.13 is a graph before and after correction of the wall surface temperature rise near the nozzle throat over time. The wall temperature oscillation is greatly improved because the heat flux amount correction was performed before the temperature oscillated. In addition, the data analyzed in Figure 7.11 was corrected by smoothing the heat flux amount from iptime 151, and the result is shown in Figure 7.14. Wall heat flux and wall temperature oscillation is improved.

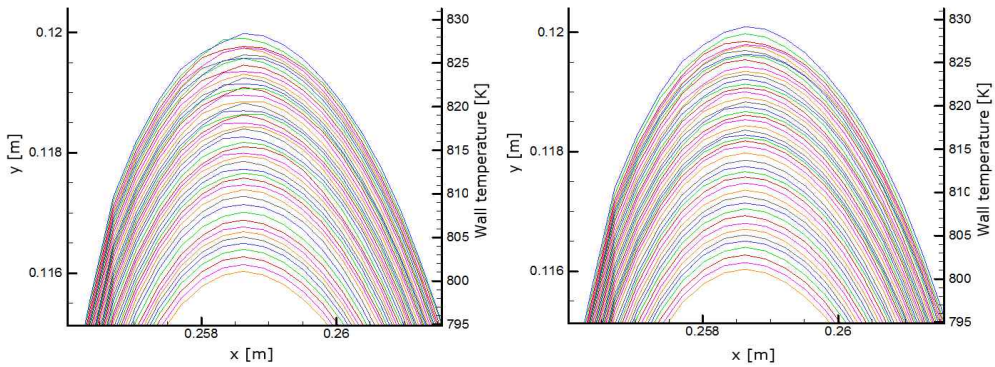

Figure 7.13 Wall temperature over time with correction, before(left) and after(right)

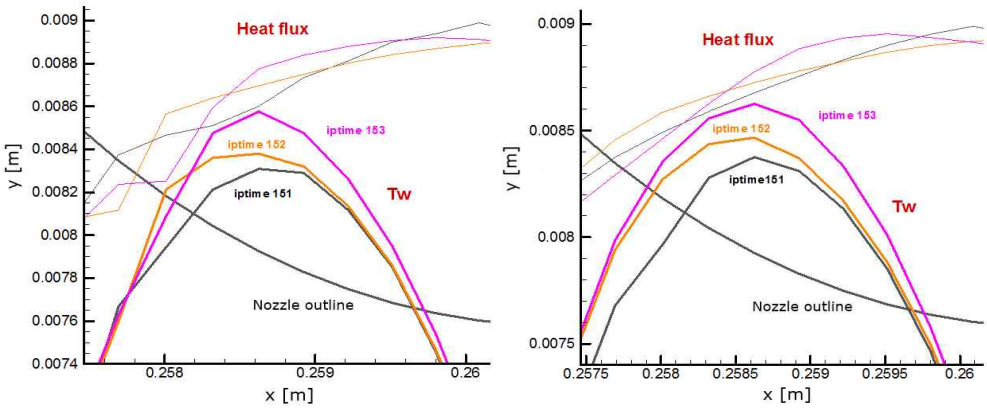

Figure 7.14 Wall temperature and heat flux of verification case with correction, before(left) and after(right)

Flow/structure analysis is performed again using nozzle wall heat flux correction method. The results are shown in Figures 7.15 and 7.16. Although the oscillation remains, the heat flux is corrected to suppress divergence. In addition, both the heat flux and wall temperature graph follow the trend during the oscillation, and the trend change that is thought to be error does not occur as compared with the calorically perfect gas graph. Therefore, it was confirmed that there might be no big difference in predicting the amount of the ablation using the wall heat flux and the wall temperature from the integrated code analysis result.

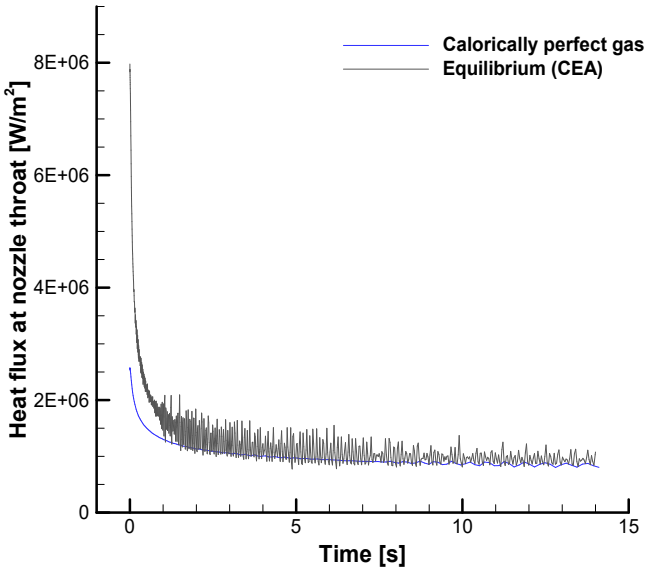

Figure 7.15 Wall heat flux at nozzle throat over time, comparison by flow type, 3rd test

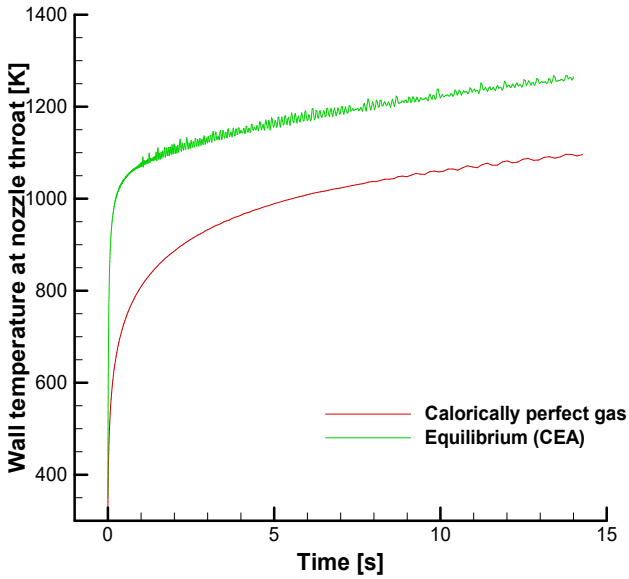

Figure 7.16 Wall temperature at nozzle throat over time, 3rd test

7.4. Physical time step setup

In order to perform calculations using a computer, the time of continuous nature must be expressed in a discrete form. In order to perform the time advance calculation, time is divided into discrete time and a variable called physical time is set. Increasing the number of physical time intervals by setting the physical time interval to a smaller value reduces the numerical error, making the calculation result more accurate, but it increases the amount of iterations and increases the total calculation time. Therefore, in order to reduce the calculation time, the number of physical time intervals is reduced as much as possible, and the physical time interval is set to a maximum value within a range in which the numerical error does not affect the analysis re-

sult severely. Table 7.2 summarizes the physical times set in this study.

Table 7.2 Number of physical time step, target time and time step summary

Number of step	Target time [s]	Time step [s]	
209	20	0.05 ~ 0.182	
915	20	0.004 ~ 0.044	
768	14	0.004 ~ 0.037	3rd test
892	19	0.004 ~ 0.043	4th, 5th test

The calorically perfect gas graph of Figure 7.15-16 is the result of calculating 209 physical time intervals, with some oscillation remaining. In order to check how much the numerical error is reduced and how much the oscillation is mitigated by arranging the 915 physical time intervals and the calculation result is compared with 209 physical time intervals results. The result is shown in Figure 7.17-18.

The smaller the physical time interval and the longer the calculation is done, the smaller the numerical error and the oscillation is alleviated.

However, in the case of calorically perfect gas flow calculated with 915 physical time intervals, calculation takes 8 days. If the equilibrium flow is analyzed, the total computation time is about twice as long. If the equilibrium flow is analyzed at 915 physical time intervals, the total computation time is 14 to 15 days. If the physical time intervals are further narrowed to reduce the numerical errors and oscillations, the computation time becomes very long, so there is a great deal of difficulty in setting a small physical time interval. Therefore, 768 and 892 physical time step intervals are used.

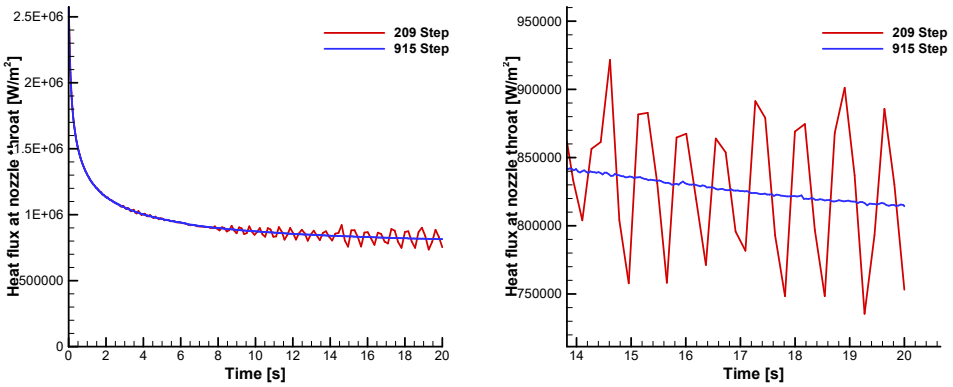

Figure 7.17 Wall heat flux at nozzle throat over time (Calorically perfect gas), comparison by physical time step variation. right graph is zoomed in

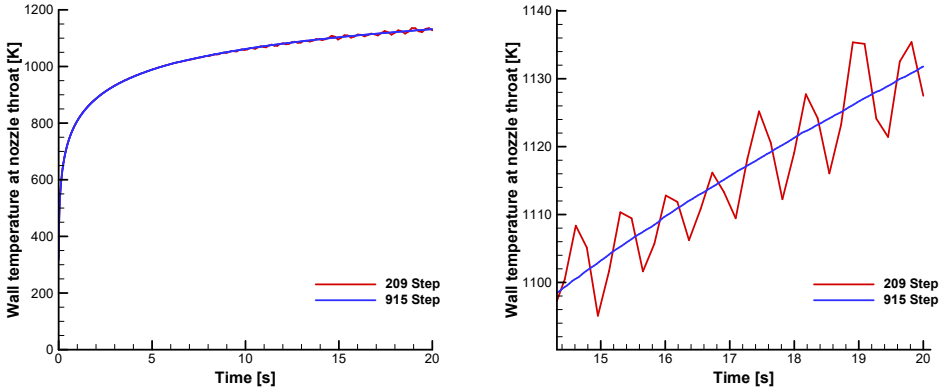

Figure 7.18 Wall temperature at nozzle throat over time (Calorically perfect gas), comparison by physical time step variation. right graph is zoomed in

7.5. Results of flow/structure integrated analysis code and discussion

The results of the calculation of the amount of ablation from the flow/structure integrated code developed in this study are summarized in this section. The results of the calculations are summarized in the vicinity of the nozzle throat as shown below.

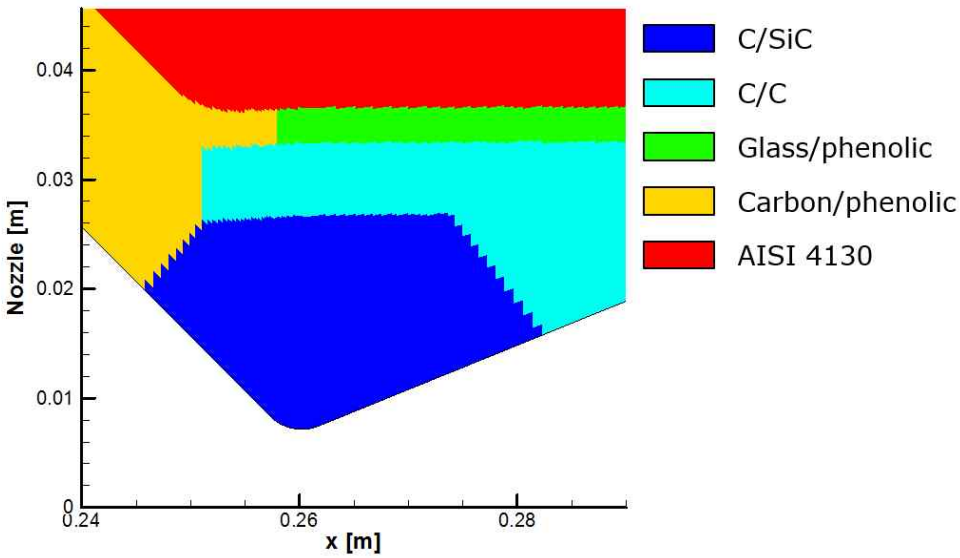

Figure 7.19 Material distribution of nozzle structure around nozzle throat (zoomed in)

7.5.1. Results of equilibrium flow field analysis

The results of equilibrium flow analysis of nozzle combustion gas using CEA database are shown in Figure 7.20-23. Figure 7.20-22 shows the flow analysis results of the first iptime under 3rd test conditions, and is the Mach number, temperature, and pressure distribution contour, respectively. Starting from the combustion chamber, the Mach number, temperature, and pressure

do not show any change until reaching near the nozzle throat, and it can be seen that the value changes rapidly through the vicinity of the nozzle throat.

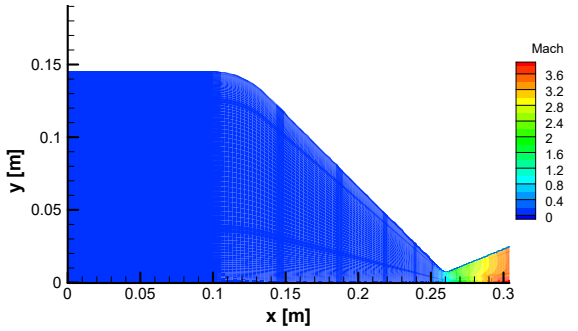

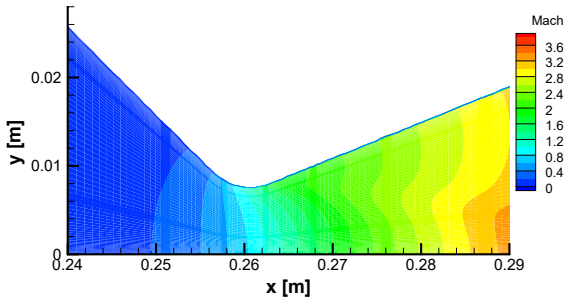

Figure 7.20 Mach number contour, t=0.000 s, 3rd test (bottom contour is zoomed in around nozzle throat)

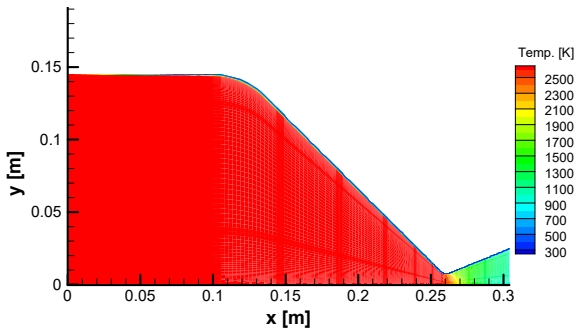

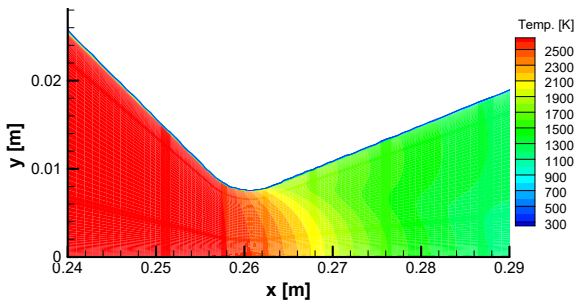

Figure 7.21 Temperature contour, t=0.000 s, 3rd test (bottom contour is zoomed in around nozzle throat)

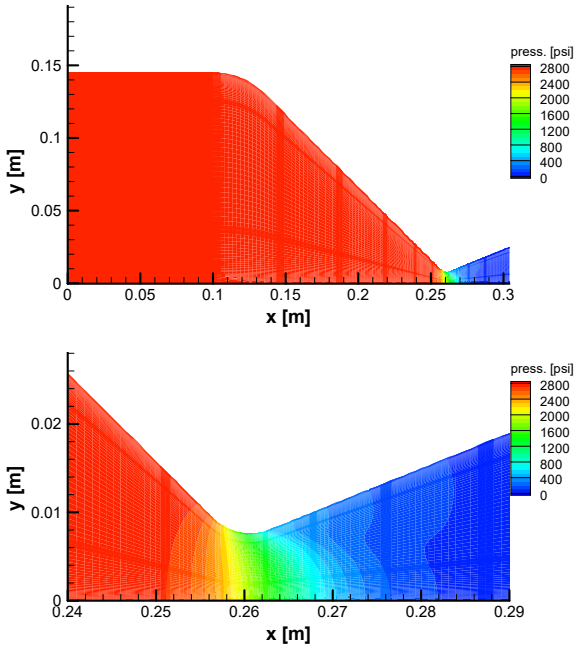

Figure 7.22 Pressure contour, t=0.000 s, 3rd test (bottom is zoomed in around nozzle throat)

Figure 7.23 shows the pressure distribution on the nozzle wall. The graph of the nozzle pressure distribution is kept constant from 0 seconds until the target time of the test without any significant difference. A sudden pressure drop due to supersonic expansion occurs in the nozzle throat, and the pressure near the nozzle outlet decreases near atmospheric pressure.

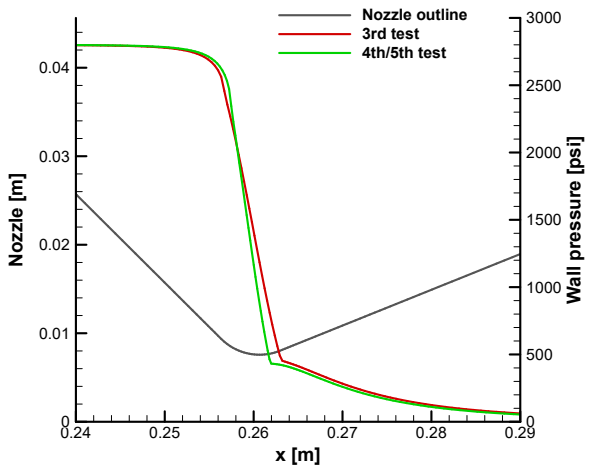

Figure 7.23 Nozzle wall pressure distribution

7.5.2. Results of structure temperature distribution analysis

The temperature distribution of the structure is analyzed over time. Due to the heat flux to the nozzle wall from the flow, the wall temperature rises over time. Figure 7.24-25 below show the temperature distribution at the target time of the 3rd and 4th/5th tests, respectively. The temperature is the highest near the nozzle throat, and the temperature rise near the outer boundary of the nozzle, which was in contact with the outside air, hardly occurred.

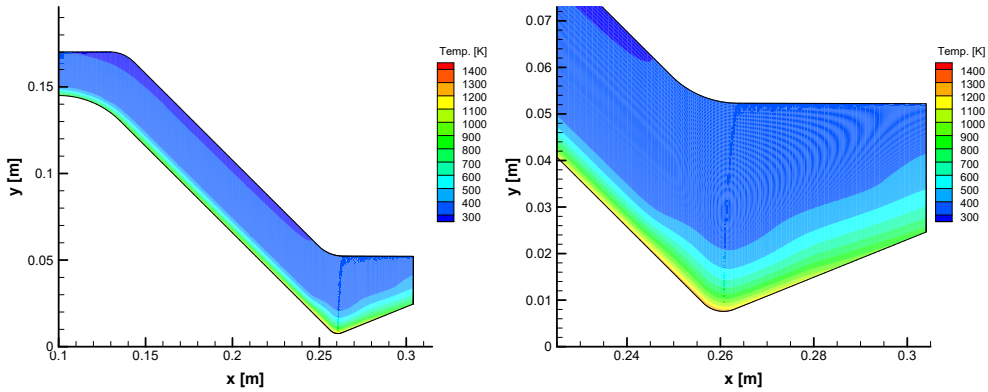

Figure 7.24 Temperature distribution of nozzle structure, t=14.000 s, 3rd test, right contour is zoomed in

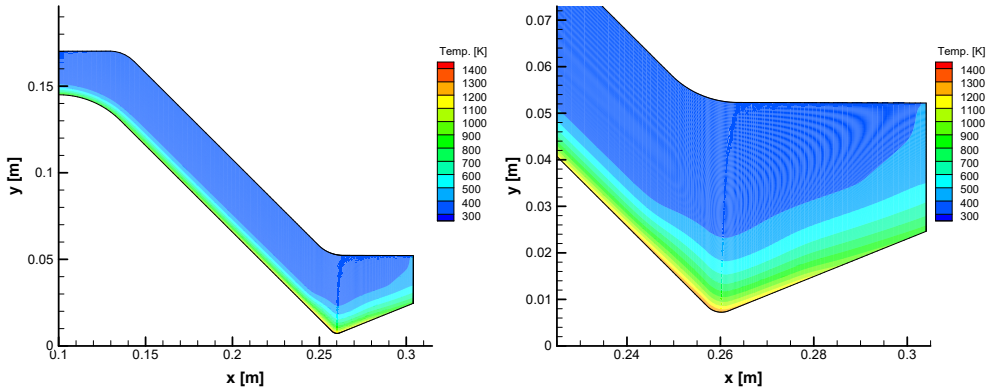

Figure 7.25 Temperature distribution of nozzle structure, t=19.000 s, 4th/5th test, right contour is zoomed in

7.5.3. Wall heat flux, shear stress, and wall temperature distribution near the nozzle throat

In Figure 7.26, the heat flux is relatively large near the nozzle throat at the beginning of the test, but decreases rapidly after a few seconds. This characteristic can also be confirmed by looking at Figure 7.15. After a certain period of time, in the C_f/SiC material region (about x=0.246-0.282 mm), the heat flux peak position is still near the nozzle throat, but the peak value is not markedly larger than the surrounding values. After passing through x = 0.282 mm, the material of the nozzle which is in contact with the flow changes to C/C, which has a relatively large heat transfer coefficient α. The larger the heat transfer coefficient, the faster the temperature propagation and the slower the wall temperature rise, so the C/C material region has much lower wall temperature than C_f/SiC. Therefore, since the temperature gradient from the flow to the wall becomes large due to the low wall temperature, the graph shows the suddenly rising heat flux when the material is changed to the C/C material.

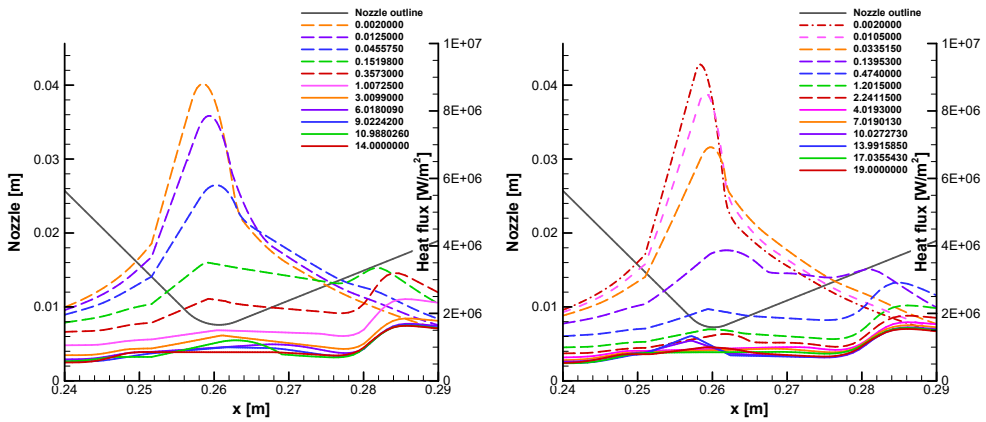

Figure 7.26 Wall heat flux distribution around nozzle throat over time, 3rd test(left) and 4th/5th test(right)

Figure 7.27 shows the change of wall shear stress over time. From the beginning of the test, it shows a rapid rise until 1 second, but after that it shows that the shear stress slowly rises untill the target time. Both the 3rd test and the 4th and 5th test show a peak near the nozzle throat, then decrease rapidly, and gradually decrease after passing the nozzle throat.

The peak is larger and narrower at the 4th/5th test conditions because the nozzle throat diameter of the 4th/5th test is smaller than that of the 3rd test.

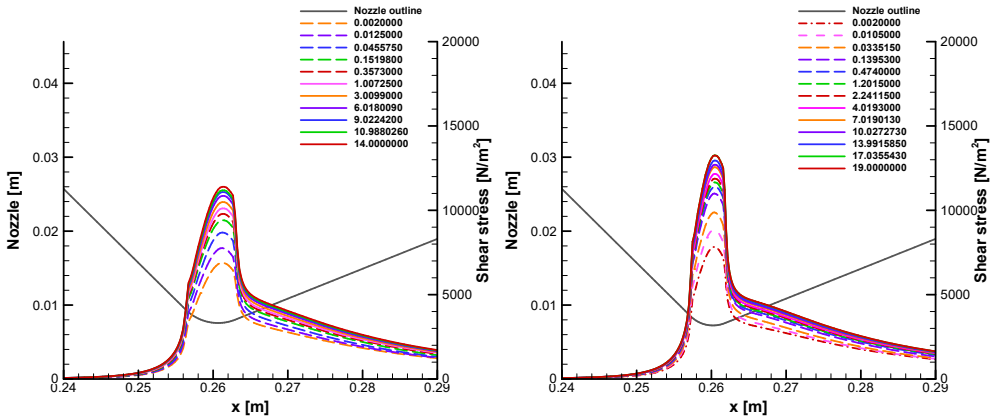

Figure 7.27 Wall shear stress distribution around nozzle throat over time, 3rd test(left) and 4th/5th test(right)

Figure 7.28 shows the time-dependent increase of the nozzle wall temperature distribution. Since the heat flux is initially high but rapidly decreases to 1 second for both the 3rd and 4th/5th test, the rise in wall temperature also takes a similar pattern. The initial rise of 1 second shows a steep increase over time, but thereafter the temperature rise is slow because the wall heat transfer remains about 1 $\mathrm{MW/m^2}$. Both tests show the maximum wall temperature near the nozzle throat.

As shown in the graph of the heat transfer rate, it can be seen from the temperature distribution graph that the wall temperature rises slowly after the

point of x = 0.282 mm because the nozzle material that meets the nozzle flow changes to C/C and the heat transfer coefficient increases

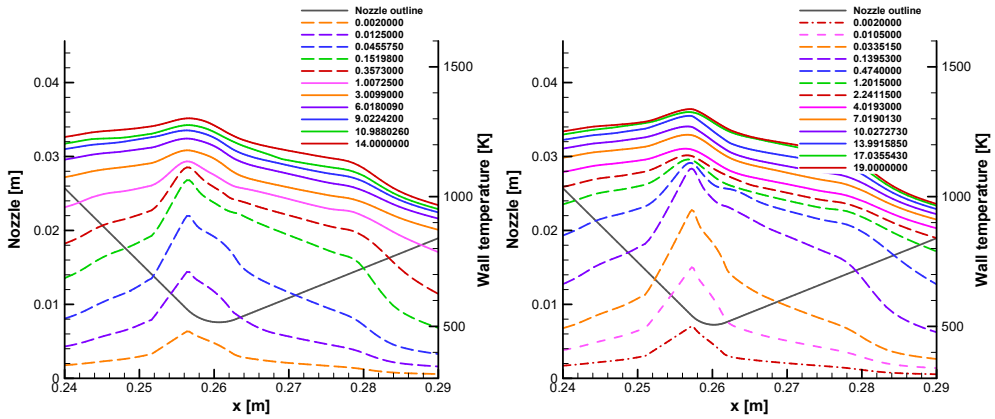

Figure 7.28 Wall temperature distribution around nozzle throat over time, 3rd test(left) and 4th/5th test(right)

7.5.4. Prediction of the amount of SiC coating ablation

7.5.4.1. Shear erosion prediction

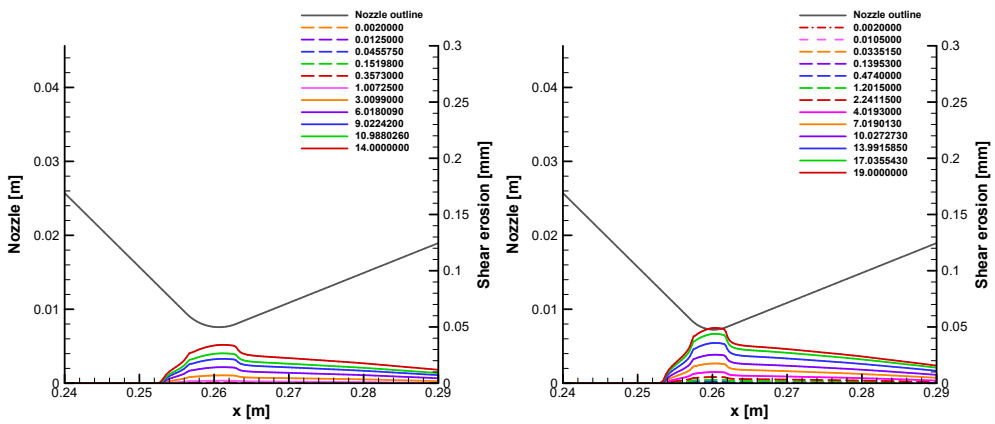

Figure 7.29 Shear erosion distribution around nozzle throat over time, 3rd test(left) and 4th/5th test(right)

Figure 7.29 is a graph showing the amount of mechanical ablation using the shear erosion model over time. The ablation does not occur at the initial stage of the test, and it can be confirmed that the ablation proceeds after a certain period of time. Since the shear force is largest at the nozzle throat, the shear erosion maximum also occurs at the nozzle throat.

7.5.4.2. Melting erosion prediction

A melting model was applied to simulate the removal of the SiO_2 layer which is formed by the oxidation reaction with the combustion gas on the SiC coated surface. As a result of the integrated code calculation, it was found that the wall temperature remained near 1,400 K below the melting point of SiO_2 even when the wall temperature reached the target time, and thus the temperature was too low to immediately apply the melting model.

The removal phenomenon of SiO_2 layer might be considered to be a process of melting and being washed away into a liquid state. Therefor, additional wall surface temperature rises, where the temperature rises to the melting point, are considered to apply the melting model. However, since the additional wall surface temperature rise of the SiO_2 layer calculated using pure SiO_2 thermal conductivity is only about 50 K, other effects must be considered.

▶Calculation of additional wall surface temperature rise using DEM (Differential effective medium) theory

The DEM theory is theoretically developed to calculate the effective properties of composite materials. Norris[32] proposed a method to theoretically calculate the effective properties of a composite material when a material made of one material is replaced by another material as much as the volume fraction. Norris generalized several problems, and solved the problem of con-

ductor-insulator composites by DEM theory to obtain effective conductivity when some of the conductors were replaced by insulators with zero conductivity. Hopkins[33] applied this DEM theory to the thermal conductivity of SiO_2 and compared the theoretical thermal conductivity of SiO_2 to the porosity with the experimental data as shown in Figure 7.30.

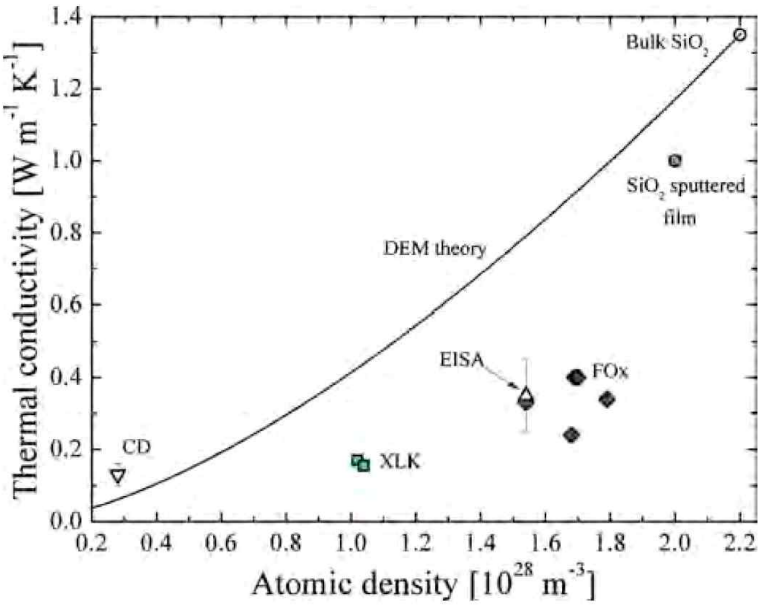

Figure 7.30 Thermal conductivity of various SiO_2 samples with porosity property[32]

The solid line in Figure 7.30 is a graph showing the thermal conductivity of bulk amorphous SiO_2 by applying the DEM theory. The porosity is expressed as atomic density by simple calculation using molecular weight, and Hopkins shows the decrease in thermal conductivity as a function of atomic density as in Eq. (7.1). As the porosity of SiO_2 increases, the atomic density of SiO_2 decreases and the thermal conductivity decreases. The CD, EISA, XLK, and FOx in Figure 7.30 are the films made of SiO_2 material and thermal conductivity measurements show lower thermal conductivity than that of

DEM theory.

$$\text{DEM theory} : k = k_{solid}\left(\frac{n}{n_{solid}}\right)^{3/2} \tag{7.1}$$

k: conductivity, n : atomic density

The density of SiO_2 amorphous is ρ_{SiO_2}=2.196 g/cm^3=2,196 kg/m^3, molecualr weight is MW_{SiO_2}=60.08 $kg/(kg-mole)$, Avogadro constant is N_{av}= 6.022×10^{26} $particle/(kg-mole)$. Thus, the atomic density of SiO_2 is $n_{SiO_2} = \frac{\rho_{SiO_2}}{MW_{SiO_2}} N_{av} = \frac{2196}{60.08} 6.022\times10^{26} = 2.20112\times10^{28}$ $particle/m^3$. Using k_{SiO_2}=1.35 $[W/m\,K]$, the thermal conductivity of SiO_2 to porosity is theoretically summarized as shown in the Table 7.3. When the porosity is 50%, the thermal conductivity is 0.47730 $[W/m\,K]$, which is about 1/2.8 times that of pure SiO_2. When the porosity is 75%, the thermal conductivity is 0.16875 $[W/m\,K]$, which is about 1/8 times.

Table 7.3 Thermal conductivity of SiO_2 with porosity by DEM theory

Porosity [%]	Atomic Density, n [particle/m^3]	Thermal Conductivity, k [W/m K]
95	0.1101	0.01509
90	0.2201	0.04269
85	0.3302	0.07843
80	0.4402	0.12075
75	0.5503	0.16875
50	1.1006	0.47730
25	1.6508	0.87685
10	1.9810	1.15265
0	2.2011	1.35000

In order to calculate the additional wall surface temperature rise by applying the DEM theory in this study, I first examined the cross section of nozzle throat after the nozzle combustion test as shown in Figure 7.31. The SiO_2 layer was formed on the SiC coating layer. And as shown in the right side which is the enlarged view of the orange circle region, the thickness of the SiO_2 layer is about 70 μm and the porosity is high because the pore is very large.

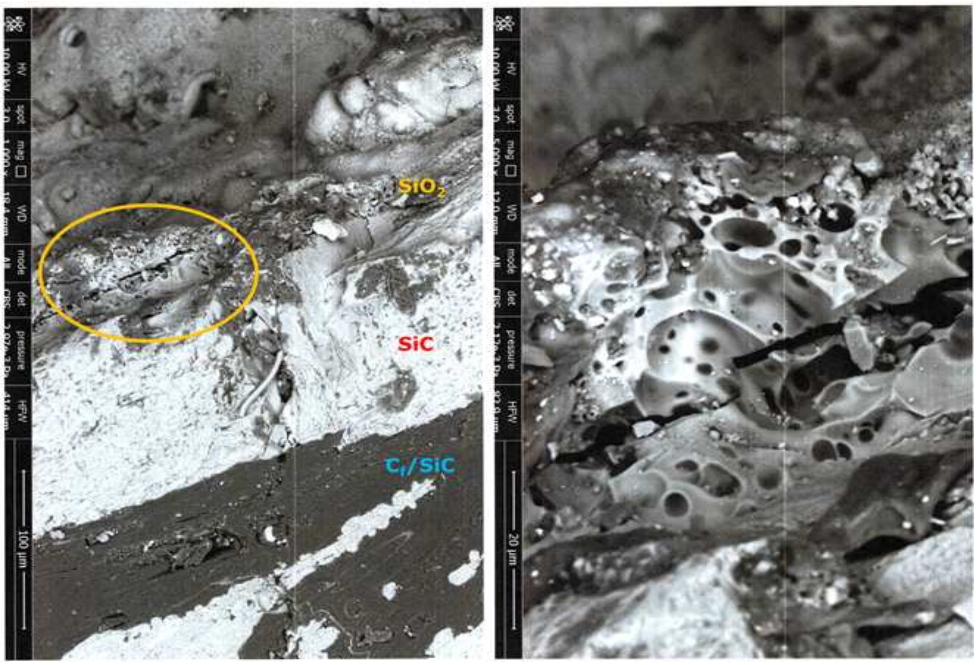

Figure 7.31 Tested nozzle surface. Porous SiO_2 layer is zoomed in (right)

In Figure 7.26, the wall heat flux of the 3rd and 4th/5th tests remains at 1 MW/m^2 after the 3 seconds from the start of the test. Therefore, this value and Fourier's law are used to calculate the additional wall surface temperature rise.

$$\text{Fourier's law} : q = k\frac{\partial T}{\partial x} \rightarrow q = k\frac{\triangle T}{\triangle x} \tag{7.2}$$

$$\triangle T = \frac{\triangle x}{k} q \tag{7.3}$$

$\triangle x$ is the thickness of SiO_2 layer, $70\ [\mu\mathrm{m}] = 70\times10^{-6}\ [\mathrm{m}]$, q is the wall heat flux, and the average value is $1\ [\mathrm{MW/m^2}] = 10^6\ [\mathrm{W/m^2}]$. Examples of the additional wall surface temperature rise($\triangle T$) calculated using these values and the thermal conductivity calculated by the DEM theory equation is as follows.

Porosity 75% : $k = 0.16875\ [\mathrm{W/m \cdot K}] \rightarrow \triangle T = \frac{\triangle x}{k} q = \frac{70\times10^{-6}}{0.16875} 10^6 = 414.8\ [\mathrm{K}]$

Porosity 80% : $k = 0.12075\ [\mathrm{W/m \cdot K}] \rightarrow \triangle T = \frac{\triangle x}{k} q = \frac{70\times10^{-6}}{0.12075} 10^6 = 579.7\ [\mathrm{K}]$

Porosity 85% : $k = 0.07843\ [\mathrm{W/m \cdot K}] \rightarrow \triangle T = \frac{\triangle x}{k} q = \frac{70\times10^{-6}}{0.07843} 10^6 = 892.5\ [\mathrm{K}]$

As shown in Figure 7.31, SiO_2 layer has a very high porosity due to space created by the escape of gas such as CO generated during the oxidation process of SiC. In addition, since the actual measured value in Figure 7.30 is smaller than the DEM theory, the additional wall temperature rise $\triangle T$ might be predicted to be 500 to 900 K or more. The surface temperature of the porous SiO_2 layer rises from 1,800 to 2,200 K or more when the additional wall temperature rise is added to the surface temperature of the SiC calculated by the integrated code(Figure 7.28), thus, the surface temperature could reach the melting point of SiO_2 from 1636 K(high quartz) to 1,996 K(high cristobalite)[34]. Therefore, Figure 7.28 shows the temperature distribution at the interface between the porous SiO_2 layer and the SiC coating, and when the melting erosion calculation is performed, the additional

wall temperature rise due to the porous SiO_2 layer is considered as well as the surface temperature of the SiC.

The additional wall temperature rise is set at 500 K and the melting point of the porous SiO_2 layer was set at 1,650 K to take into account for the additional wall temperature rise exceeding 500 K and the melting point lowering due to impurities such as soot.

The predicted values of melting erosion according to the time considering the additional wall temperature rise are shown in the following figure.

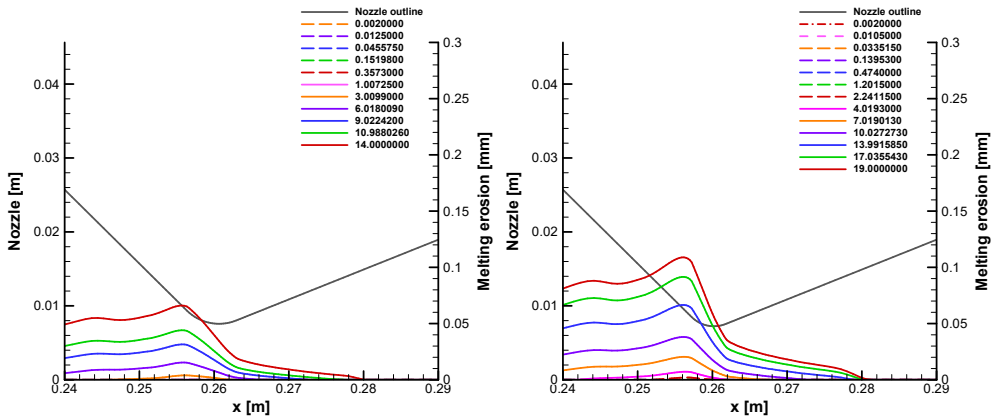

Figure 7.32 Melting erosion distribution around nozzle throat over time, 3rd test(left) and 4th/5th test(right)

7.5.4.3. Total erosion and comparison with measured values

Total erosion, which is the total amount of ablation, is expressed as the sum of shear erosion and melting erosion. Figure 7.33 is a graph showing the total erosion calculated with the integrated analysis code over time. At the beginning of the test, the surface temperature of the nozzle is low and no ablation occurs. After a while, the surface temperature rises to some extent and ablation progresses.

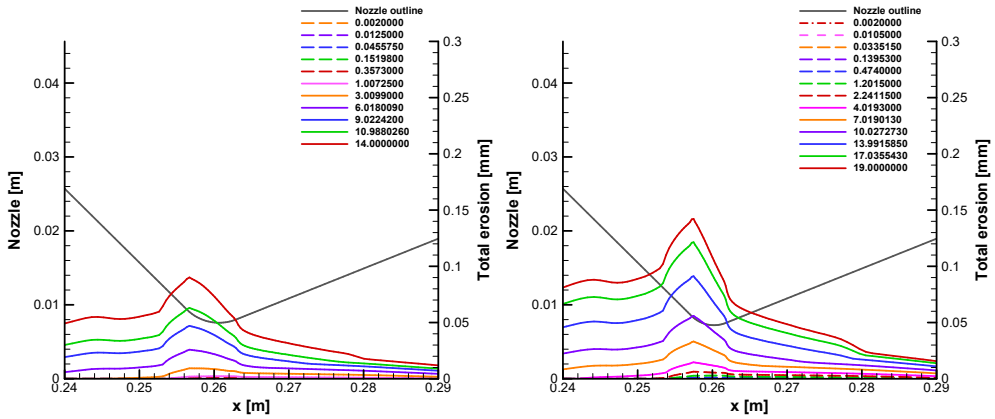

Figure 7.33 Total erosion distribution around nozzle throat over time, 3rd test(left) and 4th/5th test(right)

If it can be measured the nozzle surface heat flux and nozzle-surface/ structure-internal temperature distribution during the test, it is very helpful to make the ablation model, but it is impossible to measure these values because it is the internal flow of tiny nozzle. Therefore, only the measured amount of ablation after the nozzle test is used in the development of the ablation model. In order to compare the amount of ablation calculated by the integrated analysis code with the measured value, the calculated values of the integrated code for the target time of each test are shown along with the test measurement graphs in Figure 6.1 as Figures 7.34-35.

In order to compare and analyze the predicted values through the integrated code and the measured values, the test measured value is needed to be reviewed once more. The measured ablation amount of 3rd test for 14 seconds is larger than that of 5th test for 19 seconds, and the 4th and 5th tests were conducted under the same conditions but the difference in the amount of ablation is considerable. Reproducibility of the test may arise. Therefore, after choosing the 5th test measurement value, which is considered to have accumulated the most experience of the nozzle combustion test team, the ablation

model was developed and focused on matching the integrated code predicted value with the 5th test measurement value (see the pink solid line and the light blue dotted line in Figure 7.35). The predicted value is in good agreement with the measured value of the 5th test.

In the 4th test, the amount of the ablation is relatively large, although it is under the same condition of the 5th test. To match the predicted value to measured value of the 4th test, the melting erosion and shear erosion model was calibrated. Especially, the effect of shear erosion on nozzle throat is increased to compensate the amount of the concentrated ablation. Figure 7.36 shows the calculated result after calibration.

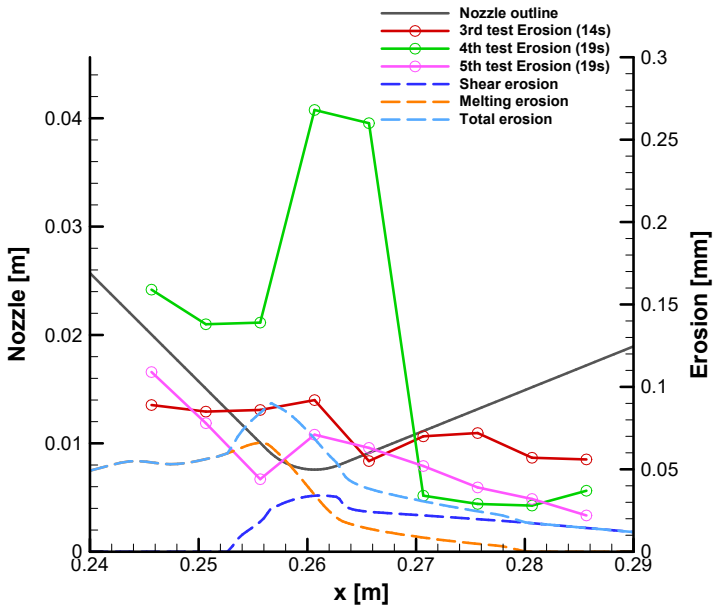

Figure 7.34 Erosion depth comparison of 3rd test

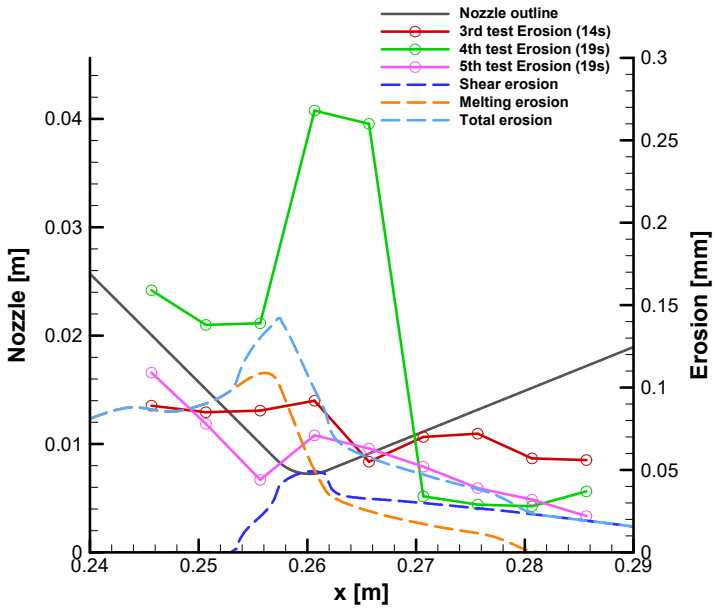

Figure 7.35 Erosion depth comparison of 4th and 5th test

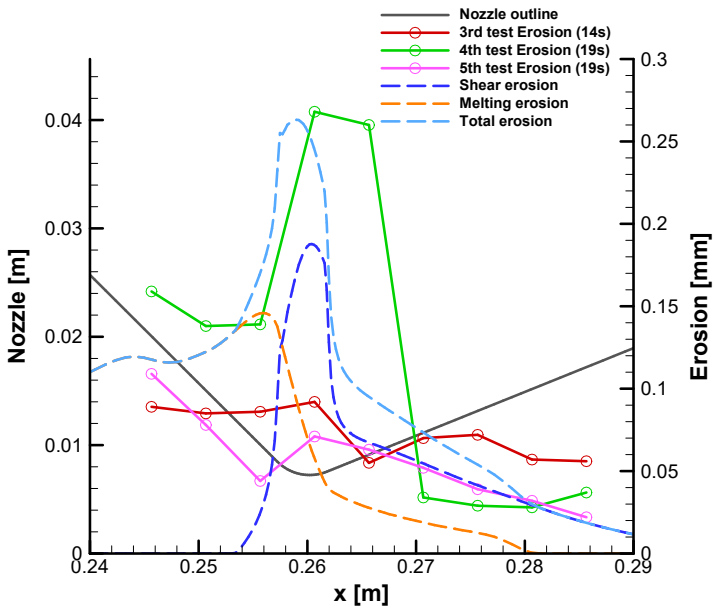

Figure 7.36 Erosion depth comparison of 4th and 5th test, modified shear/melting erosion model

8

CONCLUSION

◇ Development of equilibrium flow CFD code using CEA database

The equilibrium flow analysis code using the CEA database was developed for the analysis of the nozzle combustion gas. (ρ,e) and (T,p) table are made and a function was developed to calculate the equilibrium properties and mole fraction using bilinear interpolation method. Since the CEA GUI program can only display 5 significant digits and it takes a long time to create a table, I modified the CEA source code provided by NASA and included it in the integrated analysis code. It was developed to make tables of 14 significant digits at the beginning of the code operation and finish within about 15 minutes. More than 2000 kinds of chemical species can be used, and the desired equilibrium flow calculation can be done simply by changing the input file.

◇ Analysis of ablation measurements of nozzle test and development of SiC ablation model

If it can be measured the nozzle surface heat flux and nozzle-surface/ structure-internal temperature distribution during the test, it is very helpful to make the ablation model, but it is impossible to measure these values because it is the internal flow of tiny nozzle. Therefore, only the measured amount of ablation after the nozzle test is used in the development of the

ablation model. Looking at the measured amount of ablation, the problem of reproducibility of the test may arise. Therefore, after choosing the 5^{th} test measurement value, which is considered to have accumulated the most experience of the nozzle combustion test team, the ablation model was developed and focused on matching the integrated code predicted value with the 5^{th} test measurement value. I have developed a methodology for the development of the ablative model using a limited set of test measurements. The ablation model can be improved by the correction using later test results.

◇ Limitations and future works

In this study, oscillation and divergence of nozzle wall heat flux occurred. Though it is possible to suppress the numerical oscillation by setting a narrow physical time interval, this method is not adopted because the calculation costs much times with current computing power. As a solution to this problem, the structural properties and the heat flux of the nozzle wall were corrected. However, this correction solves the numerical oscillation of only one lattice layer adjacent to the nozzle surface, and the numerical error of the inner lattice of the flow remains intact. Since the heat flux is a value obtained by converging with the internal lattice inside the flow through mutual calculation, the numerical error of the inner lattice inside the flow field as well as the lattice in contact with the nozzle surface should be solved by a method of correcting the source term of the dual time stepping.

9

REFERENCES

[1] Anderson, John David. *Hypersonic and high temperature gas dynamics*. AIAA, 2000.

[2] Kim, K. H., Kim, C., Rho, O. H., “Methods for the Accurate Computations of Hypersonic Flows - Part I : AUSMPW+ Scheme.“ *Journal of Computational Physics*, Vol.174, 2001, pp.38-80

[3] S. Yoon, A. Jameson, An LU-SSOR Scheme for the Euler and Navier-Stokes Equations, NASA Contractor Report 179556.

[4] Gordon, Sanford, and Bonnie J. McBride. "Computer Program for Calculation of Complex Chemical Equilibrium Compositions and Applications. Part 1: Analysis." (1994).

[5] McBride, Bonnie J., and Sanford Gordon. "Computer Program for Calculation of Complex Chemical Equilibrium Compositions and Applications II. Users Manual and Program Description. 2; Users Manual and Program Description." (1996).

[6] Shuen, Jian-Shun, Meng-Sing Liou, and Bram Van Leer. "Inviscid flux-splitting algorithms for real gases with non-equilibrium chemistry." *Journal of Computational Physics* 90.2 (1990): 371-395.

[7] Shuen and Yoon. "Numerical study of chemically reacting flows using a lower-upper symmetric successive overrelaxation scheme." *AIAA journal* 27.12 (1989): 1752-1760.

[8] Moin, Parviz. Fundamentals of engineering numerical analysis. Cambridge University Press, 2010.

[9] Van Driest, E. R., “Investigation of Laminar Boundary Layer in Compressible Fluids Using the Crocco Method,” NASA TN-2597, 1952

[10] Van Driest, E. R., “Problem of Aerodynamic Heating,” *Aeronautical Engineering Review*, Vol15, No.10, 1956

[11] Hoffman, Klaus A., and Steve T. Chiang. "Computational Fluid Dynamics Volume I." Engineering Education System (2000).

[12] Chen, Bo, et al. "Viscous Flow of Silica and its Effects on Ablation of Carbon/Silicon Carbide Composites as a Liquid-Fueled Rocket Engine Nozzle." *International Journal of Applied Ceramic Technology* 8.6 (2011): 1468-1474.

[13] Fertig, Markus, Hans Frühauf, and Monika Auweter-Kurtz. "Modelling of Reactive Processes at SiC Surfaces in Rarefied Nonequilibrium Airflows." *8th AIAA/ASME Joint Thermophysics and Heat Transfer Conference*. 2002.

[14] Narushima, T., et al. "High-temperature oxidation of silicon carbide and silicon nitride." *Materials transactions, JIM* 38.10 (1997): 821-835.

[15] Opila, E. J., and N. S. Jacobson. "SiO(g) formation from SiC in mixed oxidizing-reducing gases." *Oxidation of metals* 44.5-6 (1995): 527-544.

[16] Munro, R. G., and S. J. Dapkunas. "Corrosion characteristics of silicon carbide and silicon nitride." *Journal of research of the National Institute of Standards and Technology* 98.5 (1993): 607-631.

[17] Kumar, Suresh, et al. "Fabrication and Ablation Studies of 4D C/SiC Composite Nozzle Under Liquid Propulsion." *International Journal of Applied Ceramic Technology* (2015).

[18] Chen, Bo, et al. "Ablation Behavior of a Three-Dimensional Carbon/Silicon Carbide Composite Nozzle in an Ethanol/Oxygen

Combustion Gas Generator." *International Journal of Applied Ceramic Technology* 6.2 (2009): 182-189.

[19] Lou, V. L. K., T. E. Mitchell, and Arthur H. Heuer. "REVIEW—Graphical Displays of the Thermodynamics of High-Temperature Gas-Solid Reactions and Their Application to Oxidation of Metals and Evaporation of Oxides." *Journal of the American Ceramic Society* 68.2 (1985): 49-58.

[20] Hinze, J. W., and H. C. Graham. "The Active Oxidation of Si and SiC in the Viscous Gas-Flow Regime." *Journal of the Electrochemical Society* 123.7 (1976): 1066-1073.

[21] Wagner, Carl. "Passivity during the oxidation of silicon at elevated temperatures." *Journal of Applied Physics* 29.9 (1958): 1295-1297.

[22] Heuer, Arthur H., and Victor LK Lou. "Volatility Diagrams for Silica, Silicon Nitride, and Silicon Carbide and Their Application to High-Temperature Decomposition and Oxidation." *Journal of the American Ceramic Society* 73.10 (1990): 2789-2803.

[23] Deng, DaiYing, et al. "The active-to-passive oxidation transition mechanism and engineering prediction method of C/SiC composites." *Science China Technological Sciences* 56.6 (2013): 1403-1408.

[24] Luo, Changsong, and Paul E. DesJardin. "Thermo-mechanical damage modeling of a glass–phenolic composite material." *Composites Science and Technology* 67.7 (2007): 1475-1488.

[25] ASM Specialty Handbook - Carbon and Alloy Steels, edited by J.R. Davis, Davis & Associates, ASM International, Metals Park, OH, (1996).

[26] Engineering Properties of Steels, Philip D. Harvey, editor, American Society for Metals, Metals Park, OH, (1982).

[27] Metals Handbook, Vol.1 - Properties and Selection: Irons, Steels, and High-Performance Alloys, ASM International 10th Ed. 1990.

[28] Metals Handbook, Howard E. Boyer and Timothy L. Gall, Eds., American Society for Metals, Materials Park, OH, 1985.

[29] Physics for Scientists and Engineers with Modern Physics, 2nd ed., Douglas C. Giancoli, Prentice Hall Publishers, Englewood Cliffs, NJ (1989)

[30] SAE Ferrous Materials Standards Manual, 1999 ed., HS-30, Society of Automotive Engineers, Inc., Warrendale, PA, (1999).

[31] ASTM Standards in ACI 301, 318, and 349, Publication SP-71, American Society for Testing and Materials, Philadelphia, PA, (1980)

[32] Norris, Andrew N., Andrew J. Callegari, and Ping Sheng. "A generalized differential effective medium theory." Journal of the Mechanics and Physics of Solids 33.6 (1985): 525-543.

[33] Hopkins, Patrick E., et al. "Measuring the thermal conductivity of porous, transparent SiO2 films with time domain thermoreflectance." Journal of Heat Transfer 133.6 (2011): 061601.

[34] Chase, M. W. "NIST—JANAF Thermochemical Tables (Journal of Physical and Chemical Reference Data Monograph No. 9)." (1998).

국문 초록

CEA 데이터베이스를 활용한 평형 유동 CFD 코드 개발 및 SiC 코팅 노즐의 삭마량 예측

배 지 환

기계항공공학부 우주항공공학과

서울대학교

노즐 내부의 연소가스로 인한 SiC의 삭마 모델 개발 및 SiC 코팅 노즐 삭마현상 예측, 삭마 해석 코드 개발을 목표로 연구를 수행하였다. 이를 위하여 CEA 데이터베이스를 활용한 평형 유동 해석 코드, 구조물 온도 분포 해석 코드를 개발하였으며 이들의 검증 과정을 수행하여 코드의 신뢰성을 확보하였다. 이 코드들을 벽면 열전달량 및 벽면 온도 경계조건을 주고받음으로써 연동하여 유동/구조물 통합 해석 코드를 개발하였다. SiC 재질의 산화반응 특성을 분석하였으며, 특히 SiC 재질의 active 및 passive oxidation에 대한 조사를 주로 수행하여 삭마 모델 개발에 적용하였다. 기계적 삭마로 shear erosion 모델을, 열화학적 삭마로 용융 모델을 개발하였으며 시간에 따른 노즐목 삭마량을 예측하였다. ADD로부터 전달받은 노즐 시험 삭마량 측정치를 분석하여 각 시험에 대한 삭마량을 측정 위치에 따라 제시하였고, 통합 코드 계산 결과로 얻은 삭마량 예측값과 비교하였다.

주요어: 전산유체역학, 평형유동, CEA, 삭마, SiC, SiO_2

학번: 2015-20772